

Charles University in Prague

Faculty of Mathematics and Physics



DOCTORAL THESIS

**Spin-dependent transport in
layered magnetic nanostructures**

Mgr. Karel Carva

Department of Condensed Matter Physics

Supervisor: Doc. RNDr. Ilja Turek, DrSc.

Prague, January 2007

Preface

During my PhD study I have learned a lot about its subject, the condensed matter theory, but also about other things which are no less valuable: I have seen the amenities and difficulties of researcher's work, understood the importance of team cooperation and the importance of knowing where to find things someone else already revealed or developed. I also became familiar with writing scientific programs and utilizing the power of high performance parallelized computers to carry out physical calculations using these programs. I have developed an extension of existing *ab initio* codes, which calculates lots of properties described in this thesis and was therefore crucial for its accomplishment. The research which ended in writing this thesis was done in cooperation with many other people, who all I wish to thank here. I hope that that the results of this research presented here will contribute to the main purpose of physics, the discovery of underlying laws of nature, namely to answering questions of condensed matter physics, and also offer methods that may help someone else to answer these questions too. In the future there is a big chance that more practical applications based on ideas of the branch of physics presented here will be brought to practice, which is something that assures us about the sense of our work.

First of all I would like to thank my supervisor Doc. RNDr. Ilja Turek, DrSc. for guiding me through the vast field of condensed matter theory, his advices were inevitable for the success of my research work. For example he helped me to understand possibilities and limitations of *ab initio* calculations and the fact that despite the enormous extent of problems being within the reach of current computational condensed matter physics running of programs is just a small portion of physicist's work.

I am very grateful to Prof. RNDr. Vladimír Sechovský, DrSc. for the support of all kinds that he provided to my research as well as the research of the whole department. I thank to RNDr. Josef Kudrnovský, CSc. for motivating discussions that provided me with information about current research topics and helped me to find some astonishing things in physics and also in physicist's life.

I would like to express my thanks to my girlfriend Petra Bernatziková for supporting me and withstanding my complete lack of free time during the work on this thesis. I would like to thank to my colleague RNDr. Jan Rusz, Ph.D., with whom I had many inspirative talks and could share experience with many various topics and problems encountered during the time of my studies. I thank to Dr. Olivier Bengone, Ph.D. who showed me many interesting points of view on studied topics and also developed the initial part of transport extension to electronic structure code.

I thank to Doc. RNDr. Radomír Kužel, CSc., who was always very supportive and showed true interest in good operation of the department. I am grateful to Doc. RNDr.

Martin Diviš, CSc. and Prof. RNDr. Bedřich Velický, CSc. for all valuable knowledge they supplied me during my studies. I thank to Doc. RNDr. Pavel Svoboda, CSc. and Doc. RNDr. Ladislav Havela, CSc. for acquainting me with interesting topics in physics different from my subject of study.

I thank to my colleagues RNDr. Jana Poltířová-Vejpravová, RNDr. Standa Daniš, Ph.D., RNDr. Jiří Prchal, Ph.D., Mgr. Jiří Pospíšil, RNDr. Jan Prokleška, Mgr. Klára Uhlířová and Mgr. Zdeněk Matěj, who made the atmosphere on the department very friendly and informal, made me understand many things and were always very helpful when they help was needed. Last but not least I would like to thank to my parents, who were always standing by me.

Contents

1	Introduction	5
1.1	Outline	6
2	Fundamentals	9
2.1	Density functional theory	9
2.2	TB-LMTO method	12
2.2.1	Linearization	13
2.2.2	Tight-binding technique	14
2.2.3	Lattice translational symmetry, principal layers, leads	16
2.3	Spin-dependent transport in layered nanostructures	18
2.4	Conductance from the linear response theory	21
2.4.1	Charge conductance	23
2.5	Substitutional disorder	26
2.5.1	Configurational averages	26
2.5.2	Supercell method	27
2.5.3	Coherent potential approximation	27
3	CPP conductance in disordered multilayers	29
3.1	CPA averages of two-particle observables, vertex corrections	29
3.2	LMTO full CPA solution for conductance	30
3.3	CPP conductance in disordered multilayers	31
3.3.1	Lattice point group symmetry	33
4	Spin torques due to spin accumulation	35
4.1	Spin accumulation and spin torques	36
4.2	Derivation based on NEGF	38
4.3	Derivation based on the Kubo theory	40
4.4	Comparison to scattering theory	42
4.5	TB-LMTO-CPA formulation and implementation	43
4.6	Summary of calculations results	45
4.6.1	Properties of saturated mixing conductance	47
4.6.2	Magnetic tunneling junctions	48

5	Spin torques in non-collinear layered systems	51
5.1	Spin currents and spin-transfer torques	51
5.2	Ab initio formulation	54
5.2.1	Spin currents from linear response theory	54
5.2.2	TB-LMTO expression	55
5.2.3	Ab initio torque in non-collinear spin valves	57
5.3	Comparison to spin-mixing conductance	58
5.4	Summary of calculations results	61
5.4.1	Angular dependence	63
6	Co/Cu multilayers with substitutional disorder	67
6.1	Electronic structure	67
6.2	Co Cu Co multilayers with interface roughness	68
6.2.1	Transport properties	69
6.2.2	Comparison to supercell calculations	70
6.3	Co Cu _{0.84} Ni _{0.16} Co trilayers with randomness in the spacer	71
6.4	CoCr Cu Co trilayers exhibiting negative GMR	72
6.4.1	Transport properties	72
6.4.2	The origin of the negative GMR	73
6.4.3	The influence of interface interdiffusion	75
7	(Ga,Mn)As thin layers	77
7.1	Bulk (Ga,Mn)As	78
7.1.1	Lattice defects	79
7.1.2	Uncompensated DLM state	84
7.2	Ideal (Ga,Mn)As layers coupled to metallic leads	84
7.3	(Ga,Mn)As layers with lattice defects	89
7.3.1	Uncompensated DLM state	91
8	Co₂MnSi thin layers	95
8.1	Bulk properties	95
8.2	Thin layers	98
8.3	Spin valves	101
9	Conclusions	103
A	Kubo formula for generalized CPP transport	105
B	Invariance property of spin-mixing conductance	109
	Bibliography	113

Chapter 1

Introduction

Interaction between magnetic and electric properties is a phenomenon that attracts a lot of attention of physicists and also engineers, spin-dependence of electron transport is an important subject of research. Consider the fact that magnetism allows information to be permanently stored while electron transport allows its distribution. Both of them can cooperate in its analysis. Magnetoresistance is a change of resistance under influence of a magnetic field, hence it allows for a detection of a magnetic state. It was discovered in 1856 by Lord Kelvin and originates from the Lorentz force acting on the itinerant electrons, which causes extra deflection on their trajectories. This kind of magnetoresistance in bulk materials reaches very low values of up to a few percent. It depends on the angle between current direction and the orientation of magnetization, hence it is called anisotropic magnetoresistance (AMR). Bulk magnetoresistance can go up to much higher values for some recently found materials, typically f-electron based, where the jump in resistance can be attributed to a magnetism induced phase transition, but these phenomena happen usually at uselessly low temperatures and require high switching fields.

A completely different source of magnetoresistance arises on microscopic scale, from the spin-dependence of electron scattering at interfaces. The transition probability of spin-polarized electrons is strongly influenced by the spin-polarization of states in the magnetic material it is entering. In order to exploit this effect, the distances between spin-polarized interfaces must be smaller than the spin diffusion length, so that electrons incident on an interface remain polarized from the previous one. With the advent of new fabrication techniques, such as molecular beam epitaxy (MBE) it became possible to manufacture these nanoscale systems. Only one dimension is required to fulfill that size condition, which is the case of thin layers or its many repetitions to amplify the effect: multilayers. Another important point was the observation of the *interlayer exchange coupling* (IEC) in 1986 [1], that may cause antiparallel orientation of the mentioned thin magnetic layers in the ground state and allows lower magnetization switching fields than in setups with negligible IEC. These progresses stimulated the discovery of the *giant magnetoresistance* (GMR) [2] and the *tunneling magnetoresistance* (TMR) [3], which capitalize the idea of multiple spin-dependent electron scattering at interfaces, their principle is explained in chapter 2.3. The corresponding magnetoresistance ratio (according to the definition in Eq. 2.37) reaches values of up to a few hundred percent, note for example the MR ratio of 271% found in a Co | MgO | Fe junction at room temperature [4]. Recently also other

different microscopic processes were found to give rise to high magnetoresistance. Tunneling anisotropic magnetoresistance (TAMR) was shown to reach values of the same order in (Ga,Mn)As based diluted semiconductors [5, 6]. This effect is believed to be caused not by the spin-dependent interface scattering, but by the *spin-orbit coupling*. It is also present only in thin layers, where the necessary additional symmetry breaking can be achieved.

The GMR effect was recognized to be so interesting for the industry that it took only about a decade since its discovery until it was applied in consumer electronic devices [7]. This success has stimulated higher interest in spin-dependent transport and that branch of physics has later shown itself to be extraordinary fruitful. Devices combining intentionally effects of spin and electronics have been proposed and this whole topic has been covered in under the name *spintronics*. Magnetoresistance represents not only reading, but also further operations on signal. This is the case of recently proposed *spintronics* device: a spin valve transistor [8]. It is basically a combination of the GMR effect and semiconductor transistor technology. In addition to traditional metal base transistors it features a base including two FM layers with different coercivities leading to spin-dependent scattering of hot electrons. As for GMR the spin-dependent scattering of electrons depend on the relative orientations of the two layers, which can be controlled due to their different coercivities. The ratio between collector and emitter current is much higher than the CIP-magnetoresistance of this system, which is explained by much higher sensitivity of hot electrons to its mean free path and subsequent exponential dependence of collector current on it. Spin valve transistors are not examined here, but represent an example of the vast opportunities of combining spin and semiconductor technology.

The magnetization influences strongly the electron transport. As was pointed out by Slonczewski [9], an opposite effect is also possible: Spin polarized current incident on a differently polarized FM layer exerts a *spin torque* which rotates the magnetization direction of that FM layer. Spin polarization of the current can be achieved in another FM layer preceding the rotated one. This effect has no relation to *Oersted fields* and can be easily recognized from it by its behavior with respect to current direction reversal. It has also an important advantage over magnetic field induced switching, where the switching field is roughly independent of grain size. The magnetic field due to current decreases with decreasing wire radius at constant current density. The *spin torque* effect allows applications, which avoid direct manipulation with magnetic field and its source and it scales differently: It is independent of wire radius at constant current density, therefore it dominates over *Oersted fields* caused by the same current for low wire radii, typically the threshold radius is about $0.1\mu m$ [10, 11]. One of the applications can be a nonvolatile magnetic computer memory (MRAM) with top parameters comparable to classical computer random access memory (DRAM) and without a need for constant power supply. If the *spin torque* is insufficient to rotate magnetization to another stable position, the magnetization precess, which gives rise to radio frequency oscillations on nanoscale [12, 13]. This is a conveniently measurable effect and another prospect for interesting applications.

1.1 Outline

The main aim of this work is to develop and apply first principles (*ab initio*) methods to deal with the presented phenomena. Chapter 2 describes *ab initio* methods and other

fundamentals necessary to understand the physics employed in subsequent text. Chapters 3-5 present novel methods developed in this work and together with Chapter 2 they constitute the theoretical part of this thesis.

Existing theoretical results for transport in thin layers based on the local spin density approximation (LSDA, Sec. 2.1), linear muffin-tin orbital (LMTO, Sec. 2.2) method and Kubo-Landauer formalism (Sec. 2.4.1) are in many cases in good agreement with experiments. Significant problems arise for systems with substitutional disorder, either at interfaces or spread across thin layers. These problems have been up to now solved by means of the supercell method (Sec. 2.5.2), where the results are quite satisfactory, but its calculations' numerical demands can grow very fast and there are some other drawbacks. An alternative approach is based on the coherent potential approximation (CPA - Sec. 2.5.3), and its first complete application to transport in 2D structures without crude approximations neglecting the effect of two-particle correlated motion is described in Chapter 3 (already published in [14]).

Many works have been published about the dynamics of system under influence of a given *spin torque*, but quantitative understanding of this observable is no less necessary and there are only plenty of publications dealing with *ab initio* evaluation of this phenomena [15]. Chapters 4 and 5 of this work attempt to contribute solving questions related to this topic. More approaches are available: One can see *spin torques* as results of an influence of infinitesimally small spin accumulation (Sec. 4.2) in NM lead adjacent to the FM layer as described in Chapter 4 and soon to be published [16]; or it is possible to describe the whole non-collinear spin valve and evaluate the *spin torque* acting on one of FM layers, which is done in chapter 5. The first approach gives more insight into the mechanism of *current induced magnetization reversal* and the role of material properties, while the second one corresponds better to real experiments and catches properties connected with the non-collinear setup as is the angular dependence of calculated quantities. The correspondence of these two approaches was also studied (Sec. 5.3). Both these chapters contain a section summarizing main results obtained for real materials, more details about these materials can be found in the second part of this thesis.

All transport calculations presented in this work assume linear response regime, which allows to utilize the successful Kubo theory (Sec. 2.4) [17, 18]. Some derivations shown here (Sec. 4.2) are based on non-equilibrium Green's function formalism [19], but they are confined to zero bias. Non-equilibrium situations with finite bias represent a formidable problem beyond the scope of this work. Although there are many successful finite bias calculations [20, 21], some issues connected with lead self-energies [22, 23] or with the use of the DFT (discussed in Sec. 2.1) remain still unresolved. We have also proven that the presented transport calculations are independent of the choice of partitioning of the system into the left and right lead and the intermediate region (provided that the preconditions for this partitioning are satisfied), see Appendix B.

The second part of this thesis demonstrates applications of the derived theories and methods for various particular systems. In Chapter 6 Co|Cu|Co based trilayers are examined with a special attention to the problem of interface interdiffusion. The cases of magnetic impurities in one Cu layer and other metal impurities in Co layers are also mentioned. The latter case may lead to the negative GMR, this rather rare situation is explained in Sec. 6.4.2.

Spintronics applications depend strongly on spin and hence it would be beneficial to have a material which permits electrons with spin in only one direction, an ideal spin-filter. This requirement is satisfied by magnetic materials which behave partially like metals and partially like semiconductors: *half-metals* [24], whose bands are spin-split in such a way, that the band crosses the Fermi energy in one spin direction while in the other one a band gap is located at the Fermi energy (see Fig. 7.2 for an example density of states). Materials presented in Chapters 7, 8 are both *half-metals*. Chapter 7 describes *diluted magnetic semiconductors* (DMS) [25], a novel material combining properties of semiconductors with ferromagnetism. They may also help to resolve the problem of *spin injection* into semiconductors [26]. Their unique features are achieved by substituting some of atoms on its cation sublattice by magnetic impurities, a process which was made possible only recently due to the progress in technology. We examine its transport properties, the role of native structural defects and also the spin-mixing conductance (Chap. 4), for which some unexpected findings are shown. Chapter 8 deals with a *Heusler alloy* Co_2MnSi . Here the halfmetallicity is accompanied by a very high Curie temperature. Its structure is simpler than that of (Ga,Mn)As because in its ideal form it contains no intrinsic disorder, however we find that disorder is probably present anyway in real samples in quite high amount as a defect and that it can explain some of experimental observations.

Chapter 2

Fundamentals

Most of the properties of the solids are closely related to the behavior of electrons, the particles that holds atoms together to form a solid. The determination of electronic structure (ES) is thus a key step in realistic predictions of these properties, including the main subject of this work: transport properties. Traditional ES calculations involving phenomenological parameters were given a more powerful alternative: The exponential rise of speed of available computers made it possible to calculate the electronic structure from first principles of quantum mechanics, thus avoiding any such parameters. They allow to describe wide number of systems on equal footing, gain a better understanding of unexplained phenomena, test proposed theories rapidly, and predict behavior of systems in new conditions, with arbitrary modifications. These features can be combined so that one can even design completely new materials with desired properties based on *ab initio* calculations. Even though exact solutions of the Schrödinger equation for a solid are far beyond capabilities of any computer, there are approximations that make *ab initio* solutions possible while retaining a high accuracy. The present chapter describes mainly the more or less general methods necessary for a particular *ab initio* scheme used in this work.

Atomic Rydberg units will be used throughout the text, hence $\hbar = 2m_e = e^2/2 = 1$, where m_e denotes the electron mass. This defines all other involved units, the length unit is the Bohr radius $a_0 = \frac{\hbar^2}{me^2} = 1$ ($\approx 5.29 \cdot 10^{-11}$ m) and the energy unit is 1 Rydberg $E_{Ryd} = \frac{e^2}{2a_0} = 1$ (≈ 13.6 eV).

2.1 Density functional theory

Early attempts to solve any systems bigger than a few atoms from first principles were stopped by the complexity of many-electron problems. The number of electrons in solids prevents any exact solution and calls for reasonable approximations. In 1964 Hohenberg and Kohn[27] introduced a theory which is nowadays used as a powerful tool to reduce the many-electron ground state problem to a single-electron equivalent. The essence of their formalism is a change-over from many-electron wave functions $\Psi(\mathbf{r}_1, s_1, \mathbf{r}_2, s_2, \dots, \mathbf{r}_N, s_N)$, where \mathbf{r}_i and s_i denote the space and spin coordinates of i -th particle, to one-electron (spinless) densities

defined as

$$n(\mathbf{r}) = \int d^3\mathbf{r}_1 d^3\mathbf{r}_2 \dots d^3\mathbf{r}_N \sum_{s_1, s_2, \dots, s_N} \sum_{i=1}^N |\Psi(\mathbf{r}_1, s_1, \mathbf{r}_2, s_2, \dots, \mathbf{r}_N, s_N)|^2 \delta(\mathbf{r} - \mathbf{r}_i), \quad (2.1)$$

which gave it its name density functional theory (DFT). The first Hohenberg-Kohn theorem states that *the electronic density $n(\mathbf{r})$ of the ground state uniquely determines the external potential $V_{ext}(\mathbf{r})$ up to a trivial additive constant*, and all other quantities are then in principle functionals of the electronic density also. The second theorem provides a recipe how to find the ground state: *The ground state energy corresponding to the given external potential $V_{ext}(\mathbf{r})$ can be found by minimizing the total energy functional with respect to changes in the electron density $n(\mathbf{r})$ while the number of particles is held fixed. The density associated to the minimum total energy is the ground state density.*

Soon after the discovery of the DFT a strong tool for condensed matter calculations based on these two general theorems was introduced, the Kohn-Sham equations [28]. They provide a direct transition from the many-electron Hamiltonian to a single-electron one with a different potential, the Kohn-Sham potential $V_S(\mathbf{r})$. The Schrödinger equation is then replaced by the Kohn-Sham equation:

$$(-\nabla^2 + V_S(\mathbf{r})) \Psi_i(\mathbf{r}) = \epsilon_i \Psi_i(\mathbf{r}), \quad (2.2)$$

where $\Psi_i(\mathbf{r})$ is a one-electron wave function and ϵ_i the corresponding energy eigenvalue.

It is a sum of the original external potential, Hartree-like term and an exchange-correlation potential which incorporates all the many-body effects of the original system.

$$V_S(\mathbf{r}) = V_{ext}(\mathbf{r}) + \int \frac{n(\mathbf{r}')}{|\mathbf{r} - \mathbf{r}'|} dx' + \frac{\delta E_{xc}[n(\mathbf{r})]}{\delta n(\mathbf{r})} \quad (2.3)$$

DFT is in principle exact, but the important exchange-correlation functional is defined in such a way that does not allow us to evaluate it directly. In the end it is necessary to introduce some approximations to it, their choice depends on the specific situation. Surprisingly, even the crudest approximation of the exchange-correlation functional, local density approximation (LDA) [28] or local spin density approximation (LSDA) [29] is sufficient for many situations. It is based on an assumption that the xc-energy per one electron of our system in the position \mathbf{r} is the same function of the local density $n(\mathbf{r})$, as if our system would be entirely homogeneous with the same density. Therefore the L(S)DA exchange-correlation functional is local function, this fact is crucial for the speed of calculations. The xc-energy per one particle $\epsilon_{xc}(n(\mathbf{r}))$ is specified by parameterizations which were obtained from exact calculations of the homogeneous electron gas. The parameterization of Vosko-Wilk-Nusair [30] is adopted in the presented calculations. L(S)DA becomes exact only in the limit of slowly varying spatial density and is therefore suited well to treat electronic charge clouds where the electron density varies by but a small fraction of itself over a de Broglie length of a characteristic electron. There is a systematic overbinding predicted by LDA particularly for the *s-p* bonded systems due to strong energy gradients in these directional bonds. Nevertheless it describes well electronic structure of wide class of materials, many of transition metals and simpler materials, one must avoid i.e. strongly correlated

systems, where LDA+U functional [31] or the dynamical mean-field theory [32] would be appropriate.

Since the whole problem is expressed as a set of integro-differential equations (2.2, 2.3) allowing no analytical solution, it must be solved iteratively. The direct iteration procedure diverges, hence a mixing with previous iterations must be used. Accelerated mixing scheme based on the Anderson mixing [33] was used in calculations presented here. More details can be found in Sec. 10.8.2 of [34].

Note that the key quantity in DFT, the density of states, is closely related to the resolvent of the Hamiltonian H , i.e. its Green's function (GF) [31, 35]:

$$G(z) = (z - H)^{-1} = \int_{-\infty}^{\infty} \frac{1}{z - \epsilon} \delta(\epsilon - H) d\epsilon, \quad (2.4)$$

where z is a complex energy variable. Retarded and advanced Green's functions are defined as $G^r(E) = G(E - i0)$ and $G^a(E) = G(E + i0)$, respectively, where symbol 0 denotes an infinitesimally small value and its sign is important. One can quickly show that $G^a = (G^r)^+$, the imaginary part operator is here commonly redefined so that it in fact provides its antihermitean part: $2i\text{Im} G^r = G^r - G^a$. An important property of Green's functions is the fact that the spectral density $\delta(E - H)$ is directly related to its imaginary part:

$$\delta(E - H) = -\frac{1}{\pi} \text{Im} G^r(E). \quad (2.5)$$

Then one knows also the way to obtain the total density of states defined as

$$N(E) = \text{Tr} \delta(E - H). \quad (2.6)$$

The Green's function may be expressed using the orthogonal and complete set of eigenfunctions $\Psi_i(\mathbf{r})$ and eigenenergies ϵ_i in the form:

$$G(\mathbf{r}, \mathbf{r}', z) = \sum_i \frac{\Psi_i(\mathbf{r}) \Psi_i^*(\mathbf{r}')}{z - \epsilon_i}. \quad (2.7)$$

The local single-particle density $n(\mathbf{r})$ is given by an energy integration of the spectral density at point \mathbf{r} multiplied by the Fermi-Dirac distribution $f(E)$:

$$n(\mathbf{r}) = -\frac{1}{\pi} \int_0^{\infty} f(E) \text{Im} G^r(\mathbf{r}, \mathbf{r}, E) dE. \quad (2.8)$$

In this work calculations are restricted to zero temperature, hence $f(E) = \vartheta(E - E_F)$, where $\vartheta(E)$ denotes the Heavyside function. Since there are poles in the Green's functions on the real axis at points corresponding to eigenvalues of the Hamiltonian, energy integrations over the occupied part of the valence bands are performed here in the complex energy plane along a closed contour starting and ending at the Fermi energy (Chap. 10.3 of [34]). For evaluation of Green's functions near the real energy axis the analytic continuation is used (Chap. 10.4 of [34]).

A lot of discussion concerns the question if DFT as a ground state theory is suitable for transport calculation. The presented work is restricted to the linear response regime,

one can then assume that the single particle potential of the ground state, obtained from DFT, is not changed by the transported electrons. Note that there is a well-known problem with DFT prediction of the band gap in insulating solids or semiconductors. The proper treatment of band gap or finite bias calculations, an excited state DFT extension like the GW approximation [31, 36] or time-dependent DFT [37–39], would be too computationally expensive, but within the linear response regime the corresponding error again should not be significant. More likely the previously mentioned error due to exchange-correlation potential is more important.

2.2 TB-LMTO method

When solving the one-electron Kohn-Sham equation (2.2), the basic point of ES calculation is a reasonable choice of an approximative description of potential and basis in Hilbert space. We adopt here muffin-tin potentials approximated as:

- spherically symmetric potential inside non-overlapping spheres centered on individual nuclei. The positions of its centers are labeled \mathbf{R} . The potential can then be written as

$$V(\mathbf{r}) = V_{\mathbf{R}}(r_{\mathbf{R}}) , \quad r_{\mathbf{R}} \leq s_{\mathbf{R}} , \quad (2.9)$$

where $V_{\mathbf{R}}(r)$ is the potential inside the \mathbf{R} -th atomic sphere of radius $s_{\mathbf{R}}$ (Wigner-Seitz radius), $\mathbf{r}_{\mathbf{R}}$ denotes the difference vector $\mathbf{r} - \mathbf{R}$ and r the magnitude of vector \mathbf{r} .

- constant potential in the interstitial area.

It is combined with the atomic sphere approximation (ASA) - spheres are slightly overlapping, kinetic energy in the interstitial region is neglected. This region is then described by the Laplace equation. These are distinctive approximations in comparison to full potential based methods (with no approximation of the potential shape), but calculations based on it are much less computationally demanding and for a wide class of materials the introduced error is almost negligible. Furthermore full potential methods can hardly be combined with the coherent potential approximation (sec. 2.5.3). The basis may then be constructed as follows [34, 40]:

In the interstitial region the wave function satisfies the Laplace equation. Its solution is expressed in terms of spherical harmonics $Y_L(\tilde{\mathbf{r}})$ and radial amplitudes $a_l(r)$, where $\tilde{\mathbf{r}} = \mathbf{r}/r$ is a unit vector parallel to \mathbf{r} and index L stands for usual angular momentum indices (l, m). The differential equation for $a_l(r)$ leads to the irregular solutions $K_L(\mathbf{r})$ and the regular solutions $J_L(\mathbf{r})$. The former one centered at \mathbf{R} can be expanded in terms of the latter centered at \mathbf{R}' ($\mathbf{R}' \neq \mathbf{R}$), which introduces the so called structure constants $S_{L\mathbf{R}L'\mathbf{R}'}$ describing the geometry of the problem:

$$K_L(\mathbf{r}_{\mathbf{R}}) = \sum_{L'} S_{L\mathbf{R}L'\mathbf{R}'} J_{L'}(\mathbf{r}_{\mathbf{R}'}) . \quad (2.10)$$

The solutions $\phi_{\mathbf{R}l}(r, E) Y_L(\tilde{\mathbf{r}})$ of radial Schrödinger equation for a single isolated sphere with spherically symmetric potential and interstitial region solutions must be matched

smoothly (up to first derivative) on the sphere boundary given by the Wigner-Seitz radius $s_{\mathbf{R}}$. This condition leads to the definition of the potential function $P_{\mathbf{R}\ell}(E)$ and the normalization function $N_{\mathbf{R}\ell}(E)$:

$$P_{\mathbf{R}\ell}(E) = \frac{\{K_{\ell}(r), \varphi_{\mathbf{R}\ell}(r, E)\}}{\{J_{\ell}(r), \varphi_{\mathbf{R}\ell}(r, E)\}} \Big|_{r=s_{\mathbf{R}}}, \quad (2.11)$$

$$N_{\mathbf{R}\ell}(E) = \frac{w}{2} \frac{1}{\{\varphi_{\mathbf{R}\ell}(r, E), J_{\ell}(r)\}} \Big|_{r=s_{\mathbf{R}}}, \quad (2.12)$$

where $\{f_1(r), f_2(r)\}$ is the Wronskian of two radial functions (Eq. 2.20 of [34]). These functions ensure correct matching of the two solutions:

$$N_{\mathbf{R}\ell}(E) \varphi_{\mathbf{R}\ell}(r, E) \rightarrow K_{\ell}(r) - P_{\mathbf{R}\ell}(E) J_{\ell}(r). \quad (2.13)$$

The so called muffin-tin orbitals are constructed in analogy to the partial waves in the multiple scattering theory [41, 42] from the solutions of the two regions:

$$\begin{aligned} \Psi_{\mathbf{R}L}(\mathbf{r}, E) &= N_{\mathbf{R}L}(E) \phi_{\mathbf{R}L}(\mathbf{r}, E) + P_{\mathbf{R}L}(E) J_L(\mathbf{r}_{\mathbf{R}}) && \text{for } r_{\mathbf{R}} \leq s_{\mathbf{R}}, \\ &= K_L(\mathbf{r}_{\mathbf{R}}) && \text{for } r_{\mathbf{R}} \geq s_{\mathbf{R}}. \end{aligned} \quad (2.14)$$

The parts of $\Psi_{\mathbf{R}L}(\mathbf{r}, E)$ inside and outside the \mathbf{R} -th sphere are often referred to as the head and the tail of the muffin-tin orbital (2.14), respectively. For regions $r_{\mathbf{R}'} \leq s_{\mathbf{R}'}$ of muffin-tin orbitals (2.14) the expansion (2.10) is used. Linear combinations of such muffin-tin orbitals satisfy the Schrödinger equation (2.2) provided that the coefficients for $J_L(\mathbf{r}_{\mathbf{R}})$ inside each sphere are canceled by incoming tails (2.10) from other spheres. Non-trivial solutions of this tail cancellation condition corresponds to the following equation:

$$\det(P_{\mathbf{R}L}(E) \delta_{\mathbf{R}L\mathbf{R}'L'} - S_{\mathbf{R}L\mathbf{R}'L'}) = 0, \quad (2.15)$$

where we defined the on-site canonical structure constants trivially such that

$$S_{\mathbf{R}L, \mathbf{R}L'} = 0. \quad (2.16)$$

Eq. (2.15) is often called the KKR-ASA secular equation for its close similarity with the Kohn-Korringa-Rostoker (KKR) matrix derived within the multiple scattering formalism [41, 42]. More details of its derivation can be found in [34]. This equation clearly shows a separation of the problem into two parts: potential functions $P_{\mathbf{R}L}(E)$ that describe the properties of the individual atomic spheres and structure constants related to the positions of the atomic spheres. The disadvantage lies in the non-linear energy dependence of $P_{\mathbf{R}L}(E)$, which will be removed in the next section.

2.2.1 Linearization

Let us recall that solving the Schrödinger equation (2.2) is equivalent to the use of the variational procedure

$$\begin{aligned} \delta \int \psi(\mathbf{r}) [-\Delta + V(\mathbf{r})] \psi(\mathbf{r}) d^3\mathbf{r} &= 0, \\ \int \psi^2(\mathbf{r}) d^3\mathbf{r} &= 1, \end{aligned} \quad (2.17)$$

where the second equation represents a normalization constraint. For simplicity, we use only real wave functions $\psi(\mathbf{r})$ in Eq. (2.17) which is consistent with the use of a real potential $V(\mathbf{r})$ in Eq. (2.2). Due to the constraint in Eq. (2.17), the energy E enters the variational approach as a Lagrange multiplier. If the trial wave function $\psi(\mathbf{r})$ is assumed in the form of a linear combination of basis functions $\chi_i(\mathbf{r})$ which satisfy the correct boundary conditions, the variational principle (2.17) leads to the following eigenvalue problem:

$$\det (E O_{ij} - H_{ij}) = 0 , \quad (2.18)$$

where the Hamiltonian matrix H_{ij} and the overlap matrix O_{ij} are given by

$$\begin{aligned} H_{ij} &= \int \chi_i(\mathbf{r}) [-\Delta + V(\mathbf{r})] \chi_j(\mathbf{r}) d^3\mathbf{r} , \\ O_{ij} &= \int \chi_i(\mathbf{r}) \chi_j(\mathbf{r}) d^3\mathbf{r} . \end{aligned} \quad (2.19)$$

Analogous procedure can be performed for the Schrödinger equation in ASA and allows for a reduction of the original problem (KKR-ASA secular equation) to an eigenvalue problem, provided that the basis function $\chi_i(\mathbf{r})$ are energy independent. The basis can be transformed so that overlap matrix O is replaced by the unit matrix, and an orthogonal Hamiltonian is obtained.

The linearization of the KKR-ASA secular equation corresponds to an approximation of radial amplitudes $\phi_{\mathbf{R}\ell}(r, E)$ by its Taylor expansion in energy truncated after its first two terms (thus linear). The potential function $P_{\mathbf{R}\ell}(E)$ can be written as a fraction of two linear functions, which is uniquely parameterized by three constants $C_{\mathbf{R}\ell}$, $\Delta_{\mathbf{R}\ell}$, $\gamma_{\mathbf{R}\ell}$ called potential parameters. One possible parameterization of $P_{\mathbf{R}\ell}(E)$ is given by

$$P_{\mathbf{R}\ell}(E) = \frac{E - C_{\mathbf{R}\ell}}{\Delta_{\mathbf{R}\ell} + \gamma_{\mathbf{R}\ell} (E - C_{\mathbf{R}\ell})} . \quad (2.20)$$

The exact and parameterized potential functions are required to coincide at the energy expansion point $E_{\nu, R\ell}$ up to the second derivative. The KKR-ASA secular equation (2.15) expressed using the parameterization (2.20) can be reduced to a standard eigenvalue problem of the type

$$\det \left(E \delta_{\mathbf{R}\ell, \mathbf{R}'\ell'} - H_{\mathbf{R}\ell, \mathbf{R}'\ell'}^{\text{orth}} \right) = 0 , \quad (2.21)$$

where the orthogonal Hamiltonian H^{orth} corresponds to a new orthogonal basis of the so-called linearized muffin-tin orbitals.

2.2.2 Tight-binding technique

It is desirable to reduce Hamiltonians with a far reaching interaction between sites (in LMTO corresponding to slowly decaying structural constants) to rather limited ones with interaction only between nearest neighbors. These are analogues of simple tight-binding models, but with *ab initio* calculated parameters that best reproduce the true physics, i.e. give results closest to that of original Hamiltonian. Green's functions (Sec. 2.1) represent a fundamental tool in physical *ab initio* calculations and are crucial for accomplishing this

job. One of its biggest advantages is that it easily allows for perturbation expansion. For an unperturbed Hamiltonian $H = H^0 + U$ an unperturbed Green's function is defined: $(z - H^0) G^0 = 1$. In ASA the unperturbed linear operator corresponds to the following equation for the interstitial area:

$$z + H^0(\mathbf{r}, \mathbf{r}') = \Delta_{\mathbf{r}} \delta(\mathbf{r} - \mathbf{r}') . \quad (2.22)$$

The choice of the unperturbed part of potential is in principle arbitrary, and the tight-binding method is based on a different choice of potential (V_1) that leads to the least extend of interaction. A transformation was found, that redefines the potential (expressed in terms of LMTO potential functions and screening constants) in such way, that Green's functions corresponding to that virtual potential can be easily calculated, and then transformed back to its physical counterpart.

The transformation to a representation with the limited interaction extent is therefore called the screening transformation (inspired by the electrostatic screening) and the corresponding screened potential functions $P_{\mathbf{R}\ell}^\alpha(z)$ and screened structure constants $S_{\mathbf{R}L, \mathbf{R}'L'}^\alpha$ are defined by the following implicit equations:

$$\begin{aligned} P_{\mathbf{R}\ell}^\alpha(z) &= P_{\mathbf{R}\ell}(z) + P_{\mathbf{R}\ell}(z) \alpha_{\mathbf{R}\ell} P_{\mathbf{R}\ell}^\alpha(z) , \\ S_{\mathbf{R}'L', \mathbf{R}''L''}^\alpha &= S_{\mathbf{R}'L', \mathbf{R}''L''} + \sum_{\mathbf{R}L} S_{\mathbf{R}'L', \mathbf{R}L} \alpha_{\mathbf{R}\ell} S_{\mathbf{R}L, \mathbf{R}''L''}^\alpha . \end{aligned} \quad (2.23)$$

In contrast to the vanishing on-site elements $S_{\mathbf{R}L, \mathbf{R}L'}$ of the canonical structure constants, Eq. (2.16), the on-site elements $S_{\mathbf{R}L, \mathbf{R}L'}^\alpha$ of the screened structure constants are generally non-zero and reflect the environment of a particular site \mathbf{R} (crystal field effects).

In LMTO it is customary to define an auxiliary Green's function $g(z)$ closely connected to the original KKR-ASA secular equation (2.15):

$$g(z) = [P(z) - S]^{-1} , \quad (2.24)$$

this object is more suitable for calculations. It is related to the physical Green's function by the formula

$$G(z) = \lambda(z) + \mu(z) g(z) \mu(z) , \quad (2.25)$$

where diagonal matrices $\lambda(z)$ and $\mu(z)$ can be expressed in terms of the potential function. The definitions of screened counterparts of these objects, non-diagonal matrix $g^\alpha(z)$ and diagonal matrices $\mu^\alpha(z)$ and $\lambda^\alpha(z)$, are the same as of the unscreened ones, but related to the screened potential function $P^\alpha(z)$. It is possible to find explicit expressions of $P^\alpha(z)$, $\mu^\alpha(z)$ and $\lambda^\alpha(z)$ in terms of the second-order parameterization (2.20):

$$\begin{aligned} P_{\mathbf{R}\ell}^\alpha(z) &= \frac{z - C_{\mathbf{R}\ell}}{\Delta_{\mathbf{R}\ell} + (\gamma_{\mathbf{R}\ell} - \alpha_{\mathbf{R}\ell})(z - C_{\mathbf{R}\ell})} , \\ \mu_{\mathbf{R}\ell}^\alpha(z) &= \frac{\sqrt{\Delta_{\mathbf{R}\ell}}}{\Delta_{\mathbf{R}\ell} + (\gamma_{\mathbf{R}\ell} - \alpha_{\mathbf{R}\ell})(z - C_{\mathbf{R}\ell})} , \\ \lambda_{\mathbf{R}\ell}^\alpha(z) &= \frac{\gamma_{\mathbf{R}\ell} - \alpha_{\mathbf{R}\ell}}{\Delta_{\mathbf{R}\ell} + (\gamma_{\mathbf{R}\ell} - \alpha_{\mathbf{R}\ell})(z - C_{\mathbf{R}\ell})} . \end{aligned} \quad (2.26)$$

In agreement with the previous statements the physical Green's function $G(z)$ can be shown to be independent of the screening constant α . Note that structure constants of the unscreened system are closely related to unperturbed Green's function of system with reference potential given by that chosen for interstitial area. Their screened counterparts are related to unperturbed Green's function of the "screening" reference potential V_1 . The transformation leading to the least extend of interaction will be denoted as β and the corresponding optimal screening constants $\alpha_{Rl} = \beta_l$ depend for a given lattice only on the cutoff value l_{max} .

The knowledge of the physical Green's function allows one to calculate for example the density of states (Eq. 2.6). For the \mathbf{R} -th atom it is given as (disregarding possible summation over spin states):

$$N_{\mathbf{R}}(E) = -\frac{1}{\pi} \sum_L \text{Im} G_{\mathbf{R}L, \mathbf{R}L}^r(E). \quad (2.27)$$

2.2.3 Lattice translational symmetry, principal layers, leads

For systems with 3D translational symmetry the infinite problem of finding the auxiliary Green's function is easily solvable by means of the lattice Fourier transformation. In this case, the lattice points \mathbf{R} can be expressed in the form $\mathbf{R} = \mathbf{B} + \mathbf{T}$, where the vectors \mathbf{B} denote the basis vectors (non-primitive translations), while the vectors \mathbf{T} refer to the translation vectors (primitive translations). The translational invariance of the system implies the validity of the *Bloch theorem* and leads to the concepts of a reciprocal space, a reciprocal lattice, and Brillouin zones (BZ). The problem can then be transformed from real space to the reciprocal space, where it is diagonal and thus can be solved for each vector \mathbf{k} from the first BZ separately.

In systems with translational symmetry reduced to two dimensions (layered systems) the centers \mathbf{R} of the space-filling atomic spheres can be written as $\mathbf{R} = \mathbf{B} + \mathbf{T}_{\parallel}$, where the vectors \mathbf{B} specify in general individual atomic layers parallel to the interface (including non-trivial basis vectors in the presence of a long-range atomic order within the layers). The translation vectors \mathbf{T}_{\parallel} are parallel to the interface and define a two-dimensional lattice in real space which in turn gives rise to the corresponding two-dimensional reciprocal lattice. Translationally invariant two-center quantities $X_{\mathbf{R}L, \mathbf{R}'L'}$, i.e., matrices in $\mathbf{R}L$ such as $S_{\mathbf{R}L, \mathbf{R}'L'}$ satisfying

$$X_{(\mathbf{R} + \mathbf{T}_{\parallel})L, (\mathbf{R}' + \mathbf{T}_{\parallel})L'} = X_{\mathbf{R}L, \mathbf{R}'L'}, \quad (2.28)$$

can be transformed into quantities $X_{\mathbf{B}L, \mathbf{B}'L'}(\mathbf{k}_{\parallel})$ depending on vector \mathbf{k}_{\parallel} from 2D BZ according to

$$X_{\mathbf{B}L, \mathbf{B}'L'}(\mathbf{k}_{\parallel}) = \sum_{\mathbf{T}_{\parallel}} X_{\mathbf{B}L, (\mathbf{B}' + \mathbf{T}_{\parallel})L'} \exp(i \mathbf{k}_{\parallel} \cdot \mathbf{T}_{\parallel}). \quad (2.29)$$

The inversion of this Fourier transformation (2.29) is usually called a BZ-integration and is traditionally written as

$$\begin{aligned} X_{\mathbf{B}L, (\mathbf{B}' + \mathbf{T}_{\parallel})L'} &= \frac{1}{A_{BZ}} \int_{BZ} X_{\mathbf{B}L, \mathbf{B}'L'}(\mathbf{k}_{\parallel}) \exp(-i \mathbf{k}_{\parallel} \cdot \mathbf{T}_{\parallel}) d^2 \mathbf{k}_{\parallel} \\ &= \frac{1}{N_{\parallel}} \sum_{\mathbf{k}_{\parallel}} X_{\mathbf{B}L, \mathbf{B}'L'}(\mathbf{k}_{\parallel}) \exp(-i \mathbf{k}_{\parallel} \cdot \mathbf{T}_{\parallel}), \end{aligned} \quad (2.30)$$

where A_{BZ} denotes the area of the two-dimensional BZ and N_{\parallel} is related to two-dimensional periodic boundary conditions.

The direction perpendicular to interfaces is obviously excluded from this transformation and the dimension of the transformed matrices $X_{\mathbf{B}L,\mathbf{B}'L'}(\mathbf{k}_{\parallel})$ remains infinite. In order to deal with this situation, the concept of principal layers is introduced. They are constructed from the original atomic layers in the following way: (i) each principal layer contains a finite number of neighboring atomic layers, (ii) the whole system can be considered as a stacking of an infinite sequence of the principal layers labeled by an integer index p , and (iii) the elements $S_{\mathbf{R}L,\mathbf{R}'L'}^{\beta}$ of the tight-binding structure constants are non-zero only for sites \mathbf{R} and \mathbf{R}' belonging to the same or neighboring principal layers. The sites \mathbf{R} of a given system can be then written in a form $\mathbf{R} \equiv (p, \mathbf{B}, \mathbf{T}_{\parallel})$ where p is the index of the principal layer, \mathbf{B} denotes the corresponding basis vector (mostly atomic layer) in the p -th principal layer, and \mathbf{T}_{\parallel} is a 2D translation vector. The tight-binding LMTO representation becomes particularly useful in that situation as it reduces the minimum number ν of atomic layers comprised in one principal layer. In the case of the most closely-packed planes, fcc(111) and bcc(110), the principal layer consists only of a single atomic layer, in other low-index cases it is 2 or 3 layers (Tab. 3.4 of [34]).

In practice the whole system is always truncated to a region of finite thickness, which can be calculated in finite time, the so called intermediate region. Outside this region the system is assumed to be already solved and described by a bulk-like electronic structure. It is desirable that the change of self-consistent electronic structure of boundary principal layers from its bulk counterpart is negligible, so that the two regions are smoothly matched without creating any artificial interface. Therefore a sufficiently high number of layers of the same composition as the outer region must be included in the intermediate region. Note that the role of contributions from truncated area to the intermediate region Hamiltonian is very important, without them the system would be just embedded in a vacuum with completely reflecting boundaries. For transport calculations the truncated part represents leads, which allow an influx and outflux of electrons to and out of the system. Results should not depend on a particular choice of truncation positions inside the bulk-like regions, this is studied in detail in Appendix B. These two semi-infinite parts of the system will be referred to as the left (\mathcal{L}) and right (\mathcal{R}) lead.

The Green's function corresponding to the intermediate region Hamiltonian can then be found by means of the partitioning technique [43] for matrix inversions. We start with 2D lattice Fourier transform of Eq. (2.24) and introduce the matrix

$$M^{\beta}(\mathbf{k}_{\parallel}, z) = P^{\beta}(z) - S^{\beta}(\mathbf{k}_{\parallel}), \quad (2.31)$$

which describes the whole system and is used to calculate the auxiliary Green's function:

$$M^{\beta}(\mathbf{k}_{\parallel}, z) g^{\beta}(\mathbf{k}_{\parallel}, z) = 1. \quad (2.32)$$

The auxiliary Green's function at layer p (omitting \mathbf{k}_{\parallel} - and z -dependences) is then given as:

$$g_{p,p}^{\beta} = \left\{ P_p^{\beta} - S_{p,p}^{\beta} - S_{p,p-1}^{\beta} \left[(M^{\beta,p,<})^{-1} \right]_{p-1,p-1} S_{p-1,p}^{\beta} - S_{p,p+1}^{\beta} \left[(M^{\beta,p,>})^{-1} \right]_{p+1,p+1} S_{p+1,p}^{\beta} \right\}^{-1}, \quad (2.33)$$

where $M^{\beta,p,<}(\mathbf{k}_{\parallel}, z)$ and $M^{\beta,p,>}(\mathbf{k}_{\parallel}, z)$ are semi-infinite block submatrices of the matrix $M^{\beta}(\mathbf{k}_{\parallel}, z)$ containing only layers p' , where $p' > p$ or $p' < p$, respectively.

It motivates the definition of the surface Green's functions [44, 45] for semi-infinite systems, i.e. leads. Let us assume that the intermediate region comprises principal layers p , $1 \leq p \leq N$. Layers $p_{\mathcal{L}}$ ($p_{\mathcal{L}} < 1$) and $p_{\mathcal{R}}$ ($p_{\mathcal{R}} > N$) then correspond to the left and right lead, respectively. Let $M_{\mathcal{L}}^{\beta}(\mathbf{k}_{\parallel}, z)$ denote the semi-infinite square submatrix for layers $p_{\mathcal{L}}$ of the whole system matrix $M^{\beta}(\mathbf{k}_{\parallel}, z)$. The surface Green's function (SGF) $\mathcal{G}_{\mathcal{L}}^{\beta}(\mathbf{k}_{\parallel}, z)$ of the considered semi-infinite stacking of principal layers is then defined as the $(p_{\mathcal{L}}, p_{\mathcal{L}})$ subblock of the inverted semi-infinite submatrix $M_{\mathcal{L}}^{\beta}(\mathbf{k}_{\parallel}, z)$:

$$\mathcal{G}_{\mathcal{L}}^{\beta}(\mathbf{k}_{\parallel}, z) = \left\{ \left[M_{\mathcal{L}}^{\beta}(\mathbf{k}_{\parallel}, z) \right]^{-1} \right\}_{p_{\mathcal{L}}, p_{\mathcal{L}}}, \quad (2.34)$$

which is independent of the particular choice of $p_{\mathcal{L}}$ due to the homogeneity of leads. Let us remind that this SGF is a matrix in \mathbf{BL} -indices and that analogously a SGF $\mathcal{G}_{\mathcal{R}}^{\beta}(\mathbf{k}_{\parallel}, z)$ for the right semi-infinite lead can be defined. Eq. (2.33) allows to evaluate auxiliary Green's function in the intermediate region using only intermediate region properties and surface Green's functions for both leads. The formula for the intermediate region auxiliary Green's function $g_{p,p'}^{\beta}(\mathbf{k}_{\parallel}, z)$ can be recast into the form:

$$g_{p,p'}^{\beta}(\mathbf{k}_{\parallel}, z) = \left\{ \left[P_p^{\beta}(z)\delta_{p,p'} - S_{p,p'}^{\beta}(\mathbf{k}_{\parallel}) - \Sigma^{\beta}(\mathbf{k}_{\parallel}, z) \right]^{-1} \right\}_{p,p'}, \quad (2.35)$$

where

$$\begin{aligned} \Sigma^{\beta}(\mathbf{k}_{\parallel}, z) &= \Sigma_{\mathcal{L}}^{\beta}(\mathbf{k}_{\parallel}, z) + \Sigma_{\mathcal{R}}^{\beta}(\mathbf{k}_{\parallel}, z), \\ \Sigma_{\mathcal{L}}^{\beta}(\mathbf{k}_{\parallel}, z) &= S_{1,0}^{\beta}(\mathbf{k}_{\parallel}) \mathcal{G}_{\mathcal{L}}^{\beta}(\mathbf{k}_{\parallel}, z) S_{0,1}^{\beta}(\mathbf{k}_{\parallel}), \\ \Sigma_{\mathcal{R}}^{\beta}(\mathbf{k}_{\parallel}, z) &= S_{N,N+1}^{\beta}(\mathbf{k}_{\parallel}) \mathcal{G}_{\mathcal{R}}^{\beta}(\mathbf{k}_{\parallel}, z) S_{N+1,N}^{\beta}(\mathbf{k}_{\parallel}). \end{aligned} \quad (2.36)$$

The influence of leads is represented by these operators derived simply from SGF; they are in fact self-energies representing the perturbation of the intermediate system due to presence of leads [19]. Note that due to properties of principal layers they act only in the corners $(1, 1)$ and (N, N) of the intermediate region subblock of the matrix M , in this text they are used as the matrix in layers space as well as its corner: $\Sigma_{\mathcal{L} p,p'}^{\beta}(\mathbf{k}_{\parallel}, z) = \Sigma_{\mathcal{L}}^{\beta}(\mathbf{k}_{\parallel}, z)\delta_{p,1}\delta_{p',1}$, $\Sigma_{\mathcal{R} p,p'}^{\beta}(\mathbf{k}_{\parallel}, z) = \Sigma_{\mathcal{R}}^{\beta}(\mathbf{k}_{\parallel}, z)\delta_{p,N}\delta_{p',N}$. Various methods of SGF evaluation can be found in Sec. 10.6 of [34], here we use the renormalization-decimation technique [46], which is best suited for simulations with very low value of $\text{Im } z$. The screening transformation superscript β will be omitted in further text as all relevant quantities are assumed to be expressed in the least-extend TB representation unless otherwise stated.

2.3 Spin-dependent transport in layered nanostructures

In systems with collinear magnetizations electrons spin direction must be also collinear to it, hence conductances of electrons restricted to spins parallel or antiparallel to the specified

magnetization describe fully its spin-dependent transport properties within linear response regime (see Chap. 5 for a more general situation). If spin flip is neglected, transport in one spin channel is independent of the other one and it is sufficient to define only two conductances C_\uparrow , C_\downarrow for the two spin channels, where the first typically corresponds to the more conducting (majority) channel. This approximation is referred to as the two-current model [47, 48], but do not confuse it with an assumption of an equal conductance per all \mathbf{k}_\parallel vectors, which is also sometimes labeled by this name [49]. The spin polarization of current is defined as $P = (C_\uparrow - C_\downarrow) / (C_\uparrow + C_\downarrow)$.

Simple magnetic multilayer can be built according to Fig. 2.1, it consists of alternating ferromagnetic (FM) and nonmagnetic (NM) layers. Current can flow through the structure either in the in-plane direction (CIP) or perpendicular to planes (CPP). The latter case leads to higher MR values and will be described here. The origin of GMR effect in multilayers can be roughly explained by the two-current and series resistor model [48, 50]: In one of possible multilayer realizations *the interlayer exchange coupling* [1] forces the magnetic layers to align antiparallel (AP) under zero magnetic field (Fig. 2.1 (a)). An applied magnetic field reverts all magnetizations to one direction (parallel magnetizations - PM state, Fig. 2.1 (b)). Let us assume that all FM and NM layers are the same and denote the resistances of NM | FM \uparrow | NM and NM | FM \downarrow | NM part of system for spin- \uparrow electrons as R_{maj} , R_{min} , respectively. Spin- \downarrow electrons experience the oppositely assigned resistances, i.e. R_{maj} for FM \downarrow and vice versa. If $R_{maj} \neq R_{min}$, in the PM arrangement electrons in the majority spin channels always experience only the more conducting channel, while in the AP arrangement all electrons meet layers with alternating R_{maj} and R_{min} regardless of its spin. We introduce the average resistance \bar{R} and spin asymmetry $\beta(\beta = P / (P + 1))$, so that $R_{maj} = 2\bar{R}(1 - \beta)$ and $R_{min} = 2\bar{R}(1 + \beta)$. The resistance of the PM arrangement is $R_{PM} = \bar{R}(1 - \beta^2)$ per two consecutive FM layers, while for the AP arrangement it is $R_{AP} = \bar{R}$. The first one is obviously bigger for $\beta \neq 0$; we will typically work here with the corresponding conductances $C_{PM} = R_{PM}^{-1}$, $C_{AP} = R_{AP}^{-1}$. AP / PM switching can be also accomplished by employing consecutive FM layers with different switching fields or using some other way to pin a subset of FM layers to a different magnetization direction than other ones. The simplest structures where magnetoresistance can be achieved comprise only two FM layers (NM | FM1 | NM | FM2 | NM junction), which we will refer to as spin valves here. The magnetoresistance ratio is defined in this work as

$$\gamma = \frac{C_{PM}}{C_{AP}} - 1. \quad (2.37)$$

The nonmagnetic spacer between FM layers can be replaced by a semiconductor or an insulator. Such structure comprising only two magnetic layers (FM1 and FM2) is referred to as the magnetic tunnel junction (MTJ). The corresponding analogue of GMR is the tunneling magnetoresistance (TMR) [3, 51], first successful realizations with non-negligible TMR ratio at room temperature were realized in 1995 [52, 53], inspired by the success of the GMR. Its size is determined mainly by the spin polarization of density of states at the Fermi energy: $\tilde{P} = (N_\uparrow - N_\downarrow) / (N_\uparrow + N_\downarrow)$. This allows to formulate a very simplified relation for it, Julliere's formula (named after the author of first observation of spin-dependent

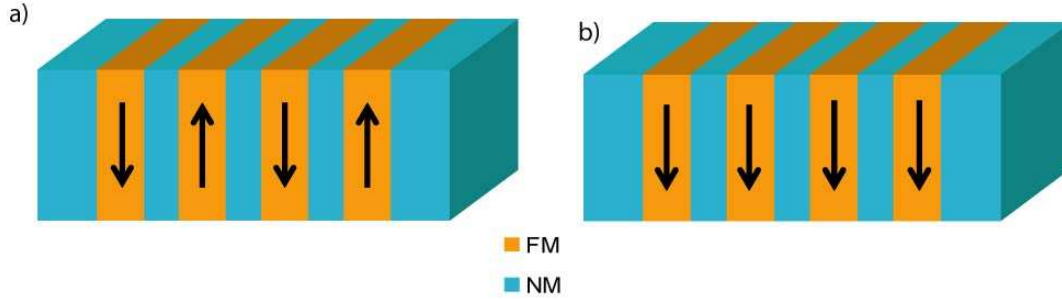


Figure 2.1: Magnetic multilayers: a) antiparallel magnetic alignment; b) parallel magnetic alignment

scattering in magnetic tunnel junctions [54]):

$$\gamma = \frac{2\tilde{P}_{FM1}\tilde{P}_{FM2}}{1 - \tilde{P}_{FM1}\tilde{P}_{FM2}}. \quad (2.38)$$

This approach is in fact based on ideas of the tunnel Hamiltonian theory [55]. Similarly to the series resistor model, there is no momentum dependence. Realistic calculations must take into account the *band structure* (momentum dependent property), its mismatch between different layers is often the most important factor determining the conductance and causing the nonzero spin asymmetry (polarization) needed for GMR to work.

Electron transport is a non stationary process caused by an external perturbation. Various sophisticated approaches to its evaluation exist. One of basic tools for quantitative transport description is the Boltzmann equation [31]. This is a semiclassical approach and cannot describe some subtle quantum effects neither can it derive the relation between current and external potential without phenomenological parameters. However it is well sufficient to get some quick qualitative understanding of some phenomena, or to examine areas which are not yet accessible for more accurate theories described further. The simple structure of this model allows to take into account quickly many additional processes if their phenomenological description in terms of Boltzmann collision term is available. Probably the most successful framework for quantitative understanding of spin transport phenomena based on it is the Valet-Fert model [56] with a collision term accounting for the spin-flip scattering. The latter mechanism provides an extension of the two-current series-resistor model [48, 50] and it has important consequences for layer thicknesses comparable to the spin-diffusion length.

For microscopic/mesoscopic devices a more appropriate formalism has been developed: the Landauer-Büttiker scattering theory [19, 57–59]. The current through a conductor is expressed here in terms of a probability T that an electron can transmit through it, this idea leads to the famous Landauer formula for conductance

$$C = \frac{e^2}{h} \sum_{n,m} T_{n,m}, \quad (2.39)$$

where the sum runs over all possible incoming and outgoing states. Important consequence of this formula is the non-zero resistance even for a system without scattering (the so

called ballistic conductor), where the conductance is limited by the finite number of incoming/outgoing channels. This phenomenon, the Sharvin or contact resistance, may play role only in nanoconstrictions. If one would want to obtain the resistance of multiple interfaces from the knowledge of each interface resistance within the spirit of the series resistor model, he must take into account the fact that Sharvin resistance is then added to each interface as an artifact of the Landauer formulation. An advantage of the Landauer approach is the fact that it allows for an extension to finite bias situations, where it in fact resembles the non-equilibrium Green's function formalism [19]. Within linear response regime the Landauer formalism has been shown to be equivalent [60] to the Kubo theory [17] employed in our calculations and presented in the next section.

2.4 Conductance from the linear response theory

The conductance calculation is restricted here to the static (zero-frequency) case and the linear response regime, where the external perturbation causes only an infinitesimal shift of system from its ground state. The perturbation operator \tilde{B} acts as an additional term in the Hamiltonian: $H \rightarrow H + e^{\alpha t} \tilde{B}$, where $\alpha \rightarrow 0^+$ ensures good analytical properties for a derivation in terms of Green's functions. The observable in question is associated with a hermitean operator A , its Heisenberg representation is $A(t) = e^{iHt} A e^{-iHt}$. Their linear response coefficient can be obtained from the general Kubo formula [18, 35] and is given by

$$C_{A\tilde{B}} = -i \lim_{\alpha \rightarrow 0^+} \int_{-\infty}^{\infty} dt e^{-\alpha t} \vartheta(t) \text{Tr} \left\{ f(H) \left[A(t), \tilde{B} \right] \right\}. \quad (2.40)$$

We define an operator

$$\tilde{A} = \dot{\tilde{B}} = -i \left[\tilde{B}, H \right], \quad (2.41)$$

and an operator B for which

$$A = \dot{B} = -i \left[B, H \right]. \quad (2.42)$$

An important achievement of the linear response theory, the Kubo formula for conductance [17], is employed to express $C_{A\tilde{B}}$ conveniently. In order to derive the charge conductance, one typically starts with its canonic form:

$$C_{A\tilde{B}}^{(C)} = \pi \int d\xi f'(\xi) \text{Tr} \left\{ A \delta(\xi - H) \tilde{A} \delta(\xi - H) \right\}. \quad (2.43)$$

In this work we will deal also with other kinds of linear response than the charge conductance. A more general form of the Kubo formula must then be used because some common assumptions must not be valid, although the result may also be called conductance. Therefore we sketch here a derivation starting from general formula (2.40). Operator $A(t)$ is replaced by its Schrödinger representation, two energy integrations are employed for the integrand $C'_{A\tilde{B}}$ of (2.40):

$$C'_{A\tilde{B}} = e^{-\alpha t} \vartheta(t) \int_{-\infty}^{\infty} d\xi \int_{-\infty}^{\infty} d\eta e^{i(\xi - \eta)t} \text{Tr} \left\{ f(H) \left[\delta(\xi - H) A \delta(\eta - H), \tilde{B} \right] \right\}, \quad (2.44)$$

where the δ -function properties allows to replace H by energy arguments:

$$C'_{A\tilde{B}} = e^{-\alpha t} \vartheta(t) \int_{-\infty}^{\infty} d\xi \int_{-\infty}^{\infty} d\eta e^{i(\xi-\eta)t} [f(\xi) - f(\eta)] \text{Tr} \left\{ \delta(\xi - H) A \delta(\eta - H) \tilde{B} \right\}. \quad (2.45)$$

Going back to complete $C_{A\tilde{B}}$ and integrating over time leads to the following equation:

$$C_{A\tilde{B}} = \lim_{\alpha \rightarrow 0^+} \int_{-\infty}^{\infty} d\xi \int_{-\infty}^{\infty} d\eta \frac{f(\xi) - f(\eta)}{\xi - \eta + i\alpha} \text{Tr} \left\{ \delta(\xi - H) A \delta(\eta - H) \tilde{B} \right\}. \quad (2.46)$$

Using the definition of Green's functions (2.4) yields this formula:

$$C_{A\tilde{B}} = \lim_{\alpha \rightarrow 0^+} \int d\xi f(\xi) \text{Tr} \left\{ \delta(\xi - H) A G(\xi + i\alpha) \tilde{B} + G(\xi - i\alpha) A \delta(\xi - H) \tilde{B} \right\}. \quad (2.47)$$

The evaluation of the limit $\alpha \rightarrow 0^+$ is complicated by the fact that the operator \tilde{B} can be non-zero in an infinitely large area in contrast to the operator A . Therefore it is desirable to recast Eq. (2.47) into form explicitly restricted by operators A or \tilde{A} , which can be assumed to be localized in a finite region.

The general derivation of $C_{A\tilde{B}}$ shown in Appendix A leads to the following formula:

$$C_{A\tilde{B}} = C_{A\tilde{B}}^{(1)} + C_{A\tilde{B}}^{(R)}, \quad (2.48)$$

where

$$C_{A\tilde{B}}^{(1)} = -\frac{i}{2} \int d\xi f'(\xi) \text{Tr} \left\{ A \delta(\xi - H) \tilde{A} G(\xi - i0) - A G(\xi + i0) \tilde{A} \delta(\xi - H) \right\}, \quad (2.49)$$

and the remaining part is

$$C_{A\tilde{B}}^{(R)} = \frac{1}{4\pi} \int d\xi f(\xi) \text{Tr} \left\{ A G(\xi + i0) \tilde{A} G^2(\xi + i0) - A G^2(\xi + i0) \tilde{A} G(\xi + i0) \right. \\ \left. - A G(\xi - i0) \tilde{A} G^2(\xi - i0) - A G^2(\xi - i0) \tilde{A} G(\xi - i0) \right\}. \quad (2.50)$$

A more transparent transcription of $C_{A\tilde{B}}^{(R)}$ is available, it is decomposed into two terms and the total response coefficient is then given as

$$C_{A\tilde{B}} = C_{A\tilde{B}}^{(1)} + C_{A\tilde{B}}^{(2)} + C_{A\tilde{B}}^{(3)}, \quad (2.51)$$

where

$$C_{A\tilde{B}}^{(2)} = -\frac{1}{2} \int d\xi f'(\xi) \text{Tr} \left\{ \delta(\xi - H) (B\tilde{A} - \tilde{B}A) \right\}, \quad (2.52)$$

$$C_{A\tilde{B}}^{(3)} = -\frac{i}{2} \int d\xi f(\xi) \text{Tr} \left\{ \delta(\xi - H) (\tilde{B}B - B\tilde{B}) \right\}. \quad (2.53)$$

The term $C_{A\tilde{B}}^{(1)}$ is equivalent to $C_{A\tilde{B}}^{(C)}$ in some situations. One can see that additional terms to formula (2.43) appeared, $C_{A\tilde{B}}^{(2)}$ is for example present when Hall resistances are derived

[61]. Note that $C_{A\tilde{B}}^{(3)}$ contains the Fermi-Dirac distribution instead of its derivative, hence even for zero temperature the energy integration would not reduce just to the Fermi energy.

There is a general rule which guarantees that the terms $C_{A\tilde{B}}$ reduces only to $C_{A\tilde{B}}^{(1)}$, which becomes equivalent to Eq. (2.43). It is valid even for case when an operator B cannot be found for A and the decomposition (2.51) is not possible. In order to satisfy this rule, there must exist a regular operator U and a scalar $\epsilon \in \{-1, 1\}$ so that the operators A, \tilde{B}, H have the following properties with respect to its transposition:

$$\begin{aligned} H^T &= UHU^{-1}, \\ \tilde{B}^T &= \epsilon U\tilde{B}U^{-1}, \\ A^T &= -\epsilon UAU^{-1}. \end{aligned} \quad (2.54)$$

To prove this, we first note that assumptions (2.54) lead quickly to $G^T(z) = UG(z)U^{-1}$ and another similar relation:

$$\tilde{A}^T = -i(\tilde{B}H - H\tilde{B})^T = -i\epsilon U(H\tilde{B} - \tilde{B}H)U^{-1} = -\epsilon U\tilde{A}U^{-1}. \quad (2.55)$$

Note that the first and third term in Eq. (2.50) differ only by the choice of energy substitution $z = \xi + i0$ or $z = \xi - i0$. We label the common expression for these terms as $C_{A\tilde{B}}^{(R,1)}(z)$, and analogously $C_{A\tilde{B}}^{(R,2)}(z)$ for the second and fourth term. Employing the general identity $\text{Tr} M = \text{Tr} M^T$ for the first one we find

$$C_{A\tilde{B}}^{(R,1)}(z) = \text{Tr}\{AG(z)\tilde{A}G^2(z)\} = \text{Tr}\{[G^2(z)]^T\tilde{A}^TG^T(z)A^T\}. \quad (2.56)$$

Substitution of the already known transposes of involved matrices shows that the term (2.56) turns into the second (or fourth) term $C_{A\tilde{B}}^{(R,2)}(z)$ of Eq. (2.50):

$$C_{A\tilde{B}}^{(R,1)}(z) = \text{Tr}\{AG^2(z)\tilde{A}G(z)\} = C_{A\tilde{B}}^{(R,2)}(z).$$

These two terms with opposite sign cancel and $C_{A\tilde{B}}^{(R)}$ vanishes.

One example of linear response satisfying conditions (2.54) is described in the following section, other can be found in Sec. 4.3 and 5.2.1.

2.4.1 Charge conductance

The starting point is the choice of the position operator $X(\mathbf{r})$ as the response operator: $B = X(\mathbf{r})$. If the operator $X(\mathbf{r})$ is defined as a Cartesian coordinate at a point \mathbf{r} , the operator A then equals the velocity operator, which is useful to examine charge conductivity. If the operator $X(\mathbf{r})$ is defined as a projector to a given subspace, the operator $A = -i[X, H]$ gives the flux from/into the subspace, which corresponds to calculation of charge conductance through the surface of the subspace. $\tilde{B} = \varphi(\mathbf{r})$ is a profile of a spin-independent external electrostatic field. One can quickly show that this kind of linear response fulfills the conditions (2.54), this is achieved with the choice $U = 1$ and $\epsilon = 1$.

Substituting these operators into Eq. (2.43) leads to the Kubo formula for conductance (or conductivity) :

$$C = -2\pi \int d\xi f'(\xi) \text{Tr} \{ [X, H] \delta(\xi - H) [\varphi, H] \delta(\xi - H) \} , \quad (2.57)$$

where the additional pre-factor 2 comes from atomic units expression of electron charge e^2 present in conductance formula. Only zero temperature conductance is considered here, hence $f'(E) = -\delta(E - E_F)$ and the energy integration reduces to an evaluation at the Fermi energy. Substitution of Eq. (2.5) to (2.57) leads to:

$$C(E_F) = -\frac{2}{\pi} \text{Tr} \{ \text{Im} G^r(E_F) [X, H] \text{Im} G^r(E_F) [\varphi, H] \} . \quad (2.58)$$

In the LMTO method the commutator $[X, H]$ reduces to $[X, S]$ simply because the remaining terms from H are diagonal in position as well as X . The same is valid for $[\varphi, H]$. Its version expressed in an arbitrary LMTO representation α is given as

$$C(E_F) = -\frac{2}{\pi} \text{Tr} \{ \text{Im} g^\alpha(E_F + i0) [X, H^\alpha] \text{Im} g^\alpha(E_F + i0) [\varphi, H^\alpha] \} , \quad (2.59)$$

and it is invariant with respect to the representation (denoted by α) [62]. It has been proved that this formula is correct up to second order in energy $\epsilon = E - E_\nu$ [62]. The derivation was actually done for a form with a commutator $[X, S^\alpha]$ instead of $[\varphi, H^\alpha]$, but the same argumentation can be applied. The index related to LMTO representation (α) will be omitted in the subsequent text.

The quantity of interest is the CPP charge conductance in layered systems. Note that the system is always attached to leads which allow electrons to enter or leave the structure. They are described by surface Green's function as was explained in Sec. 2.2.3. The trace in Eq. (2.59) is restricted to the intermediate region, where Green's functions fulfill Eq. (2.35). It allows us to write

$$(g^r - g^a) = g^r (\Sigma^r - \Sigma^a) g^a = g^a (\Sigma^r - \Sigma^a) g^r , \quad (2.60)$$

where we introduced the retarded and advanced form of self-energy (embedding potential of leads, Eq. 2.36) in the same way as for the corresponding Green' functions. The anti-hermitean part of embedding potentials (self-energies) $\Sigma_{\mathcal{L}, \mathcal{R}}$ will be denoted here as $\mathcal{B}_{\mathcal{L}, \mathcal{R}}$ instead of the commonly used Γ in order not to confuse it with vertex corrections Γ in the next part:

$$\mathcal{B} = i(\Sigma^r - \Sigma^a) , \quad (2.61)$$

$$\mathcal{B}_{\mathcal{L}, \mathcal{R}} = i(\Sigma_{\mathcal{L}, \mathcal{R}}^r - \Sigma_{\mathcal{L}, \mathcal{R}}^a) . \quad (2.62)$$

Eq. (2.59) can be then rewritten as:

$$C(E_F) = -\frac{1}{2\pi} \text{Tr} \{ \mathcal{B} g^r [X, H] g^r \mathcal{B} g^a [\varphi, H] g^a \} . \quad (2.63)$$

Employing $[X, \Sigma^r] = 0$ we find that

$$g^r [X, H] g^r = g^r [X, E - H - \Sigma^r] g^r = g^r X - X g^r , \quad (2.64)$$

with a similar relation valid for $[\varphi, \Sigma^a]$ this leads to

$$C(E_F) = -\frac{1}{2\pi} \text{Tr} \{ \mathcal{B}(g^r X - X g^r) \mathcal{B}(g^a \varphi - \varphi g^a) \}. \quad (2.65)$$

From this equation it is clear that only the (constant) values of the functions $X(\mathbf{r})$ and $\varphi(\mathbf{r})$ inside the leads enter the resulting conductance, it is therefore independent of the actual spatial profile of the potential. Note that this statement need not hold for ac conductance, as was shown for a quantum wire in [63]. In order to obtain conductance through the intermediate region we consider Eq. (2.61) and take the profiles such that the unitary field is generated inside the left lead ($X = 0$ and $\varphi = -1$ there) while the response to it (current) is measured inside the right lead ($X = 1$ and $\varphi = 0$ there) :

$$\mathcal{B}X = X\mathcal{B} = \mathcal{B}_{\mathcal{R}}, \quad \mathcal{B}\varphi = \varphi\mathcal{B} = -\mathcal{B}_{\mathcal{L}}, \quad X\mathcal{B}\varphi = \varphi\mathcal{B}X = 0. \quad (2.66)$$

Charge unit e was already employed in (2.57), which justifies the choice of unitary potential and current as 1. The negative value of the chosen ansatz for φ ensures that commutators $[X, H]$, $[\varphi, H]$ picks elements of H going in one direction with the same sign ($S_{p,p'}$ for $p' > p$ and $-S_{p,p'}$ for $p' < p$) consistently with the physical meaning of current. Relations (2.66) yield a compact Caroli-like [64] expression for conductance:

$$C(E_F) = -\frac{1}{2\pi} \text{Tr} \{ \mathcal{B}_{\mathcal{R}} g^r \mathcal{B}_{\mathcal{L}} g^a + \mathcal{B}_{\mathcal{L}} g^r \mathcal{B}_{\mathcal{R}} g^a \}. \quad (2.67)$$

It is a sum of two terms of the form

$$\begin{aligned} C(E_F) &= -C(E_F + i0, E_F - i0) - C(E_F - i0, E_F + i0), \\ C(z_\mu, z_\nu) &= \frac{1}{2\pi} \text{Tr} \{ g(z_\mu) \mathcal{B}_{\mathcal{L}} g(z_\nu) \mathcal{B}_{\mathcal{R}} \}. \end{aligned} \quad (2.68)$$

If the system is invariant with respect to the reversal of time, the terms $C(E_F + i0, E_F - i0)$ and $C(E_F - i0, E_F + i0)$ are equal. In transport calculations presented here the values $\pm 10^{-7}$ Ry were taken as the imaginary parts of energy arguments z_μ and z_ν .

An alternative derivation of this formula can be seen in the appendix of Ref. [65]. The definition of surface Green's functions (SGF) [34] together with the partitioning technique [66] allows one to derive relations (A16 of Ref. [65]), with which the products of current operators and system Green's functions are replaced by embedding potentials $\Sigma_{L,R}$ (Eq. 2.36).

The formula (2.68) is obviously analogous to the transmission probability in the Landauer formulation of transport [19]. The relation between the Kubo formulation and transmission matrices has been examined in [67]. If, for example, Eq. (2.68) is applied to a pure infinite wire (ballistic conductor), its contact resistance is obtained as in the Landauer point of view [19].

For spin-dependent systems within the two-current model (Sec. 2.3) the two spin channels are independent. Spin-resolved conductances C_\uparrow, C_\downarrow can be derived directly from formula (2.68), where Green's functions for the corresponding spin state are employed:

$$C_s(z_\mu, z_\nu) = \frac{1}{2\pi} \text{tr} (g_s(z_\mu) \mathcal{B}_{\mathcal{L}} g_s(z_\nu) \mathcal{B}_{\mathcal{R}}), \quad s = \uparrow, \downarrow. \quad (2.69)$$

All relations valid for Eq. (2.68) are valid also for (2.69) as long as no spin-dependent operations are involved.

2.5 Substitutional disorder

Interfaces between two different materials are hardly completely clean and distinct. Because of manufacturing limitations and additional thermal processes, atoms of one species (A) can diffuse to the other one (B) and vice versa. This interface interdiffusion creates substitutional disorder at few monolayers near the interface. It means that its lattice sites are occupied by one of atoms Q , where $Q \in \{A, B\}$, but lattice geometry remains unchanged. Generally the number of species Q is unlimited. The occupation of the site \mathbf{R} by the atom Q is described by $\eta_{\mathbf{R}}^Q \in \{0, 1\}$, and $\sum_Q \eta_{\mathbf{R}}^Q = 1$.

Alloys represent substitutional disorder not limited to only a few monolayers. Bulk disorder can be intrinsic property of the material, it can also be a defect present under some conditions. In any case its presence has often a strong impact on transport and other properties and may lead to some unique phenomena [68].

2.5.1 Configurational averages

One particular realization of occupations of the lattice sites is called a configuration \mathcal{C} . Physical observables are obtained as averages of the observable's mean value $\langle X \rangle$ over all possible configurations weighted with their probabilities $p(\mathcal{C})$:

$$\langle\langle X \rangle\rangle = \sum_{\mathcal{C}} p(\mathcal{C}) \langle X \rangle(\mathcal{C}) . \quad (2.70)$$

Common assumption here is complete randomness of occupations, given by probabilities (concentrations) $c_{\mathbf{R}}^Q$, with no short range order or correlations. The probability of one configuration is then given as:

$$p(\mathcal{C}) = \prod_{\mathbf{R}} \left(\sum_Q c_{\mathbf{R}}^Q \eta_{\mathbf{R}}^Q \right) . \quad (2.71)$$

Very useful tool for dealing with substitutional disorder are again Green's functions. Their configurational averages $\langle G \rangle$ are related to the averaged particle density and thus they allow us to extract relevant observables due to the Hohenberg-Kohn's first theorem (Sec. 2.1). Their advantage is the possibility to treat the random configuration-dependent part of Hamiltonian as a perturbation U : $H(\mathcal{C}) = H_0 + U(\mathcal{C})$, where H_0 is configuration-independent. Note that the configurationally averaged Green' function $\langle G \rangle$ obtained by substitution into Eq. (2.70) has again the full translational symmetry of the original lattice.

For disordered systems the property called Bloch spectral function becomes particularly useful. In the case of a system with a 3D or 2D translational symmetry, one can transform the density of states (Eq. 2.27) to reciprocal space and obtain the Bloch spectral function, which allows to examine how different parts of the BZ contribute to the total density of states. In bulk crystals without substitutional disorder discrete bands are formed and the Bloch spectral function is reduced to δ -functions located at crystal eigenenergies, which correspond to its *band structure*. For disordered systems the peaks in the Bloch spectral function are no longer δ -functions, their extent and relation to the peaks of the original pure materials may be important to understand properties of the disordered system. Energy bands of such system are thus not discrete.

The main problem is to find desired configurational averages without evaluating all possible configurations. There are simple methods available: virtual crystal approximation (VCA), where the random perturbing potential U is replaced by its average; and self-consistent Born approximation (SCBA), which corresponds to first order of perturbation theory [18]. However, these cannot describe real physical properties of disordered systems quantitatively and cannot even catch some qualitative properties, for example the creation of split bands for strong disorder (big $|U_A - U_B|$ as compared to the bandwidth).

2.5.2 Supercell method

One possible approach to this problem is stochastic: to evaluate a number of possible random configurations chosen with respect to prescribed concentrations and find its average. Infinite systems must be split into small clusters (supercells) with size allowing it to be solved in real space [69]. A random configuration is generated for one supercell, which is then assumed to be repeated infinitely across the lattice (or a layer in case of 2D translational invariance). This defines boundary conditions of the supercell as periodic. The splitting into finite supercells represents key question of the method, the sufficient size of the supercell is not known as well as the necessary number of trial configurations, one should always check whether the result converges when increasing supercell size and what is the error due to its variation.

An advantage of this method is its relatively simple implementation. Everything is performed here for one configuration so that no theory describing the effect of disorder must be employed. Therefore it can be used quite simply not only for one particle properties but also two-particle ones, which is one of the common areas of its application [15, 70]. It can also handle situations beyond the complete randomness assumption, i.e. short range order.

Unfortunately the supercell method has high computational demands. Concentrations of involved species are employed only by the ratio of atoms of their species with respect to total number of atoms in the supercell. In order to catch slight changes of concentrations very big supercell must be used, the demands may then grow to the maximum currently available computers can offer. On the other hand, the bigger the supercell, the less \mathbf{k} vectors must be used in calculation to maintain equal accuracy [70].

2.5.3 Coherent potential approximation

The *coherent potential approximation* (CPA) [71] is a single-site approximation - each site of the lattice is examined as a single impurity in an effective medium. The total Hamiltonian of the system can be rewritten as

$$H = [H_0 + \Sigma(z)] + [U - \Sigma(z)] , \quad (2.72)$$

where H_0 is the part of the Hamiltonian independent of configuration and U is its configuration-dependent complement. The CPA self-energy $\Sigma(z)$ (so far undefined) added to H_0 corresponds in CPA to the effective medium and it is associated to Green's function \bar{G} , overbars denote CPA averaged quantities. The remaining part of Hamiltonian $U - \Sigma(z)$ is now treated as a perturbation and the Dyson equation for the problem can be written:

$$G = \bar{G} + \bar{G}T\bar{G} . \quad (2.73)$$

It is immediately visible that if $\bar{G} = \langle G \rangle$, the Eq. (2.73) leads to the exact condition

$$\langle T \rangle = 0. \quad (2.74)$$

The CPA has been shown to be the best single-site approximation [72]. The T -matrix can be expanded as sums of site contributions $T = \sum_{\mathbf{R}} T_{\mathbf{R}}$, these contributions are expressed in terms of single impurity scattering matrix $t_{\mathbf{R}}$ [31]: $T_{\mathbf{R}} = t_{\mathbf{R}} + t_{\mathbf{R}} \bar{G} \sum_{\mathbf{R}'} T_{\mathbf{R}'}$, where the prime at the sum denotes exclusion of $\mathbf{R}' = \mathbf{R}$. Statistical correlations between $t_{\mathbf{R}}$ and $T_{\mathbf{R}'}$ are neglected, which is partially justified by the complete randomness of occupations, this is the so called CPA decoupling. Then a simple condition can be derived from Eq. (2.74) also for $t_{\mathbf{R}}$:

$$\langle t_{\mathbf{R}} \rangle = \sum_Q c^Q t_{\mathbf{R}}^Q(z) = 0. \quad (2.75)$$

The scattering matrix is required to behave so that scattering at a single site from the medium vanishes on average. This is the *Soven equation* [71] for CPA, which allows to find the CPA self-energy. The self-energy is also decomposed into site contributions: $\Sigma(z) = \Sigma_{\mathbf{R}}(z)$. Matrices $t_{\mathbf{R}}$ can be expressed in terms of these contributions:

$$t_{\mathbf{R}} = [U_{\mathbf{R}} - \Sigma_{\mathbf{R}}(z)] \{1 - \bar{G}(z) [U_{\mathbf{R}} - \Sigma_{\mathbf{R}}(z)]\}^{-1}. \quad (2.76)$$

Substituting (2.76) into (2.75) allows to find the unknown CPA self-energy $\Sigma(z)$. The exact condition (2.74) is then fulfilled with high accuracy, the only error is due to the CPA decoupling. This is the desired state, the CPA-averaged Green's function \bar{G} resembles closely the true configurational average of the system.

CPA can be conveniently combined with the TB-LMTO method [73]. This leads to an elegant formulation of the CPA-averaged auxiliary Green's function in the form of Eq. (2.24):

$$\bar{g}(z) = [\mathcal{P}(z) - S]^{-1}, \quad (2.77)$$

where $\mathcal{P}(z)$ is defined by this equation and is called a coherent potential function, LMTO representation indices are omitted. Due to the single-site character of the CPA it is site-diagonal: $\mathcal{P}_{\mathbf{R},\mathbf{R}'}(z) = \delta_{\mathbf{R},\mathbf{R}'} \mathcal{P}_{\mathbf{R}}(z)$. For an atom Q in the effective medium described by the coherent potential one can rewrite the formula (2.76) in terms of the coherent potential:

$$t_{\mathbf{R}}^Q(z) = \left(P_{\mathbf{R}}^Q(z) - \mathcal{P}_{\mathbf{R}}(z) \right) \left[1 + \bar{g}_{\mathbf{R},\mathbf{R}}(z) \left(P_{\mathbf{R}}^Q(z) - \mathcal{P}_{\mathbf{R}}(z) \right) \right]^{-1}. \quad (2.78)$$

For a binary alloy combining this equation with the CPA equation for t -matrices (2.75) leads to the following formula for the coherent potential function:

$$\mathcal{P}_{\mathbf{R}}(z) = \langle P_{\mathbf{R}}(z) \rangle + (P_{\mathbf{R}}^A(z) - \mathcal{P}_{\mathbf{R}}(z)) \bar{g}_{\mathbf{R},\mathbf{R}}(z) (P_{\mathbf{R}}^B(z) - \mathcal{P}_{\mathbf{R}}(z)). \quad (2.79)$$

A general solution for alloys with arbitrary number of components can be found in Chap. 10.7 of [34]. The coherent potential function is obtained in an iterative process which should lead to self-consistency. There are numerous particular schemes of this iterative process [34] and it is often combined with the DFT iteration scheme.

Chapter 3

CPP conductance in disordered metallic multilayers

The CPA is widely used to determine electronic structure of disordered systems. For two-particle observables, for example the conductance, there are additional obstacles to be solved, which are addressed in Sec. 3.1. The Kubo formula for conductance has been combined with the CPA a long time ago [74]. Its *ab initio* KKR implementation for residual resistivity of random bulk alloys [75] has been used by many authors [76–78]. However, for layered systems it has been applied only exceptionally, being confined mostly to models with a single orbital per site [79] or to a weak scattering limit [80]. In work [14] we have applied for the first time the coherent potential approximation to this problem on an *ab initio* level, which is the approach presented here. Its results are compared to supercell method results where possible, see sections 6.2.2, 6.3, 6.4.1.

3.1 CPA averages of two-particle observables, vertex corrections

In general, the Kubo formula (2.57) can be expressed so that it contains terms of the form $\text{Tr} \{G(z_\mu) B G(z_\nu) B'\}$. Current operators B, B' are nonrandom within the TB-LMTO method, thus configurational averages of the following form are to be found:

$$K(z_\mu, z_\nu) = \langle G(z_\mu) B G(z_\nu) \rangle . \quad (3.1)$$

Configurational average of a product of two Green's functions corresponds to a two-particle Green's function and it generally includes more complicated multiple-scattering processes than those included in the one particle Green function described in sec. 2.5. Since the operator B is nonrandom, after substituting the Dyson equation (2.73) into (3.1) and employing (2.74) one obtains :

$$\langle GBG \rangle = \bar{G} B \bar{G} + \bar{G} \Gamma \bar{G} , \quad (3.2)$$

where $\Gamma = \langle T \bar{G} B \bar{G} T \rangle$ and energy arguments are omitted for brevity. The simple contribution corresponding to one-particle diagrams given as $\bar{G} B \bar{G}$ will further be denoted as the

coherent part. Vertex corrections to it given by term $\bar{G}\Gamma\bar{G}$ represent genuine two-particle correlation effects [18]. This contribution to $\langle GBG \rangle$ in many cases cannot be neglected, as will be shown further.

Vertex corrections can be derived with the same assumptions as the CPA self-energy, namely the CPA decoupling. No diagrammatic expansion is involved here. Due to the localized nature of the single-site T-matrices $t_{\mathbf{R}}(z)$, Γ can be decomposed within the CPA into a sum of site-localized contributions:

$$\Gamma = \sum_{\mathbf{R}} \Gamma_{\mathbf{R}}. \quad (3.3)$$

A closed set of exactly soluble linear equations for unknown $\Gamma_{\mathbf{R}}$ has been derived [74]:

$$\begin{aligned} \Gamma_{\mathbf{R}}(z_{\mu}, z_{\nu}) &= \langle t_{\mathbf{R}}(z_{\mu}) \bar{G}(z_{\mu}) B \bar{G}(z_{\nu}) t_{\mathbf{R}}(z_{\nu}) \rangle + \\ &\sum_{\mathbf{R}'(\neq \mathbf{R})} \langle t_{\mathbf{R}}(z_{\mu}) \bar{G}(z_{\mu}) \Gamma_{\mathbf{R}'}(z_{\mu}, z_{\nu}) \bar{G}(z_{\nu}) t_{\mathbf{R}}(z_{\nu}) \rangle. \end{aligned} \quad (3.4)$$

Vertex corrections satisfy an important consistency condition, the Ward identity:

$$\Gamma(z_{\mu}, z_{\nu}, 1) = \frac{-1}{z_{\mu} - z_{\nu}} (\Sigma(z_{\mu}) - \Sigma(z_{\nu})), \quad (3.5)$$

where the third argument of Γ specifies the operator to which it corresponds. Satisfaction of this identity is natural since the derivation of vertex corrections is compatible with the self-energy.

3.2 LMTO full CPA solution for conductance

Vertex corrections have been shown to vanish for conductivities in a single band model [74]. However, this is not true for a multiband case. We express the abstract set of Eqs. (3.4) in the TB-LMTO basis (Sec. 2.2) and solve it.

The equation for $\Gamma_{\mathbf{R}}$ in terms of the matrix elements (energies omitted) :

$$\begin{aligned} \Gamma_{\mathbf{R}}^{L_1 L'_1} &= \sum_Q \sum_{L_2 L'_2} c_{\mathbf{R}}^Q t_{\mathbf{R}}^{Q L_1 L_2} [\bar{g} B \bar{g}]_{\mathbf{R} \mathbf{R}}^{L_2 L'_2} t_{\mathbf{R}}^{Q L'_2 L'_1} + \\ &\sum_Q \sum_{\mathbf{R}'(\neq \mathbf{R})} \sum_{L_2 L'_2 L_3 L'_3} c_{\mathbf{R}}^Q t_{\mathbf{R}}^{Q L_1 L_2} \bar{g}_{\mathbf{R} \mathbf{R}'}^{L_2 L_3} \Gamma_{\mathbf{R}'}^{L_3 L'_3} \bar{g}_{\mathbf{R}' \mathbf{R}}^{L'_3 L'_2} t_{\mathbf{R}}^{Q L'_2 L'_1}. \end{aligned} \quad (3.6)$$

They can be formally simplified by introducing the following composed indices and auxiliary variables:

$$\Lambda = (L, L'), \quad (3.7)$$

$$\xi_{\mathbf{R}}^{\Lambda_1}(z_{\mu}, z_{\nu}) = \xi_{\mathbf{R}}^{L_1 L'_1}(z_{\mu}, z_{\nu}) = (\bar{g}(z_{\mu}) B \bar{g}(z_{\nu}))_{\mathbf{R} \mathbf{R}}^{L_1 L'_1}, \quad (3.8)$$

$$\omega_{\mathbf{R}}^{\Lambda_1 \Lambda_2}(z_{\mu}, z_{\nu}) = \sum_Q c_{\mathbf{R}}^Q t_{\mathbf{R}}^{Q L_1 L_2}(z_{\mu}) t_{\mathbf{R}}^{Q L'_2 L'_1}(z_{\nu}), \quad (3.9)$$

$$\chi_{\mathbf{R}\mathbf{R}'}^{\Lambda_1\Lambda_2}(z_\mu, z_\nu) = (1 - \delta_{\mathbf{R}\mathbf{R}'}) \bar{g}_{\mathbf{R}\mathbf{R}'}^{L_1L_2}(z_\nu) \bar{g}_{\mathbf{R}'\mathbf{R}}^{L'_2L'_1}(z_\mu). \quad (3.10)$$

The original Eqs. (3.6) are then rewritten compactly as:

$$\Gamma_{\mathbf{R}}^{\Lambda_1} = \sum_{\Lambda_2} \omega_{\mathbf{R}}^{\Lambda_1\Lambda_2} \xi_{\mathbf{R}}^{\Lambda_2} + \sum_{R'; \Lambda_2\Lambda_3} \omega_{\mathbf{R}}^{\Lambda_1\Lambda_2} \chi_{\mathbf{R}\mathbf{R}'}^{\Lambda_2\Lambda_3} \Gamma_{\mathbf{R}'}^{\Lambda_3}, \quad (3.11)$$

where energy arguments have been omitted for brevity. Matrices with one \mathbf{R} index are treated here as if were multiplied by $\delta_{\mathbf{R}\mathbf{R}'}$. The set of equations (3.11) for Γ is solved by matrix inversion, which yields the following matrix equation:

$$\Gamma = (1 - \omega\chi)^{-1} \omega\xi = (\omega^{-1} - \chi)^{-1} \xi. \quad (3.12)$$

Auxiliary variables can be defined in a slightly different way, which leads to a solution more suitable for a direct calculation:

$$\lambda^{-1} = \omega^{-1} + \varphi, \quad (3.13)$$

where

$$\varphi_{\mathbf{R}}^{\Lambda_1\Lambda_2}(z_\mu, z_\nu) = \bar{g}_{\mathbf{R}\mathbf{R}}^{L_1L_2}(z_\mu) \bar{g}_{\mathbf{R}\mathbf{R}}^{L'_2L'_1}(z_\nu). \quad (3.14)$$

Then the matrix equation for vertex corrections reads:

$$\Gamma = (\lambda^{-1} - \psi)^{-1} \xi, \quad (3.15)$$

where $\psi_{\mathbf{R}_1\mathbf{R}_2}^{\Lambda_1\Lambda_2}(z_\mu, z_\nu) = \bar{g}_{\mathbf{R}_1\mathbf{R}_2}^{L_1L_2}(z_\mu) \bar{g}_{\mathbf{R}_2\mathbf{R}_1}^{L'_2L'_1}(z_\nu)$, hence it fulfills $\chi = \psi - \varphi$. The advantage is that λ is site-diagonal and ψ has a more simple structure than χ , which allow to perform lattice Fourier transformation easily. The central matrix is given its name:

$$\Delta = \lambda^{-1} - \psi. \quad (3.16)$$

The equation for vertex corrections with explicit typing of all indices reads:

$$\Gamma_{\mathbf{R}_1}^{\Lambda_1}(z_\mu, z_\nu) = (\Delta^{-1})_{\mathbf{R}_1\mathbf{R}_2}^{\Lambda_1\Lambda_2}(z_\mu, z_\nu) \xi_{\mathbf{R}_2}^{\Lambda_2}(z_\mu, z_\nu). \quad (3.17)$$

3.3 CPP conductance in disordered multilayers

With the knowledge of vertex corrections the conductance can be derived directly from the formula (2.68). As both operators $\mathcal{B}_{\mathcal{L}}$ and $\mathcal{B}_{\mathcal{R}}$ are nonrandom, one of them can be put out of the configurational average; the remaining part to be averaged corresponds to the product of two Green's functions and an operator, which already appeared in equation (3.1), the second one from operators $\mathcal{B}_{\mathcal{L},\mathcal{R}}$ is identified with the generic operator B . Hence (3.2) can be employed and the main term in conductance expression is also expanded into the coherent and VC part:

$$\begin{aligned} & \text{Tr} \langle g(z_\mu) \mathcal{B}_{\mathcal{L}} g(z_\nu) \mathcal{B}_{\mathcal{R}} \rangle = \\ & \text{Tr} \{ \bar{g}(z_\mu) \mathcal{B}_{\mathcal{L}} \bar{g}(z_\nu) \mathcal{B}_{\mathcal{R}} \} + \text{Tr} \{ \bar{g}(z_\mu) \Gamma \bar{g}(z_\nu) \mathcal{B}_{\mathcal{R}} \}. \end{aligned} \quad (3.18)$$

The coherent part is similar to the case without disorder, but now the auxiliary Green's function $g(z)$ is replaced by its configurationally averaged counterpart \bar{g} . The trace property for the VC part is employed:

$$C_{VC}(z_\mu, z_\nu) = \frac{1}{2\pi} \text{Tr} \{ \bar{g}(z_\mu) \Gamma \bar{g}(z_\nu) \mathcal{B}_R \} = \frac{1}{2\pi} \text{Tr} \{ \bar{g}(z_\nu) \mathcal{B}_R \bar{g}(z_\mu) \Gamma \} . \quad (3.19)$$

Substituting Γ from (3.17) leads to:

$$C_{VC}(z_\mu, z_\nu) = \frac{1}{2\pi} \sum_{\mathbf{R}_1 \Lambda_1} \sum_{\mathbf{R}_2 \Lambda_2} [\bar{g}(z_\nu) \mathcal{B}_R \bar{g}(z_\mu)]_{\mathbf{R}_1}^{\tilde{\Lambda}_1} [\Delta^{-1}(z_\mu, z_\nu)]_{\mathbf{R}_1 \mathbf{R}_2}^{\Lambda_1 \Lambda_2} [\bar{g}(z_\mu) \mathcal{B}_L \bar{g}(z_\nu)]_{\mathbf{R}_2}^{\Lambda_2} , \quad (3.20)$$

where the index $\tilde{\Lambda}$ means Λ with a transposed order of orbital indices and the quantity $\xi(z_\mu, z_\nu)$ is now labeled as $[\bar{g}(z_\mu) \mathcal{B}_{L,R} \bar{g}(z_\nu)]$ to make its close relation to operators \mathcal{B}_L , \mathcal{B}_R more transparent. The result is again explicitly symmetric in \mathcal{B}_L , \mathcal{B}_R , although vertex corrections were expressed with respect to only one of the operators during the derivation.

Multilayers can be viewed as systems with 2D translational invariance, there are always two dimensions much larger than electron mean free path and the corresponding boundaries does not play role, contrary to its thickness, which is on the nanoscale. In disordered systems, the 2D translational invariance is destroyed, but the effective system replacing the physical one is again translationally invariant. This is greatly facilitated in calculations of Green's functions, where the 2D lattice Fourier transformation from the real to reciprocal space is then employed (Sec. 2.2.3). Matrix quantities in real space transform according to Eq. (2.29), the opposite transformation is given by (2.30). Generally the site position vector \mathbf{R} is decomposed as $\mathbf{R} \equiv (p, \mathbf{B}, \mathbf{T}_\parallel)$ as described in Sec. 2.2.3. The quantities involved in Eq. (3.20) expressed in terms of \mathbf{k}_\parallel -resolved Green's functions:

$$\Delta(0, z_\mu, z_\nu)_{p_1, \mathbf{B}; p_2, \mathbf{B}_2}^{\Lambda_1 \Lambda_2} = \delta_{p_1 \mathbf{B}_1; p_2 \mathbf{B}_2} [\lambda^{-1}(z_\mu, z_\nu)]_{p_1 \mathbf{B}_1}^{\Lambda_1 \Lambda_2} - \frac{1}{N} \sum_{\mathbf{k}_\parallel} \bar{g}_{p_1 \mathbf{B}_1; p_2 \mathbf{B}_2}^{L_1 L_2}(\mathbf{k}_\parallel, z_\mu) \bar{g}_{p_2 \mathbf{B}_2; p_1 \mathbf{B}_1}^{L'_2 L'_1}(\mathbf{k}_\parallel, z_\nu) . \quad (3.21)$$

$$[\bar{g}(z_\mu) \mathcal{B}_R \bar{g}(z_\nu)]_{p \mathbf{B}}^\Lambda = \frac{1}{N} \sum_{\mathbf{k}_\parallel} \sum_{L_a \mathbf{B}_a} \sum_{L_b \mathbf{B}_b} \bar{g}_{p \mathbf{B}; p_R \mathbf{B}_a}^{L L_a}(\mathbf{k}_\parallel, z_\mu) \mathcal{B}_{R \mathbf{B}_a; \mathbf{B}_b}^{L_a L_b}(\mathbf{k}_\parallel) \bar{g}_{p_R \mathbf{B}_b; p \mathbf{B}}^{L_b L'}(\mathbf{k}_\parallel, z_\nu) \quad (3.22)$$

Note that they are independent of \mathbf{k}_\parallel as well as \mathbf{T}_\parallel , which significantly simplifies the calculation. The first expression is nothing but the lattice Fourier transform for zero \mathbf{k}_\parallel vector of the matrix $\Delta_{\mathbf{R}_1 \mathbf{R}_2}^{\Lambda_1 \Lambda_2}(z_\mu, z_\nu)$, Eq. (3.16). The formula for VC contribution to conductance is then given as [14]:

$$\text{Tr} \langle g(z_\mu) \mathcal{B}_L g(z_\nu) \mathcal{B}_R \rangle_{VC} = \frac{1}{2\pi} \sum_{p_1 \mathbf{B}_1 \Lambda_1} \sum_{p_2 \mathbf{B}_2 \Lambda_2} [\bar{g}(z_\nu) \mathcal{B}_R \bar{g}(z_\mu)]_{p_1, \mathbf{B}_1}^{\tilde{\Lambda}_1} [\Delta^{-1}(0, z_\mu, z_\nu)]_{p_1, \mathbf{B}_1; p_2, \mathbf{B}_2}^{\Lambda_1 \Lambda_2} [\bar{g}(z_\mu) \mathcal{B}_L \bar{g}(z_\nu)]_{p_2, \mathbf{B}_2}^{\Lambda_2} . \quad (3.23)$$

Equation (4.41) together with the definitions of auxiliary variables (Eqs. 3.21, 3.22, 3.13) represents the central result of this chapter and was implemented in an *ab initio* calculation

scheme. The matrix Δ to be inverted is of the size $l_{max}^4 \tilde{N}^2$, where $\tilde{N} = \sum_{p=1}^N \tilde{N}_p$ and \tilde{N}_p denotes the number of disordered basis atoms in one principal layer p . This can yield for example matrices of the order 1000×1000 for (Ga,Mn)As slab containing 12 principal layers, but the numerically demanding inversion of it has to be done for only one \mathbf{k}_{\parallel} point. The smaller basis with respect to the supercell method (Sec. 2.5.2) leads to a significant performance gain of the full CPA scheme, although all subblocks of $\bar{g}(\mathbf{k}_{\parallel}, z)$ must be evaluated here in contrast to the CPP conductance formula for a clean system (2.68) used also in supercell transport calculations, where only the layer-wise subblocks in corners $(1, N)$ and $(N, 1)$ are needed. As the evaluation of the whole $\bar{g}(\mathbf{k}_{\parallel}, z)$ is the most time-consuming part, it is advantageous to utilize the tridiagonal character of the Hamiltonian in space, this procedure then becomes roughly of order N^2 .

This CPA based method has been used to examine selected impure Co/Cu based multilayers (Chap. 6), thin layers of (Ga,Mn)As (Chap. 7) and possible disorder in Co₂MnSi (Chap. 8). In the first case results were compared to alternative supercell calculations and their overall agreement confirms the validity of this approach. The presented derivation can be also adapted to spin-mixing conductances, see Sec. 4.5.

3.3.1 Lattice point group symmetry

In addition to translation symmetry, lattice point group symmetry represents an important factor influencing the solid properties. If it is utilized in ES and transport calculations, it allows to evaluate general quantities X for \mathbf{k} -points only inside the irreducible Brillouin zone (IBZ), while the rest of the total Brillouin zone (BZ) can be obtained from appropriate similarity transformations $U(\mathcal{O})$ [34], where \mathcal{O} are symmetry operations. This rests on the existence of matrices M and M' such that X for vectors $\mathcal{O}\mathbf{k}$ outside the IBZ can be expressed as

$$X(\mathcal{O}\mathbf{k}) = M(\mathcal{O}) X(\mathbf{k}) M'(\mathcal{O}) . \quad (3.24)$$

This provides significant reduction of calculation time and memory requirements. Its implementation in CPA transport for disordered systems is not so straightforward as for systems without disorder, but in principle it can reduce the amount of \mathbf{k} -points to calculate by the same ratio, $1/|\mathcal{N}_{\mathcal{O}}|$, where $|\mathcal{N}_{\mathcal{O}}|$ is the order of the group of allowed symmetry operations. The argumentation is valid for any translational symmetry, hence only vectors from Brillouin zone will now be generally denoted as \mathbf{k} . Quantities averaged over the whole BZ (X^{BZ}) are expressed in the following way in terms of an IBZ-averaged quantities X^{IBZ} :

$$X^{\text{BZ}} = \frac{1}{|\mathcal{N}_{\mathcal{O}}|} \sum_{\mathcal{O}} X^{\text{IBZ}}(\mathcal{O}) . \quad (3.25)$$

Let us first examine the behavior of TB-LMTO Green's functions: elements diagonal in \mathbf{B} transform as

$$g_{\mathbf{B},\mathbf{B}}(\mathcal{O}\mathbf{k}) = U^+(\mathcal{O}) g_{\mathbf{B},\mathbf{B}}(\mathbf{k}) U(\mathcal{O}) , \quad (3.26)$$

which is already in the form of Eq. (3.24). Explicit matrix structure of similarity transformations is U^{L_1, L_2} , summations over these orbital indices L are omitted for brevity. For transformation of elements non-diagonal in \mathbf{B} an additional factor (unitary matrix in orbital indices)

$$f_{\mathbf{B}}(\mathcal{O}, \mathbf{k}) = e^{i\mathbf{k}(\mathcal{O}^{-1}\mathbf{B}-\mathbf{B})} \quad (3.27)$$

is present:

$$g_{\mathbf{B},\mathbf{B}'}(\mathcal{O}\mathbf{k}) = f_{\mathbf{B}}(\mathcal{O},\mathbf{k}) U^+(\mathcal{O}) g_{\mathbf{B},\mathbf{B}'}(\mathbf{k}) U(\mathcal{O}) f_{\mathbf{B}'}^{-1}(\mathcal{O},\mathbf{k}). \quad (3.28)$$

BZ summations in Eqs. (3.21, 3.22) allows to utilize these properties of Green's functions. Value of Eq. (3.22) for a part of BZ obtained by a symmetry operation \mathcal{O} is given (with omitted explicit dependence of $U(\mathcal{O})$ and $f_{\mathbf{B}}(\mathcal{O},\mathbf{k})$ on \mathcal{O}) as:

$$\begin{aligned} [\bar{g}(z_\mu) \mathcal{B} \bar{g}(z_\nu)]_{p\mathbf{B}}(\mathcal{O}) &= \frac{1}{N} \sum_{\mathbf{k}(\text{IBZ})} \sum_{\mathbf{B}_a} \sum_{\mathbf{B}_b} f_{\mathbf{B}}(\mathbf{k}) U^+ \bar{g}_{p\mathbf{B},p\mathbf{R}\mathbf{B}_a}(\mathbf{k},z_\mu) U f_{\mathbf{B}_a}^{-1}(\mathbf{k}) f_{\mathbf{B}_a}(\mathbf{k}) U^+ \\ &\quad \times \mathcal{B}_{\mathbf{B}_a\mathbf{B}_b}(\mathbf{k}) U f_{\mathbf{B}_b}^{-1}(\mathbf{k}) f_{\mathbf{B}_b}(\mathbf{k}) U^+ \bar{g}_{p\mathbf{R}\mathbf{B}_b,p\mathbf{B}}(\mathbf{k},z_\nu) U f_{\mathbf{B}}^{-1}(\mathbf{k}). \end{aligned}$$

All adjacent UU^+ terms cancel, all $f_{\mathbf{B}}(\mathbf{k})$ terms cancel with their counterpart $f_{\mathbf{B}}^{-1}(\mathbf{k})$. Then

$$[\bar{g}(z_\mu) \mathcal{B} \bar{g}(z_\nu)](\mathcal{O}) = U^+(\mathcal{O}) [\bar{g}(z_\mu) \mathcal{B} \bar{g}(z_\nu)]^{\text{IBZ}} U(\mathcal{O}), \quad (3.29)$$

where $[\bar{g}(z_\mu) \mathcal{B} \bar{g}(z_\nu)]^{\text{IBZ}}$ is given by Eq. (3.22), but with the \mathbf{k} -summation restricted only to the irreducible Brillouin zone. This result has the form of Eq. (3.24), it is valid for each \mathbf{k} point from IBZ as well as the whole IBZ average.

For $\psi(z_\mu, z_\nu)$, the only \mathbf{k} -dependent component of $\Delta(0, z_\mu, z_\nu)$ (Eq. 3.21), we first examine the effect of the inclusion of $f_{\mathbf{B}}(\mathbf{k})$ and for clarity omit U , which commutes with $f_{\mathbf{B}}(\mathbf{k})$:

$$\tilde{\psi}_{p_1\mathbf{B}_1;p_2\mathbf{B}_2}^{L_1L'_1;L_2L'_2}(\mathcal{O}, z_\mu, z_\nu) = \sum_{\mathbf{k}(\text{IBZ})} f_{\mathbf{B}_1}^{-1}(\mathbf{k}) \bar{g}_{p_1\mathbf{B}_1,p_2\mathbf{B}_2}^{L_1;L_2}(\mathbf{k}, z_\mu) f_{\mathbf{B}_2}^{-1}(\mathbf{k}) f_{\mathbf{B}_2}(\mathbf{k}) \bar{g}_{p_2\mathbf{B}_2,p_1\mathbf{B}_1}^{L'_2;L'_1}(\mathbf{k}, z_\nu) f_{\mathbf{B}_1}^{-1}(\mathbf{k}). \quad (3.30)$$

All $f_{\mathbf{B}}(\mathbf{k})$ terms cancel here. The true $\psi(z_\mu, z_\nu)$ for the part of BZ corresponding to symmetry operation \mathcal{O} is given as:

$$\begin{aligned} \psi_{p_1\mathbf{B}_1,p_2\mathbf{B}_2}^{\tilde{L}_1\tilde{L}'_1;\tilde{L}_2\tilde{L}'_2}(\mathcal{O}, z_\mu, z_\nu) &= \\ &= \sum_{L_1L_2L'_1L'_2} \sum_{\mathbf{k}(\text{IBZ})} (U^+)^{\tilde{L}_1L_1} (U^+)^{\tilde{L}'_1L'_1} \bar{g}_{p_1\mathbf{B}_1,p_2\mathbf{B}_2}^{L_1L_2}(\mathbf{k}, z_\mu) \bar{g}_{p_2\mathbf{B}_2,p_1\mathbf{B}_1}^{L'_1L'_2}(\mathbf{k}, z_\nu) U^{L_2\tilde{L}_2} U^{L'_2\tilde{L}'_2} \\ &= \sum_{L_1L_2L'_1L'_2} (U^+)^{\tilde{L}_1L_1} (U^+)^{\tilde{L}'_1L'_1} \psi_{p_1\mathbf{B}_1,p_2\mathbf{B}_2}^{\text{IBZ } L_1L'_1;L_2L'_2}(z_\mu, z_\nu) U^{L_2\tilde{L}_2} U^{L'_2\tilde{L}'_2}, \end{aligned} \quad (3.31)$$

where $\psi^{\text{IBZ}}(z_\mu, z_\nu)$ is given by Eq. (3.21), but with the \mathbf{k} -summation restricted only to the irreducible Brillouin zone. The transformation $\mathbf{k} \rightarrow \mathcal{O}\mathbf{k}$ is now performed by a proper multiplication of submatrices of ψ by U matrices, it cannot be expressed in terms of compound indices Λ , but it is still in the form of (3.24) suitable for the replacement of BZ averaging by IBZ one.

Chapter 4

Spin torques due to spin accumulation

If a current incident on a thin ferromagnetic (FM) layer is polarized non-collinear with respect to the layer magnetization direction, it exerts a *spin-transfer torque* on the magnetic layer and may change its magnetization direction [9]. This phenomenon is therefore referred to as the current induced magnetization switching (CIMS).

One of successful quantitative descriptions of this process is based on Valet-Fert model (Sec. 2.3), which has been recently extended to non-collinear spin structures [81–83]. It rests heavily on two additional properties of spin currents (Sec. 5.1). First, the transverse (perpendicular to local exchange field) component of the spin current inside a ferromagnet becomes rapidly damped on a typical distance of a few interatomic spacings [84]. This very short magnetic coherence length is a result of a large exchange splitting which leads to mostly destructive interference effects due to all contributions of wave vectors on the two Fermi surfaces of the ferromagnetic metal. Consequently, the *spin torque* experienced by a ferromagnetic (FM) layer can be identified with the transverse spin current at its interface with a neighboring non-magnetic (NM) layer. Second, the proper boundary conditions inevitable for a full solution of the diffusion equations must be formulated in terms of properties of individual interfaces and it comes out that more information is needed than contained in the spin-resolved conductances of the interfaces.

The magneto-electronic circuit theory [15, 85, 86] represents another flexible approach to the transport properties of non-collinear magnetic systems consisting of FM and NM elements (nodes). This scheme is highly efficient especially when dimensions of individual nodes are smaller than the spin-diffusion lengths but bigger than the electron mean-free paths of the corresponding materials. The theory is based on the semiclassical concept of spin accumulation (Sec. 4.1). Within the developed formalism, the chemical potentials and spin accumulations of the nodes are contained in 2×2 distribution matrices in the spin space. The change of spin current due to junctions among the nodes is related to the non-collinear part of spin accumulation in terms of the so called spin-mixing conductance. The steady-state currents, spin currents and spin torques in a device can be obtained from applied voltages by solving a set of linear equations quite similar to the Kirchhoff's laws for usual electronic circuits, see Ref. [15] for a review.

A truly microscopic (quantum mechanical) approach to all aspects of CIMS seems to

be prohibitively complicated having in mind the large layer thicknesses and the quality of interfaces in presently used multilayers and spin valves. A reasonable compromise between the accuracy and the complexity has been adopted by several authors in addressing the spin-polarized electronic and transport properties of a single ferromagnet/non-magnet interface [84, 87] with emphasis put on the conductances and their sensitivity, e.g., to interface alloying. Since the traditional scheme for the transport, namely the Landauer-Büttiker scattering theory [19, 58, 59], has been used in majority of papers, the effect of disorder was included by a supercell technique [15, 88].

Here we sketch an alternative approach to the mixing conductances that employs the non-equilibrium Green's function (NEGF) formalism [19] applied to a ferromagnetic (FM) layer embedded between two semi-infinite non-magnetic (NM) leads; in one of them the spin accumulation is present. The derived general formula is implemented in an *ab initio* technique. The spin-mixing conductances of FM layers of a finite thickness attached to two NM leads have been studied very recently for Co/Cu, Fe/Au and Fe/Cr systems [89]. We calculate these properties for two of these systems too, so that both methods can be compared, and also provide novel results for systems where the spin-mixing conductance may have extraordinary properties, namely (Ga,Mn)As (Chap. 7) and Co₂MnSi (Chap. 8).

4.1 Spin accumulation and spin torques

Conductance electrons passing transversally through a FM1 | NM | FM2 junction experience spin-dependent reflections at interfaces which leads to spin-polarization of electrons even in NM layer (if NM layer thickness is smaller than the spin-diffusion length). This can be represented by spin-dependent chemical potential in the NM layer, which corresponds to the so called spin accumulation. The spin accumulation is assumed to be uniform across NM layer and it can be described by its direction \mathbf{s} and size. The *spin-transfer torque* can then be related directly to this spin accumulation, and a model with only one FM layer (Fig. 4.1) is sufficient to describe this problem. We examine the linear response of the *spin torque* to the spin accumulation, thus only infinitesimal spin accumulation is taken into account, see Fig. 4.2.

The Hamiltonian H is limited to the so called intermediate region and semi-infinite NM leads are included in the system Hamiltonian as a self-energy (Sec. 2.2.3), see Fig. 4.1. The Hamiltonian is given as

$$\hat{H} = H_0 + \gamma(\boldsymbol{\sigma} \cdot \mathbf{n}), \quad (4.1)$$

where H_0 represents a spin-independent part, $\boldsymbol{\sigma} = (\hat{\sigma}_x, \hat{\sigma}_y, \hat{\sigma}_z)$ is the vector of Pauli matrices, \mathbf{n} defines the direction of the exchange field of the FM layer and γ its corresponding exchange splitting (nonzero only inside the FM layer). Matrices in spin space are denoted by hat ($\hat{\cdot}$).

For the purpose of magnetization switching we define the *spin torque* as a time derivative of the total spin moment and obtain this quantity of interest directly using its operator defined as:

$$\boldsymbol{\tau} = -i \left[\boldsymbol{\sigma}, \hat{H} \right]. \quad (4.2)$$

This approach is formally different, but physically equivalent to existing approaches based on evaluation of difference between spin currents on both sides of the FM layer [15], see

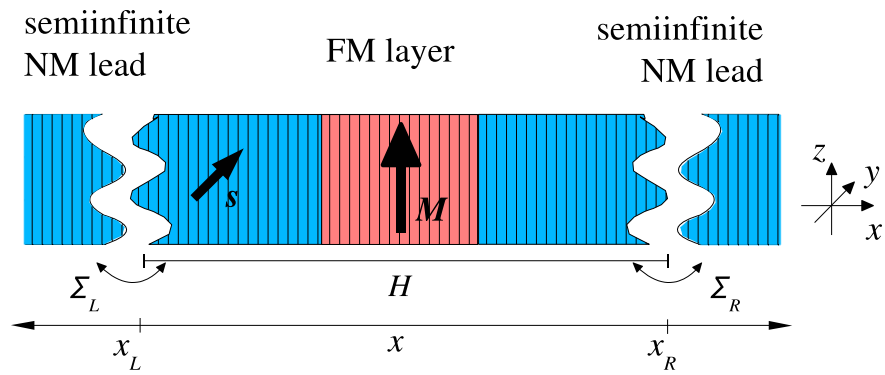


Figure 4.1: NM | FM | NM junction with spin accumulation \mathbf{s} parallel to the y -axis in the left lead.

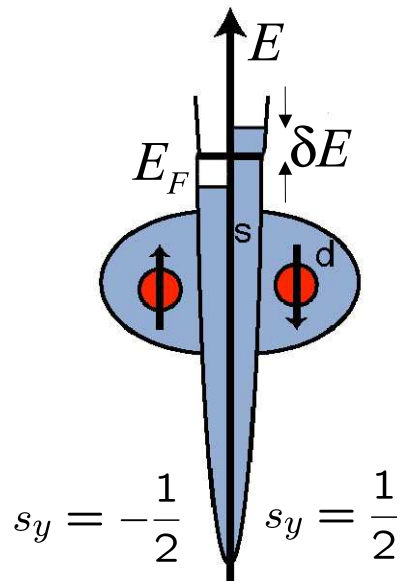


Figure 4.2: Infinitesimally small spin accumulation parallel to the y -axis direction

Sec. 5.1.

The well known algebraic rules for the Pauli matrices

$$\begin{aligned}(\boldsymbol{\sigma} \cdot \mathbf{p})(\boldsymbol{\sigma} \cdot \mathbf{q}) &= \mathbf{p} \cdot \mathbf{q} + i(\mathbf{p} \times \mathbf{q}) \cdot \boldsymbol{\sigma}, \\ (\boldsymbol{\sigma} \cdot \mathbf{p})\boldsymbol{\sigma} &= \mathbf{p} + i\boldsymbol{\sigma} \times \mathbf{p}, \\ \boldsymbol{\sigma}(\boldsymbol{\sigma} \cdot \mathbf{q}) &= \mathbf{q} + i\mathbf{q} \times \boldsymbol{\sigma},\end{aligned}\tag{4.3}$$

valid for arbitrary classical vectors \mathbf{p} and \mathbf{q} , yield an explicit form of the torque operator

$$\boldsymbol{\tau} = 2\gamma\mathbf{n} \times \boldsymbol{\sigma}.\tag{4.4}$$

This relation shows that the spin torque is a local operator non-zero only inside the intermediate region. *Ab initio* expression for the response $\mathbf{C}_{\mathcal{L}}$ of the spin torque to the spin accumulation can be found using NEGF. An alternative approach based on the Kubo linear response theory is also possible, we use it to derive a less general formula only for spin torque response in the direction parallel to the spin accumulation. NEGF based derivation for this component of the total spin torque will be published elsewhere [90].

4.2 Derivation based on NEGF

The thermodynamic average of the spin torque $\boldsymbol{\tau}$ for the NM|FM|NM system in a stationary non-equilibrium state is given by

$$\bar{\boldsymbol{\tau}} = \frac{1}{2\pi} \int_{-\infty}^{\infty} \text{Tr} \{ \boldsymbol{\tau} G^<(E) \} dE,\tag{4.5}$$

where $G^<(E)$ is the lesser component of the non-equilibrium Green's function. The latter quantity is related to the retarded and advanced Green's functions $G^r(E)$ and $G^a(E)$ by means of the kinetic equation

$$\begin{aligned}G^<(E) &= G^r(E)\Sigma^<(E)G^a(E), \\ G^r(E) &= [E - H - \Sigma^r(E)]^{-1}, \\ G^a(E) &= [E - H - \Sigma^a(E)]^{-1},\end{aligned}\tag{4.6}$$

where $\Sigma^<(E)$, $\Sigma^r(E)$ and $\Sigma^a(E)$ denote the lesser, retarded and advanced components of the self-energy, respectively, which are usually defined in NEGF formalism [19]. The total self-energies are given as sums of separate contributions due to the left (\mathcal{L}) and the right (\mathcal{R}) leads,

$$\Sigma^x(E) = \Sigma_{\mathcal{L}}^x(E) + \Sigma_{\mathcal{R}}^x(E), \quad x = r, a, <.\tag{4.7}$$

These self-energies therefore correspond to embedding potentials (2.36) once the TB-LMTO formulation is assumed (Sec. 4.5). Note that all operators in Eqs. (4.5, 4.6) are defined in the Hilbert space of the intermediate region.

The spin accumulation in the NM leads results in a change of the lesser self-energy $\delta\Sigma^<(E)$ (see below), which induces the following first-order change of the thermodynamic average (4.5):

$$\delta\bar{\boldsymbol{\tau}} = \frac{1}{2\pi} \int_{-\infty}^{\infty} \text{Tr} \{ G^a(E)\boldsymbol{\tau}G^r(E)\delta\Sigma^<(E) \} dE.\tag{4.8}$$

The special form of the torque operator, Eq. (4.2), together with the expression for $G^{r,a}(E)$, Eq. (4.6), provide a relation

$$G^a(E)\boldsymbol{\tau}G^r(E) = -i[\boldsymbol{\sigma}G^r(E) - G^a(E)\boldsymbol{\sigma}] + G^a(E)\boldsymbol{\sigma}\mathcal{B}(E)G^r(E), \quad (4.9)$$

where the abbreviation for the antihermitean part of self-energy due to leads according to Eq. (2.61, 2.62) is employed.

In deriving Eq. (4.9), use was made of the fact that the self-energies of the unperturbed NM leads are spin-independent, so that $[\boldsymbol{\sigma}, \Sigma^{r,a}(E)] = 0$.

For stationary non-equilibrium systems without spin accumulation, the lesser self-energies are given by

$$\Sigma_{\mathcal{L},\mathcal{R}}^<(E) = f_{\mathcal{L},\mathcal{R}}(E)\mathcal{B}_{\mathcal{L},\mathcal{R}}(E), \quad (4.10)$$

where the functions $f_{\mathcal{L},\mathcal{R}}(E)$ refer to the Fermi-Dirac distributions of the two leads.

In the thermodynamic equilibrium, the distributions $f_{\mathcal{L},\mathcal{R}}(E)$ coincide with the Fermi-Dirac distribution of the whole system. In presence of the spin accumulation in one of the leads (\mathcal{L}), the system is driven out of equilibrium by adding a spin-dependent shift $\delta E_{\mathcal{L}}$ to the Fermi energy of the lead. This yields the first-order change of the lesser self-energy in a form

$$\delta\Sigma^<(E) = \delta\Sigma_{\mathcal{L}}^<(E) = f'(E)(\boldsymbol{\sigma} \cdot \mathbf{s})\mathcal{B}_{\mathcal{L}}(E)\delta E_{\mathcal{L}}, \quad (4.11)$$

where $f'(E)$ means the derivative of the Fermi-Dirac distribution and \mathbf{s} is a unit vector pointing in direction of the spin accumulation. For systems at zero temperature, which will be considered in the following, $f'(E) = -\delta(E - E_F)$ where E_F is the Fermi energy. Substitution of Eqs. (4.9, 4.11) into Eq. (4.8) provides a starting expression for the corresponding response coefficient $\mathbf{C}_{\mathcal{L}}$:

$$\mathbf{C}_{\mathcal{L}} \equiv \frac{\delta\bar{\boldsymbol{\tau}}}{\delta E_{\mathcal{L}}} = \frac{1}{2\pi} \text{Tr} [i(\boldsymbol{\sigma}G^r - G^a\boldsymbol{\sigma})(\boldsymbol{\sigma} \cdot \mathbf{s})\mathcal{B}_{\mathcal{L}} - \boldsymbol{\sigma}\mathcal{B}G^r(\boldsymbol{\sigma} \cdot \mathbf{s})\mathcal{B}_{\mathcal{L}}G^a], \quad (4.12)$$

where all omitted energy arguments equal the Fermi energy E_F .

In order to extract the dependence of the response coefficient $\mathbf{C}_{\mathcal{L}}$ on orientation of the spin accumulation \mathbf{s} and the magnetization direction \mathbf{n} , the explicit structure of the Green's functions $G^{r,a}$ of the Hamiltonian (4.1) with respect to the spin must be used,

$$G^{r,a} = \frac{G_{\uparrow}^{r,a} + G_{\downarrow}^{r,a}}{2} + \frac{G_{\uparrow}^{r,a} - G_{\downarrow}^{r,a}}{2}(\boldsymbol{\sigma} \cdot \mathbf{n}), \quad (4.13)$$

where the spin-resolved Green's functions are defined by

$$G_s^{r,a}(E) = [E - H_s - \Sigma^{r,a}(E)]^{-1}, \quad s = \uparrow, \downarrow. \quad (4.14)$$

The substitution of Eq. (4.13) into Eq. (4.12) reduces its r.h.s. to a sum of terms of the form $\text{Tr}(\xi X) = \text{tr}_{\mathbb{S}}(\xi)\text{tr}(X)$ where ξ is a matrix in the spin indices only while X is a matrix in the other (site and orbital) indices and where the symbols $\text{tr}_{\mathbb{S}}$ and tr denote the respective trace operations. Further steps employ the rules (4.3) and their consequences for trace relations:

$$\begin{aligned} \text{tr}_{\mathbb{S}}[\boldsymbol{\sigma}(\boldsymbol{\sigma} \cdot \mathbf{s})] &= 2\mathbf{s}, \\ \text{tr}_{\mathbb{S}}[\boldsymbol{\sigma}(\boldsymbol{\sigma} \cdot \mathbf{n})(\boldsymbol{\sigma} \cdot \mathbf{s})] &= 2i\mathbf{n} \times \mathbf{s}, \\ \text{tr}_{\mathbb{S}}[\boldsymbol{\sigma}(\boldsymbol{\sigma} \cdot \mathbf{n})(\boldsymbol{\sigma} \cdot \mathbf{s})(\boldsymbol{\sigma} \cdot \mathbf{n})] &= 4(\mathbf{n} \cdot \mathbf{s})\mathbf{n} - 2\mathbf{s}. \end{aligned} \quad (4.15)$$

The resulting expression for $\mathbf{C}_{\mathcal{L}}$ follows after a lengthy but straightforward manipulation:

$$\mathbf{C}_{\mathcal{L}} = D_1 \mathbf{s} + D_2 \mathbf{s} \times \mathbf{n} - D_3 (\mathbf{n} \cdot \mathbf{s}) \mathbf{n}, \quad (4.16)$$

where the prefactors D_1 , D_2 and D_3 are given by

$$\begin{aligned} D_1 &= \frac{1}{2\pi} \text{tr} [i (G_{\uparrow}^r + G_{\downarrow}^r - G_{\uparrow}^a - G_{\downarrow}^a) \mathcal{B}_{\mathcal{L}} - \mathcal{B} G_{\uparrow}^r \mathcal{B}_{\mathcal{L}} G_{\downarrow}^a - \mathcal{B} G_{\downarrow}^r \mathcal{B}_{\mathcal{L}} G_{\uparrow}^a], \\ D_2 &= \frac{1}{2\pi} \text{tr} [(G_{\uparrow}^r - G_{\downarrow}^r + G_{\uparrow}^a - G_{\downarrow}^a) \mathcal{B}_{\mathcal{L}} + i (\mathcal{B} G_{\uparrow}^r \mathcal{B}_{\mathcal{L}} G_{\downarrow}^a - \mathcal{B} G_{\downarrow}^r \mathcal{B}_{\mathcal{L}} G_{\uparrow}^a)], \\ D_3 &= \frac{1}{2\pi} \text{tr} [\mathcal{B} (G_{\uparrow}^r - G_{\downarrow}^r) \mathcal{B}_{\mathcal{L}} (G_{\uparrow}^a - G_{\downarrow}^a)]. \end{aligned} \quad (4.17)$$

The form of Eq. (4.16) can be simplified by using a general relation

$$i [G^r(E) - G^a(E)] = G^a(E) \mathcal{B}(E) G^r(E) \quad (4.18)$$

that follows from Eqs. (4.6, 2.62). After inserting the spin-resolved counterparts of Eq. (4.18), $i(G_s^r - G_s^a) = G_s^a \mathcal{B} G_s^r$ ($s = \uparrow, \downarrow$), in the expression (4.17) for D_1 one obtains $D_3 = D_1$. The previous formula (4.16) for the response coefficient $\mathbf{C}_{\mathcal{L}}$ can thus be rewritten as

$$\mathbf{C}_{\mathcal{L}} = D_1 \mathbf{n} \times (\mathbf{s} \times \mathbf{n}) + D_2 \mathbf{s} \times \mathbf{n}. \quad (4.19)$$

Note that this results has a general form of a vector perpendicular to \mathbf{n} , in agreement with Eq. (4.4). A closer inspection of the real quantities D_1 and D_2 , Eq. (4.17), reveals their simple relation to a single complex quantity – the spin-mixing conductance $C_{\mathcal{L}}^{\text{mix}}$:

$$C_{\mathcal{L}}^{\text{mix}} = \frac{1}{2\pi} \text{tr} [i (G_{\uparrow}^r - G_{\downarrow}^a) \mathcal{B}_{\mathcal{L}} - \mathcal{B} G_{\uparrow}^r \mathcal{B}_{\mathcal{L}} G_{\downarrow}^a], \quad (4.20)$$

which yields

$$D_1 = D_3 = 2 \text{Re } C_{\mathcal{L}}^{\text{mix}}, \quad D_2 = 2 \text{Im } C_{\mathcal{L}}^{\text{mix}}. \quad (4.21)$$

The formulas (4.19, 4.20, 4.21) represent the central result of this Chapter. It is interesting to compare them to the well-known spin-resolved charge conductances, Eq. (2.69). We have shown that these formulas are invariant with respect to the position of boundaries between the leads and the intermediate region (Appendix B), which is an important feature for the consistency of the theory and for practical calculations.

4.3 Derivation based on the Kubo theory

The real part of the spin mixing conductance C^{mix} can also be derived within the Kubo linear response approach and the result is equivalent to that from the NEGF derivation. The Hamiltonian is in the form of Eq. (4.1), but we set the magnetization direction along the z -axis for simplicity:

$$\hat{H} = H_0 + \gamma \hat{\sigma}_z, \quad (4.22)$$

The setup of the system can be seen in Fig. 4.1. We employ the linear response theory (Sec. 2.4). The spin-transfer torque $\hat{\tau}_{\alpha} = -i[\hat{\sigma}_{\alpha}, \hat{H}]$ is substituted as an operator in the form $A = -i[B, H]$, and the perturbation operator is given as $\tilde{B} = \hat{\sigma}_y \phi(x)$, where $\phi(x)$

is the profile of the spin accumulation across layers and the spin accumulation is assumed to be parallel to the y -axis. Response coefficient $C_{A\tilde{B}}$ is in general given by three terms $C^{(1)}$, $C^{(2)}$, $C^{(3)}$ (Eq. 2.51). If we consider only the most interesting situation, the spin torque in the direction of the spin accumulation, $\hat{B} = \hat{\sigma}_y$, the spin-transfer torque operator is then

$$\hat{A} = -i \left[\hat{\sigma}_y, \hat{H} \right] = -i \left[\hat{\sigma}_y, H_0 + \gamma \hat{\sigma}_z \right] = 2\gamma \hat{\sigma}_x. \quad (4.23)$$

The operator \tilde{A} is evaluated as follows:

$$\tilde{A}(x) = -i \left[\tilde{B}(x), \hat{H} \right] = -i \left[\phi(x), H_0 \right] \hat{\sigma}_y + 2\phi(x) \gamma \hat{\sigma}_x. \quad (4.24)$$

Then the terms $C^{(2)}$ and $C^{(3)}$ vanish. Differently speaking this combination of A , \tilde{B} operators satisfies the condition (2.54). The presence of $C^{(3)}$ would require an integration over the whole energy range below Fermi level even at zero temperature, which would complicate the solution. This term cannot be shown to vanish in the calculation of an out-of-plane response in the direction given by $\hat{\sigma}_x$, therefore we examine only the first case here. Then only the term $C^{(1)}$ constitutes the linear response coefficient denoted C_K^{mix} , analogously to the charge conductance solution and for zero temperature it is given by substituting into (2.43):

$$C_K^{mix} = \pi \int d\xi f'(\xi) \text{Tr} \{ 2\gamma \hat{\sigma}_x \delta(\xi - H) (-i [\phi, H_0] \hat{\sigma}_y + 2\phi \gamma \hat{\sigma}_x) \delta(\xi - H) \}. \quad (4.25)$$

Employing explicit spin structure of Green's functions of collinear system (described in the preceding section) and the zero temperature assumption we find after a few manipulations:

$$C_K^{mix} = -\frac{2}{\pi} \text{tr} \{ 2\gamma \text{Im} G_{\downarrow}^r ([\phi, H_0] + 2\phi \gamma) \text{Im} G_{\uparrow}^r \} \quad (4.26)$$

Both γ and $[\phi, H_0] + 2\phi \gamma$ are localized to the intermediate region, hence the trace is evaluated only in that region. One can quickly find that for the Green's functions defined as the resolvent of the Hamiltonian (4.22) the following relations hold:

$$G_{\uparrow}^r 2\gamma G_{\downarrow}^r = G_{\uparrow}^r - G_{\downarrow}^r, \quad (4.27)$$

$$G_{\downarrow}^a 2\gamma G_{\uparrow}^a = G_{\uparrow}^a - G_{\downarrow}^a. \quad (4.28)$$

Employing the relation between $\text{Im} G_s^r$ and self-energies, Eq. (2.60) and the definition of its anti-hermitean part (2.61), formula (4.26) can then be rewritten as

$$C_K^{mix} = \frac{1}{2\pi} \text{tr} \{ G_{\uparrow}^r \mathcal{B} \phi G_{\uparrow}^a \mathcal{B} - G_{\uparrow}^r \mathcal{B} G_{\downarrow}^a \phi \mathcal{B} - G_{\downarrow}^r \mathcal{B} \phi G_{\uparrow}^a \mathcal{B} + G_{\downarrow}^r \mathcal{B} G_{\downarrow}^a \phi \mathcal{B} \}. \quad (4.29)$$

Operators \mathcal{B} are non-zero only at boundaries (interfaces to leads), therefore the response depends only on spin accumulation $\phi(x)$ at these boundaries, its arbitrary variations in the intermediate region are not significant. Consistently with Sec. 4.2 we express the response to the spin accumulation in the left lead (\mathcal{L}), hence $\lim_{x \rightarrow \infty} \phi(x) = \phi_{\mathcal{R}} = 0$ and the profile is then normalized so that $\lim_{x \rightarrow -\infty} \phi(x) = \phi_{\mathcal{L}} = 1$. This yields

$$C_{K,\mathcal{L}}^{mix} = \frac{1}{2\pi} \text{tr} \{ (G_{\uparrow}^r - G_{\downarrow}^r) \mathcal{B}_{\mathcal{L}} G_{\uparrow}^a \mathcal{B} - (G_{\uparrow}^r - G_{\downarrow}^r) \mathcal{B} G_{\downarrow}^a \mathcal{B}_{\mathcal{L}} \}. \quad (4.30)$$

Note that during BZ averaging this quantity for each \mathbf{k}_{\parallel} vector is summed together with its time inversion corresponding to its appropriate $-\mathbf{k}_{\parallel}$ vector and this inversion is related by symmetry operations to its origin: $G(-\mathbf{k}_{\parallel}) = G^T(\mathbf{k}_{\parallel})$. Using these operations one can show that the NEGF result in the linear response limit for the real part of the spin-mixing conductance (quantity D_3 in Eq. 4.17) is equivalent to that of the Kubo based approach (Eq. 4.30) if their sums together with their time-inversions are considered: $\sum_{\mathbf{k}_{\parallel}} C_{K,\mathcal{L}}^{mix}(\mathbf{k}_{\parallel}) = \sum_{\mathbf{k}_{\parallel}} 2\text{Re} C_{\mathcal{L}}^{mix}(\mathbf{k}_{\parallel})$. It has been also proved that an actual shape of spin accumulation profile in the system is irrelevant for the real part of the spin-mixing conductance, it depends only on its values at interfaces to leads. In NEGF derivation we assumed spin accumulation to be present only in the leads and now this assumptions was shown to be appropriate.

4.4 Comparison to scattering theory

The resulting dependence of the spin torque, Eq. (4.19) on the orientation of the spin accumulation and the magnetization is identical to that obtained within the Landauer-Büttiker scattering theory of transport [15]. In order to make the relation of this traditional tool to the present approach more explicit, we consider here the simplest case, namely a one-dimensional system with one propagating mode in both of the identical NM leads.

The configuration space of the system is a real axis with positions denoted by a continuous variable x ($-\infty < x < \infty$), see Fig. 4.1. The spin-independent part of the Hamiltonian is given by $H_0 = -(\partial/\partial x)^2$ (atomic units are used) and the exchange splitting $\gamma(x)$ vanishes for $x \leq x_{\mathcal{L}}$ and $x \geq x_{\mathcal{R}}$, where the points $x_{\mathcal{L}}$ and $x_{\mathcal{R}}$ denote the boundaries between the NM leads and the intermediate region containing the FM part. The Fermi energy corresponds to a positive kinetic energy in the leads, $E_F = k^2$ with $k > 0$.

The spin-resolved retarded and advanced Green's functions $G_s^{r,a}$ ($s = \uparrow, \downarrow$) at this real energy are constructed from two independent solutions $\chi_{1s}(x)$ and $\chi_{2s}(x)$ of the Schrödinger equation for the Hamiltonians $H_{\uparrow} = H_0 + \gamma$ and $H_{\downarrow} = H_0 - \gamma$. The asymptotics of the two solutions is

$$\begin{aligned}\chi_{1s}(x) &= \exp(ikx) \quad \text{for } x \geq x_{\mathcal{R}}, \\ \chi_{2s}(x) &= \exp(-ikx) \quad \text{for } x \leq x_{\mathcal{L}},\end{aligned}\tag{4.31}$$

and the retarded Green's function is given by

$$\langle x | G_s^r | x' \rangle = \frac{\chi_{1s}(x_{>}) \chi_{2s}(x_{<})}{W_s},\tag{4.32}$$

where $W_s = \chi_{2s}(x)[\partial\chi_{1s}(x)/\partial x] - \chi_{1s}(x)[\partial\chi_{2s}(x)/\partial x]$ denotes the (x -independent) Wronskian of the two solutions while $x_{>} = \max\{x, x'\}$ and $x_{<} = \min\{x, x'\}$.

The asymptotic behavior of the solution $\chi_{1s}(x)$ for $x \leq x_{\mathcal{L}}$ is given by

$$\chi_{1s}(x) = t_s^{-1} [\exp(ikx) + r_s \exp(-ikx)],\tag{4.33}$$

where we introduced the spin-resolved transmission (t_s) and reflection (r_s) coefficients of the wave incoming from the left. They satisfy the usual condition $|r_s|^2 + |t_s|^2 = 1$ and their

knowledge allows us to evaluate explicitly the Wronskian in Eq. (4.32), $W_s = 2ikt_s^{-1}$, as well as the asymptotics of the solution $\chi_{2s}(x)$ for $x \geq x_{\mathcal{R}}$:

$$\chi_{2s}(x) = \frac{1}{t_s} \exp(-ikx) - \frac{r_s^*}{t_s^*} \exp(ikx). \quad (4.34)$$

These relations yield, e.g., the following elements of the retarded Green's functions:

$$\begin{aligned} \langle x_{\mathcal{L}} | G_s^r | x_{\mathcal{L}} \rangle &= \frac{1}{2ik} [1 + r_s \exp(-2ikx_{\mathcal{L}})], \\ \langle x_{\mathcal{R}} | G_s^r | x_{\mathcal{R}} \rangle &= \frac{1}{2ik} \left[1 - \frac{r_s^* t_s}{t_s^*} \exp(2ikx_{\mathcal{R}}) \right], \\ \langle x_{\mathcal{L}} | G_s^r | x_{\mathcal{R}} \rangle &= \frac{t_s}{2ik} \exp[ik(x_{\mathcal{R}} - x_{\mathcal{L}})]. \end{aligned} \quad (4.35)$$

Other elements, including those of the advanced Green's functions, can be obtained with help of general identities $\langle x' | G_s^r | x \rangle = \langle x | G_s^r | x' \rangle$ and $\langle x | G_s^a | x' \rangle = \langle x' | G_s^r | x \rangle^*$. Since the antihermitean parts of the self-energy $\mathcal{B} = \mathcal{B}_{\mathcal{L}} + \mathcal{B}_{\mathcal{R}}$, Eq. (2.62), are in this particular case given by

$$\begin{aligned} \langle x | \mathcal{B}_{\mathcal{L}} | x' \rangle &= 2k\delta(x - x_{\mathcal{L}})\delta(x' - x_{\mathcal{L}}), \\ \langle x | \mathcal{B}_{\mathcal{R}} | x' \rangle &= 2k\delta(x - x_{\mathcal{R}})\delta(x' - x_{\mathcal{R}}), \end{aligned} \quad (4.36)$$

the total spin-mixing conductance, Eq. (4.20) is equal to

$$C_{\mathcal{L}}^{\text{mix}} = \frac{1}{2\pi} (1 - r_{\uparrow} r_{\downarrow}^* - t_{\uparrow} t_{\downarrow}^*). \quad (4.37)$$

Note that the formula is analogous to sum of Eqs. (144) and (146) of [15] and to Eq. (16) of [91]. The mixing conductance in the first formula (144) corresponds to a situation with only one interface - NM|FM, the transmission across FM layer is included in (146). In the latter reference another FM layer causing the spin accumulation is also taken into account, which leads to additional prefactor to the formula (4.37) present in its counterpart from ref. [91]. This agreement is in fact an extension of the Fisher-Lee's statement [67] that Kubo formula can be expressed in terms of transition probabilities to the area of spin-mixing conductance. Note that the spin-resolved CPP conductances, Eq. (2.69), reduce within the present model to $C_s = |t_s|^2 / (2\pi)$.

4.5 TB-LMTO-CPA formulation and implementation

The formalism of Section 4.2 is well suited for implementation within the *ab initio* TB-LMTO method (Sec. 2.2). The same argumentation as provided in Section III of [62] for charge conductance can be used to derive TB-LMTO formulation of Eq. (4.20). The expression of operators $\mathcal{B}_{\mathcal{L},\mathcal{R}}$ in a LMTO representation is analogous to that of current operators (Eq. 10 of [62]):

$$\mathcal{B}_{\mathcal{L},\mathcal{R}} = \left(\hat{\Delta}^{\alpha} \right)^{1/2} \mathcal{B}_{\mathcal{L},\mathcal{R}}^{\alpha} \left(\hat{\Delta}^{\alpha} \right)^{1/2}. \quad (4.38)$$

Since matrices $\hat{\Delta}^\alpha$ are space diagonal and operators $\mathcal{B}_{\mathcal{L},\mathcal{R}}$ are localized at system boundaries, terms $(\hat{\Delta}^\alpha)^{\pm 1/2}$ present in Eq. (4.38) and Eq. (11) of [62] are localized there as well. Hence these terms are spin-independent and the cancellation of these terms during multiplications involving Green's functions for different spin channels in Eq. (4.20) is not obstructed. An analogue of Eq. (14) of [62], the final TB-LMTO formula for spin-mixing conductance $C_{\mathcal{L}}^{\text{mix}}$ can then easily be derived. Its value per unit two-dimensional (2D) cell is given by

$$C_{\mathcal{L}}^{\text{mix}} = \frac{1}{2\pi} \frac{1}{N_{\parallel}} \text{tr} [i (g_{\uparrow}^r - g_{\downarrow}^a) \mathcal{B}_{\mathcal{L}} - (\mathcal{B}_{\mathcal{L}} + \mathcal{B}_{\mathcal{R}}) g_{\uparrow}^r \mathcal{B}_{\mathcal{L}} g_{\downarrow}^a], \quad (4.39)$$

where N_{\parallel} refers to a large number of 2D cells in directions parallel to atomic layers and the trace is taken over the site and orbital indices of the intermediate region.

For epitaxial systems with perfect 2D translational symmetry, the evaluation of Eq. (4.39) rests on the lattice Fourier transformation of the involved matrices. For FM layers with substitutional disorder, attached to non-random NM leads, the CPA is used for configurational averaging. The configurational average of the second term (quadratic in Green's functions) in Eq. (4.39) has the structure of Eq. (3.1) and thus CPA vertex corrections are to be evaluated for it and this can be done in complete analogy to charge conductance (Chap. 3). The derivation of the general formula for CPA vertex corrections (Eq. 3.4) performed in [74] is valid also in case that the involved Green's functions correspond to different spin channels s, s' . Then:

$$\begin{aligned} \Gamma_{\mathbf{R}}^{s,s'}(z_{\mu}, z_{\nu}) &= \left\langle t_{\mathbf{R}}^s(z_{\mu}) \bar{G}_s(z_{\mu}) B \bar{G}_{s'}(z_{\nu}) t_{\mathbf{R}}^{s'}(z_{\nu}) \right\rangle + \\ &\sum_{\mathbf{R}'(\neq \mathbf{R})} \left\langle t_{\mathbf{R}}^s(z_{\mu}) \bar{G}_s(z_{\mu}) \Gamma_{\mathbf{R}'}^{s,s'}(z_{\mu}, z_{\nu}) \bar{G}_{s'}(z_{\nu}) t_{\mathbf{R}'}^{s'}(z_{\nu}) \right\rangle. \end{aligned} \quad (4.40)$$

Spin indices were located up for $t_{\mathbf{R}}, \Gamma_{\mathbf{R}}$ to maintain readability. The term $\text{tr} \langle (\mathcal{B}_{\mathcal{L}} + \mathcal{B}_{\mathcal{R}}) g_s^r \mathcal{B}_{\mathcal{L}} g_{s'}^a \rangle$ can undergo the same operations that were applied to $\text{tr} \langle g(z_{\mu}) \mathcal{B}_{\mathcal{L}} g(z_{\nu}) \mathcal{B}_{\mathcal{R}} \rangle$ in Sec. 3.3. The formula for VC contribution to this term (analogous to Eq. (4.41) for charge conductance) reads:

$$\begin{aligned} \text{tr} \langle g_s^r \mathcal{B}_{\mathcal{L}} g_{s'}^a (\mathcal{B}_{\mathcal{L}} + \mathcal{B}_{\mathcal{R}}) \rangle_{VC} &= \sum_{p_1 \mathbf{B}_1 \Lambda_1} \sum_{p_2 \mathbf{B}_2 \Lambda_2} \\ &[\bar{g}_{s'}^a (\mathcal{B}_{\mathcal{L}} + \mathcal{B}_{\mathcal{R}}) \bar{g}_s^r]_{p_1, \mathbf{B}_1}^{\Lambda_1} \left[(\Delta_{s,s'})^{-1} (0, E + i0, E - i0) \right]_{p_1, \mathbf{B}_1; p_2, \mathbf{B}_2}^{\Lambda_1 \Lambda_2} [\bar{g}_s^r (\mathcal{B}_{\mathcal{L}}) \bar{g}_{s'}^a]_{p_2, \mathbf{B}_2}^{\Lambda_2} \end{aligned} \quad (4.41)$$

The definitions of $\Delta_{s,s'}$ and terms of the form $[\bar{g}_s \mathcal{B} \bar{g}_{s'}]$ are easy to obtain from their charge conductance counterparts (Eqs. 3.21 and 3.22).

Note that due to Eq. (4.18) the real part of $C_{\mathcal{L}}^{\text{mix}}$ can be expressed in the form of term D_3 from Eqs. (4.17), where both terms are quadratic in Green's functions. TB-LMTO formula analogous to Eq. (4.39) can then be derived:

$$\text{Re } C_{\mathcal{L}}^{\text{mix}} = \frac{1}{2\pi} \frac{1}{N_{\parallel}} \text{tr} [(\mathcal{B}_{\mathcal{L}} + \mathcal{B}_{\mathcal{R}}) (g_{\uparrow}^r - g_{\downarrow}^r) \mathcal{B}_{\mathcal{L}} (g_{\uparrow}^a - g_{\downarrow}^a)]. \quad (4.42)$$

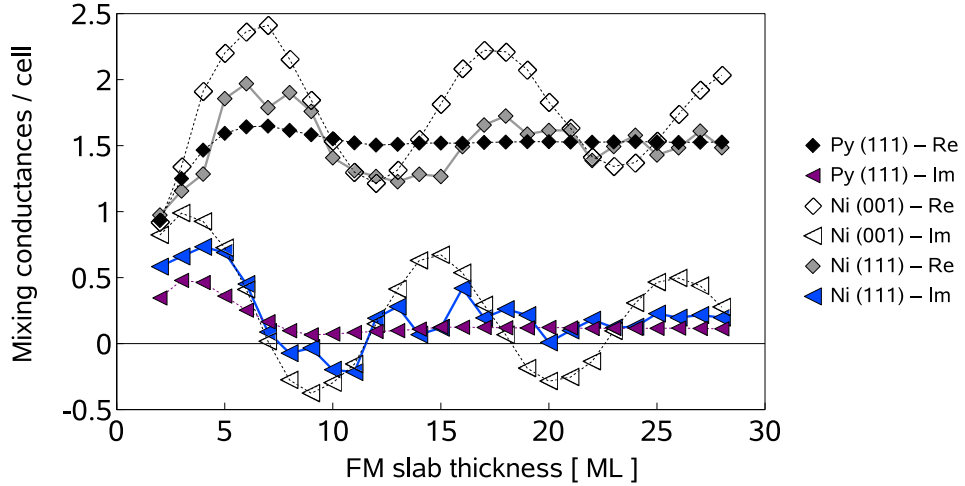


Figure 4.3: fcc Cu | Ni | Cu in (111) and (001) directions and Cu | Py (Ni_{0.84}Fe_{0.16}) | Cu (111) junctions: Real and imaginary parts of spin-mixing conductance as functions of FM layer thickness.

In this case vertex corrections must be evaluated to more terms than in the case of Eq. (4.39). The decomposition of $C_{\mathcal{L}}^{\text{mix}}$ into coherent and incoherent part is then ambiguous. Nevertheless, the physical observable is their sum and it is independent of the choice between Eq. (4.42) and the real part of Eq. (4.39).

4.6 Summary of calculations results

Calculations were performed for model junctions with purely interface scattering (Co and Ni sandwiched by fcc Cu leads, Fe with bcc Cr and V leads), junctions with interface and bulk scattering (disordered Cu_{0.2}Ni_{0.8} and Ni_{0.84}Fe_{0.16} with fcc Cu leads), junctions with halfmetals (Co₂MnSi and Mn-doped GaAs with bcc Cr leads), or tunneling junctions with vacuum between the FM layer and one of the NM leads (Co with fcc Cu leads). All interfaces were clean except for one case (Co with Cu leads), 4 layers of NM leads on each side were included in the intermediate region. The BZ-averages were evaluated using $N_{\parallel} \approx 500$ \mathbf{k}_{\parallel} points in the IBZ (equivalent to about 5000 \mathbf{k}_{\parallel} points in the full 2D BZ).

Dependences of spin-mixing conductance on FM layer thickness are shown in Fig. 4.3 for systems with Ni and permalloy as FM layers, Fig. 4.4 for systems based on Co and Fig. 4.5 for systems based on (Ga_{0.92}Mn_{0.08})As diluted magnetic semiconductor (DMS). Concerning another examined half-metal, Co₂MnSi, the trends (Fig. 8.7) are very similar to that of (Ga,Mn)As. There is one feature which has been found to be common for all examined materials: with respect to the FM thickness the spin-mixing conductance is either a constant or oscillating around a constant value once the thickness is big enough so that interface states do not change. Oscillations are decaying with FM layer thickness until $C_{\mathcal{L}}^{\text{mix}}$ reaches its saturation value.

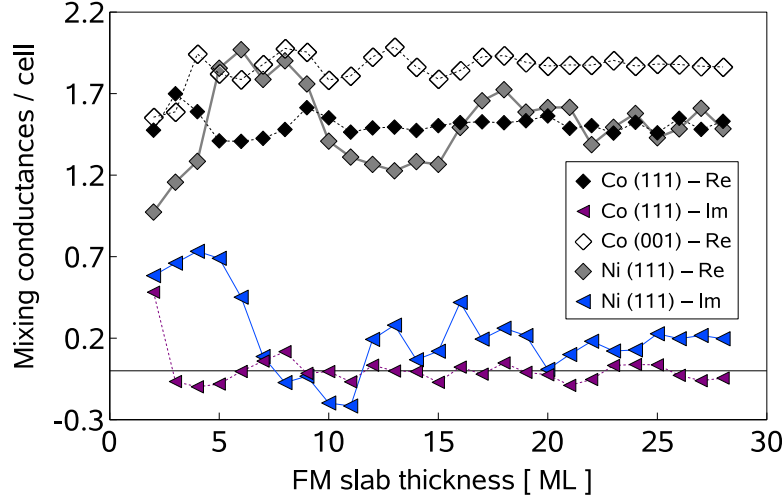


Figure 4.4: fcc Cu | Co | Cu in (111) and (001) directions and Cu | Ni | Cu (111) junctions: Real and imaginary parts of spin-mixing conductance as functions of FM layer thickness. The imaginary part for Cu | Co | Cu (001) is very similar to its (111) counterpart (not depicted).

Note that these quantum oscillations of mixing conductance are present for both pure transition metals but for disordered systems as permalloy and DMS they are smeared out, a necessary precondition for their presence is coherence. The spin-mixing conductance is only weakly affected by interface roughness contrary to the GMR effect, see Fig. 4.6 for $C_{\mathcal{L}}^{mix}$ as a function of interface disorder in Cu | Co | Cu junctions. Figs. 4.6 and 4.5 provide also information about the participation of the coherent and incoherent contributions to $\text{Re } C_{\mathcal{L}}^{mix}$ obtained from Eq. (4.42). If $\text{Re } C_{\mathcal{L}}^{mix}$ is calculated from Eq. (4.39), the vertex contributions are generally much smaller. The fact that for vanishing interface disorder the incoherent part approaches zero helps to verify that the CPA implementation is correct.

There is also an apparent difference in the extent of quantum oscillations between Co and Ni (Fig. 4.4), oscillations of the former one are generally weaker and they are damped much faster. For half-metallic Co_2MnSi oscillations almost completely vanish even without disorder (Fig. 8.7). This can be ascribed to the difference of magnetic exchange splitting between the two metals, which is much bigger in Co than Ni. States propagating across FM layer and non-collinear to its magnetization precession, see explanation of this phenomena in Sec. 5.1. The frequency of this precession is different for different points of Fermi surface, which leads to cancellation of these states on average for sufficiently thick FM layers [15]. The precession frequency depends also linearly on the exchange splitting, therefore the contribution to spin-mixing conductance due to transmission across FM layer vanishes on much shorter distance for materials with bigger splitting (Co, Co_2MnSi). This behavior is equivalent to the very short magnetic coherence length and it proves that the spin-mixing conductance is predominantly an interface property for these metals. On the contrary, the transmission contribution to spin-mixing conductance remains quite high in Ni based

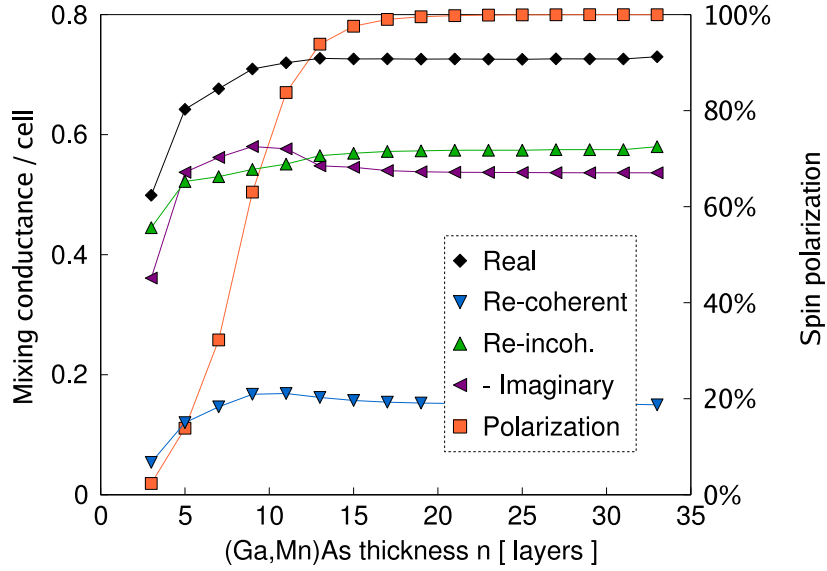


Figure 4.5: Thin Cr | $(\text{Ga}_{0.92}\text{Mn}_{0.08})\text{As}$ | Cr slabs: Real and imaginary parts of the spin-mixing conductance, the decomposition of the real part into coherent and incoherent contributions based on results of Eq. (4.42) and CPP conductance spin polarization as functions of $(\text{Ga}_{0.92}\text{Mn}_{0.08})\text{As}$ layer thickness. The sign of the imaginary part is reversed to allow better graph composition.

junctions. The often adopted neglect of this term (for example the Valet-Fert model) is not justified in this case. Note that there is also a significant difference between the extent of oscillations for (001) and (111) directions (Fig. 4.3), this can probably be ascribed to different Cu - Ni Fermi surface matching in these two cases. Less distinct difference can be seen between (001) and (111) Cu | Co | Cu junctions (Fig. 4.4).

4.6.1 Properties of saturated mixing conductance

Table 4.1 provides a comparison of spin-mixing and CPP charge transport properties of selected NM | FM | NM junctions representatives. Once the saturation thickness is reached the spin current is completely absorbed in all transition metal systems and the real part of the mixing conductance per unit cell is thus proportional to Sharvin conductance of leads C_N^{Sh} . This finding is in agreement with the conclusions of [89].

Another interesting observation is the fact that the imaginary part of C^{mix} approaches zero or is at least an order of magnitude lower than the real part for junctions based on transition metal ferromagnets once the saturation thickness was reached; the same thing was found also in other works [87, 89]. This property has been employed in a number of theoretical studies concerning steady-state torques [81, 82] and angular magnetoresistance [92] of spin valves as well as magnetization dynamics of thin FM films [89]; its validity, however, has to be checked in each particular case. Our calculations show that $(\text{Ga}, \text{Mn})\text{As}$

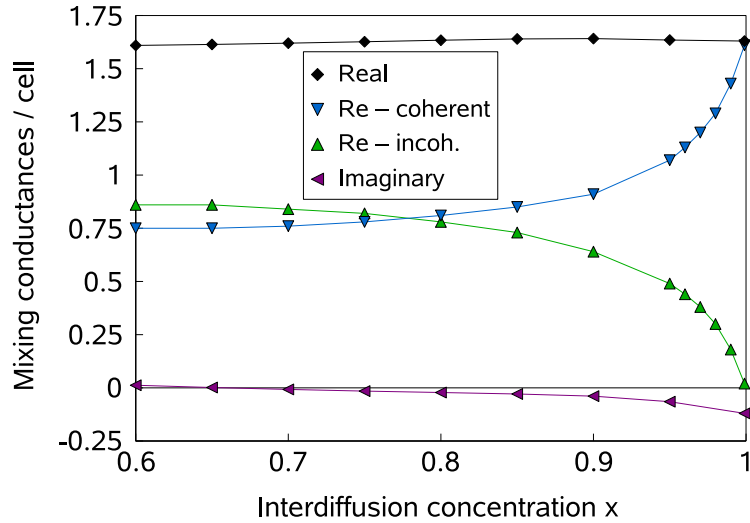


Figure 4.6: Real and imaginary parts of spin-mixing conductance and the decomposition of the real part into coherent and incoherent contributions based on results of Eq. (4.42) as functions of interdiffusion concentration x in fcc Cu | 4 ML Co | Cu (111) system.

and Co_2MnSi do not have this property, an explanation of this based on the free-electron model was proposed for the Co_2MnSi case [16].

In (Ga,Mn)As based diluted magnetic semiconductors the average exchange splitting is much smaller than in the $3d$ transition metals and the size of the Fermi surface for the spin-up channel is small. This could enhance the coherence length [15, 82], because it probably prevents the possibility of cancellation of contributions with different \mathbf{k}_{\parallel} vectors [15] common in transition metal systems. It is interesting to see that the thickness dependence of $\text{Re } C_{\mathcal{L}}^{\text{mix}}$ is almost immediately saturated, which can probably be ascribed to disorder destroying the coherence, but $\text{Im } C_{\mathcal{L}}^{\text{mix}}$ is far from zero while also being not oscillatory.

For (Ga,Mn)As junctions both real and imaginary parts of the mixing conductance increase with Mn-content x in a similar way as the charge conductance or spin polarization, the ratio between $\text{Re } C^{\text{mix}}$ and C remains roughly the same when Mn concentration is varied. This behavior was not observed in any other system, disorder induced reduction of conductance had no effect on the saturated mixing conductance; it can probably be ascribed to a change of Fermi surface due to Mn-content change. The advantage of (Ga,Mn)As is its good $C_{\mathcal{L}}^{\text{mix}}/C$ ratio together with low energetic barrier against magnetization change. Successful experiments with magnetization reversal have already been performed in (Ga, Mn)As at critical currents significantly lower than for other systems [93].

4.6.2 Magnetic tunneling junctions

Our calculations also confirm the previous result [87, 94] that in properly designed magnetic NM | FM | Vac | NM tunneling junctions (Fig. 4.8) the total charge conductance C can be made arbitrarily small, while the mixing conductance $C_{\mathcal{L}}^{\text{mix}}$ remains of the same order

Table 4.1: Saturated spin-mixing conductances $C_{\mathcal{L}}^{mix}$ (in atomic units) for selected thin layers, its ratio to charge conductance C and Sharvin conductances of NM leads C_N^{Sh} . Saturation values are calculated as averages over 10 thickest calculated slabs. For strongly oscillating Cu | Ni | Cu (001) the average is taken over its last period. Note that conductance of (Ga,Mn)As decays quickly with its thickness, the value for thickness of 9ML is taken to provide rough orientation.

material/leads	Re $C_{\mathcal{L}}^{mix}$	Im $C_{\mathcal{L}}^{mix}$	Re $C_{\mathcal{L}}^{mix}/C$	C_N^{Sh}
Cu Ni Cu fcc(111)	1.53	0.16	1.37	1.59
Cu Cu _{0.2} Ni _{0.8} Cu fcc(111)	1.51	0.14	2.01	1.59
Cu Ni _{0.84} Fe _{0.16} Cu fcc(111)	1.53	0.11	2.05	1.59
Cu Co Cu fcc(111)	1.52	-0.02	1.55	1.59
Cu Ni Cu fcc(001)	1.74	0.11	1.35	1.86
Cu Co Cu fcc(001)	1.88	0.06	1.79	1.86
V Fe V bcc(001)	2.79	-0.23	1.99	2.93
Cr Fe Cr bcc(001)	2.41	-0.07	2.08	2.43
Cr (Ga _{0.92} Mn _{0.08})As Cr bcc(001)	0.71	-0.58	4.06	5.24
Cr Co ₂ MnSi Cr bcc(001)	4.74	2.46	11.97	5.24
Cu Co Vac Cu fcc(111)	1.47	-0.06	3.4×10^{10}	1.59

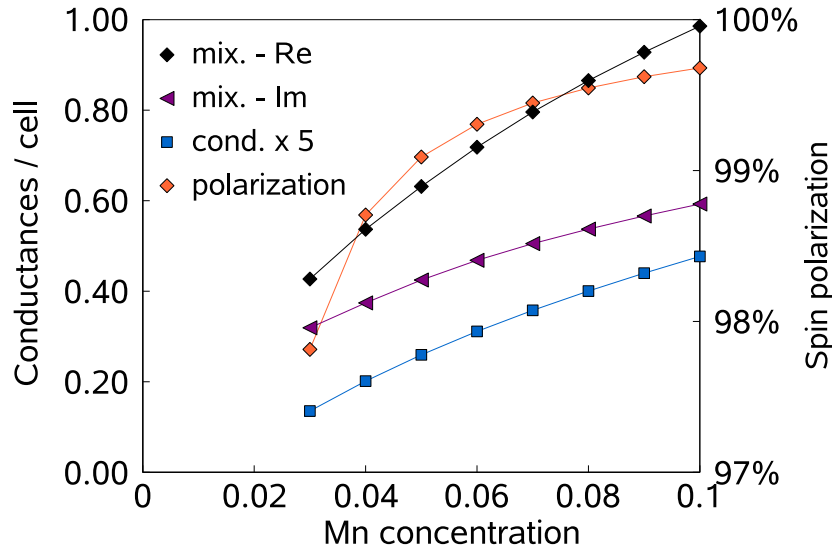


Figure 4.7: Cr | 21ML (Ga_{1-x}Mn)As | Cr slabs: Spin-mixing conductances, CPP charge conductances and its spin polarization as functions of Mn concentration x .

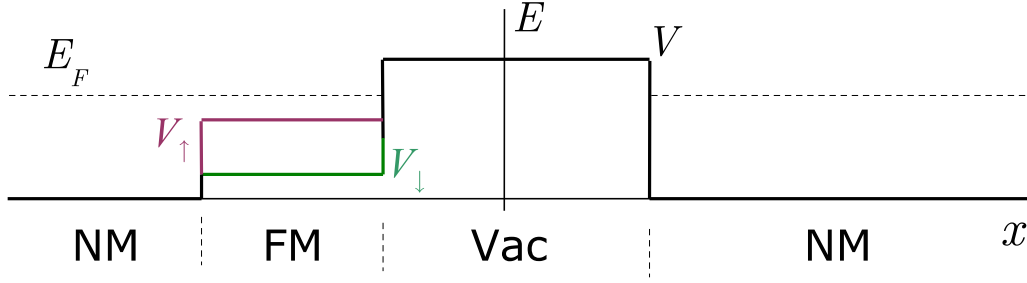


Figure 4.8: Magnetic tunneling junction with a schematic graph of one-electron potentials and the Fermi energy.

as without tunneling. This can be seen from a perturbation expansion with respect to exchange splitting ($V_{\uparrow} - V_{\downarrow}$) in the FM layer. If g_{\uparrow} is considered as a perturbation to g_{\downarrow} : $g_{\uparrow} = g_{\downarrow} + g_{\downarrow} T g_{\downarrow}$, the T-matrix is given as follows:

$$T = (V_{\uparrow} - V_{\downarrow}) [1 - g_{\downarrow} (V_{\uparrow} - V_{\downarrow})]^{-1}. \quad (4.43)$$

Matrix T is nonzero only inside FM layer, the set of layer indices associated with it is denoted as F . Terms of the form $(g_{\uparrow} - g_{\downarrow})_{p,p'}$ present in Eq. (4.42), where p, p' are layers adjacent to one of the leads (\mathcal{L}, \mathcal{R}), can be expanded as

$$\begin{aligned} (g_{\uparrow} - g_{\downarrow})_{\mathcal{L},\mathcal{R}} &= g_{\downarrow,\mathcal{L},F} T g_{\downarrow,F,\mathcal{R}} \\ (g_{\uparrow} - g_{\downarrow})_{\mathcal{L},\mathcal{L}} &= g_{\downarrow,\mathcal{L},F} T g_{\downarrow,F,\mathcal{L}}. \end{aligned} \quad (4.44)$$

Note that $g_{\downarrow,\mathcal{L},F}$ is not crossing the vacuum area therefore the term $(g_{\uparrow} - g_{\downarrow})_{\mathcal{L},\mathcal{L}}$ is not exponentially damped. In the TB-LMTO formulas for spin-mixing conductance $C_{\mathcal{L}}^{mix}$ (4.42, 4.39) there is always a term where only Green's functions on the left side of the junction are involved, which is thus not suppressed if FM layer is located left from the vacuum area. Similarly for a spin-mixing conductance due to spin accumulation in right lead $C_{\mathcal{R}}^{mix}$ a term with only Green's functions on the right side is present and it is non-negligible if FM layer is right from the vacuum area. However, charge conductance (2.68) contains always Green's function across the junction and these must be exponentially damped when tunneling occurs. This is illustrated in Tab. 4.1 by a Cu | Co | Vac | Cu junction, where Vac represents 6 monolayers of empty spheres.

Chapter 5

Spin torques in non-collinear layered systems

Consider electrons incident on a ferromagnetic (FM) layer with a spin polarization non-collinear to FM magnetization direction. Their state is not an eigenstate inside the FM layer and decays exponentially with its thickness. Electrons lose their original moment, which is then transferred into the FM layer and exerts the *spin torque* on it. The problems mentioned in previous chapters were evaluated using the two-current model in which one assumes that the effect of spin polarized currents can be described in terms of separately calculated spin-up and spin-down currents. However, a complete model of a structure exhibiting current induced magnetization reversal must contain non-collinear magnetizations, so the electrons can possess non-collinear spin polarizations. This problem cannot be simplified to a two-current model, relevant quantities are vectors in spin space and can be conveniently represented by 2×2 matrices. The non-collinearity represent a formidable challenge in the formulation of a computational model, in fact majority of operations involved in quantity evaluations have to be reprogrammed to respect the general spin structure. There are many non-collinear structures, which can exhibit current induced magnetization reversal. The simplest one is the so called spin valve composed of two FM layers separated by a NM spacer and connected to NM leads (Fig. 5.1), where the first magnetic layer FM1 simply polarizes the current, and the polarized current exerts the torque on the FM2 layer. Domain walls traversed by a current represent another example of such structure, here the torque causes steady movement of the domain wall. Current induced domain wall propagation [95] is currently quite well experimentally examined and may lead to important applications in the data storage area. A principally similar effect is expected to be possible in spin spirals, but has not been experimentally observed yet [96].

5.1 Spin currents and spin-transfer torques

Apart from standard charge current, a spin current density can be defined:

$$\overleftarrow{\mathbf{I}}^{\sigma}(\mathbf{r}) = i\text{Re}[\Psi^*(\mathbf{r}) \boldsymbol{\sigma} \otimes \mathbf{v}\Psi(\mathbf{r})], \quad (5.1)$$

where $\boldsymbol{\sigma} = (\hat{\sigma}_x, \hat{\sigma}_y, \hat{\sigma}_z)$ is the vector of Pauli matrices.

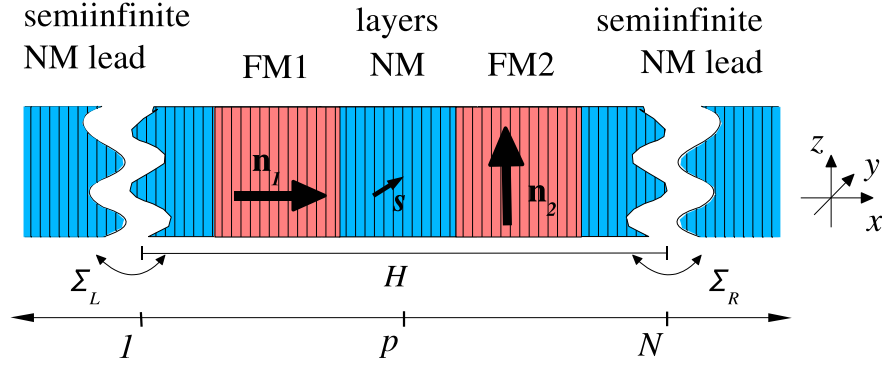


Figure 5.1: Junction comprising two FM slabs with non-collinear (in this case perpendicular) magnetizations sandwiched by NM leads. The direction of the spin accumulation \mathbf{s} generated in the NM spacer by current lies in the $x - z$ plane.

Let us examine its basic properties, mainly a continuity equation, which should be consistent with the definition (5.1). We choose to show the derivation for the direction of an arbitrary Pauli matrix $\hat{\sigma}_\alpha$ to maintain clarity about the structure of involved quantities in spin space, a general vector of Pauli matrices can of course be decomposed to it. Time derivative of the spin-density matrix is given as

$$\frac{\partial}{\partial t} (\Psi^* \hat{\sigma}_\alpha \Psi) = \left(\frac{\partial}{\partial t} \Psi^* \right) \hat{\sigma}_\alpha \Psi + \Psi^* \hat{\sigma}_\alpha \frac{\partial}{\partial t} \Psi, \quad (5.2)$$

explicit \mathbf{r} dependence of $\Psi(\mathbf{r})$ matrices is omitted. The Schrödinger equation can be employed:

$$\frac{\partial}{\partial t} \Psi = -i \left(-\Delta \hat{1} + V_p \hat{1} + \hat{V}_s \right) \Psi, \quad (5.3)$$

where V_p and \hat{V}_s are spin-independent and spin-dependent parts of the Hamiltonian. The latter vanishes in the non-magnetic parts of the system. Unit matrix in spin space ($\hat{1}$) will be omitted in the following text. Substituting (5.3) into (5.2) leads to

$$\frac{\partial}{\partial t} (\Psi^* \hat{\sigma}_\alpha \Psi) = i \left(-\Delta + V_p + \hat{V}_s \right) \Psi^* \hat{\sigma}_\alpha \Psi + i \Psi^* \hat{\sigma}_\alpha \left(\Delta - V_p - \hat{V}_s \right) \Psi. \quad (5.4)$$

Using the fact $\sigma_\alpha^T = \sigma_\alpha^*$ valid for all Pauli matrices, after a few manipulations the Eq. (5.4) is simplified:

$$\frac{\partial}{\partial t} (\Psi^* \hat{\sigma}_\alpha \Psi) = -i (\Delta \Psi^*) \hat{\sigma}_\alpha \Psi + i \Psi^* \hat{\sigma}_\alpha \Delta \Psi + i \Psi^* \left[\hat{V}_s, \hat{\sigma}_\alpha \right] \Psi. \quad (5.5)$$

Then the first two terms on the RHS can be identified with the divergence of the spin current density (Eq. 5.1) projected to direction σ_α :

$$i \nabla \cdot (\Psi^* \hat{\sigma}_\alpha \nabla \Psi - \Psi \hat{\sigma}_\alpha^* \nabla \Psi^*) = \nabla \cdot \hat{\mathbf{I}}_\alpha^\sigma. \quad (5.6)$$

Contrary to the charge conductance the continuity equation contains an additional term $i\Psi^* \left[\hat{V}_s, \hat{\sigma}_\alpha \right] \Psi$, in vector formulation $i\Psi^* \left[\hat{V}_s, \boldsymbol{\sigma} \right] \Psi$. As was already pointed out [84], spin is generally not conserved and the additional term corresponds to an influence of a spin-split potential. For the potential given by a magnetic exchange field \mathbf{B} , the term reads $i \left[\mathbf{B} \cdot \boldsymbol{\sigma}, \boldsymbol{\sigma} \right] = 2\mathbf{B} \times \boldsymbol{\sigma}$ due to the Pauli matrix algebra. This term perpendicular to both the magnetic field and the spin density is apparently similar to the precession term present in the *Landau-Lifshitz-Gilbert* equation. In a ferromagnet, where the field \mathbf{B} corresponds to its exchange field, this spin-precession term contains averages over many states with different Larmor frequencies, which leads to a quick relaxation of terms in the spin-density matrix non-collinear to the magnetization \mathbf{n} in the ferromagnet [86]. However presence of these terms due to divergence of spin current also twists the magnetization of the FM layer and the effective field \mathbf{B} , the absorbed spin is transferred to the lattice magnetization giving rise to *spin-transfer* torque $\boldsymbol{\tau}$. These processes have to be studied in more detail when the dynamics of *spin-transfer torque* generated rotation is examined, here we restrict only to evaluation of torque $\boldsymbol{\tau}$ acting to a FM layer with prescribed uniform magnetization direction \mathbf{n} and not its further evolution. A discussion about how the *spin-transfer torque* is balanced by the torque exerted by the effective magnetic field and the relations valid for the spin-current divergence in a steady state can be seen in [97].

The mechanism of the spin-precession term leads to the quick decay of spin current component perpendicular to the magnetization direction \mathbf{n} of FM layer [15] so that the current leaving the sufficiently thick FM layer is polarized parallel to \mathbf{n} . Note that the component parallel to the magnetization can be understood completely within the two-current model (with no non-collinearity taken into account), it can be only reflected or transmitted as it is unaffected by the spin-precession term. The spin-precession term is perpendicular to \mathbf{n} and the torque $\boldsymbol{\tau}$ is too. In order to find $\boldsymbol{\tau}$ it is natural to evaluate spin currents in NM regions adjacent to the FM region. The spin-precession term is zero there (without the *spin-orbit coupling*), hence spin current is conserved and its value does not depend on a position inside the NM region. A deviation from the equilibrium (non-polarized) spin density called spin accumulation (Sec. 4.1) may arise there because of spin currents and it is not destroyed as in FM layer. *Spin-transfer torque* acting on a subsequent FM layer can alternatively be related directly to it.

The additional source term in continuity equation is also denoted as angular spin current and this kind of continuity equation is analogous to a flow of a classical vector [98]. If *spin-orbit coupling* is included in \hat{V}_s and thus participates in the angular spin current, it becomes particularly important to postulate a better definition of the spin current so that it remains conserved [99]. Within fully relativistic treatment a suitable generalization of spin density has been discovered, leading to a new definition of spin current; *spin-transfer torque* due to *spin-orbit coupling* has been examined in this framework [100]. Recently a relation between the electrical polarization and the antisymmetric components of the spin current has been found based on fully relativistic theory [101], which allowed to propose a way to measure spin-current directly and thus help experimental characterization of the *spin-transfer torque* phenomena.

5.2 Ab initio formulation

In LMTO approach system's spin-dependent properties are incorporated in the potential function P . In the non-collinear situation these are general matrices in spin space \hat{P} . In the local reference frame associated with its magnetization direction its matrix $\hat{P}(0)$ is diagonal in spin space:

$$\hat{P}(0) = \begin{pmatrix} P^\uparrow & 0 \\ 0 & P^\downarrow \end{pmatrix}. \quad (5.7)$$

Its representation in the global reference frame is obtained using a rotation matrix in spin space, assuming rotation by angle ϑ in the $x - z$ plane:

$$\hat{R}_\vartheta = \begin{pmatrix} \cos \frac{\vartheta}{2} & -\sin \frac{\vartheta}{2} \\ \sin \frac{\vartheta}{2} & \cos \frac{\vartheta}{2} \end{pmatrix}, \quad \hat{P}(\vartheta) = \hat{R}_\vartheta \hat{P}(0) \hat{R}_\vartheta^\dagger \quad (5.8)$$

In principle, self-consistent DFT calculation of electronic structure should be also performed in spin space, leading to an exact knowledge of Green's functions direction in spin space. Our aim here is not to examine systems with complicated non-collinear bulk magnetic structure but only non-collinear arrangement of separated magnetically homogeneous layers. This problem can be replaced within reasonable accuracy by a DFT solution of a corresponding collinear system, parts of its ground state solution corresponding to magnetic layers are then rotated in spin space by means of Eq. (5.8) to attain the desired angle. This is justified by the theory leading to the frozen potential approximation [102]. Differently speaking we assume that the ground state of one magnetic layer is not influenced by a change of magnetization direction of another magnetic layer. It also implicates that the magnetic structure of material is assumed completely known and prescribed initially, deviations from it that would minimize the total energy cannot be found this way, this is the same as for two-current model solutions.

5.2.1 Spin currents from linear response theory

As we have shown *spin torques* acting on FM layers of a magnetic multilayer are closely related to spin currents flowing through the structure. These are not conserved in non-collinear systems, hence the point of their evaluation must be properly chosen. The spin current operator at a given point \mathbf{r} is defined as

$$\mathbf{J}^\sigma(\mathbf{r}) = -i[X(\mathbf{r}), H]\boldsymbol{\sigma}. \quad (5.9)$$

Its linear response to external potential applied at the leads is evaluated (Sec. 2.4), we label it spin conductance \mathbf{C}^σ . For the corresponding spin-torque response we use the term *torkance* \mathbf{C}^τ . One should first check whether the spin conductance fulfills the conditions (2.54) that allow the general linear response formula to reduce to the canonical form (2.43). For this purpose we choose the axis system so that both magnetization directions lie in the $x - z$ plane and the response direction first coincides with the x axis (the in-plane response). Hence the Hamiltonian reads

$$\hat{H} = H_0 + W_x \hat{\sigma}_x + W_z \hat{\sigma}_z, \quad (5.10)$$

where H_0 represents the spin-independent part of the Hamiltonian and W_x, W_z are components of the exchange splitting. The explicit dependence of $H_0, W_{x,z}$ and X on position is omitted for simplicity. The response operator is

$$\hat{A}_{\parallel} = -i [X, \hat{H}] \hat{\sigma}_x = -i [X, H_0 \hat{\sigma}_x + W_x + iW_z \hat{\sigma}_y]. \quad (5.11)$$

Note that both operators X and $W_x, W_z \hat{\sigma}_y$ are diagonal in real space, $W_z \hat{\sigma}_y$ is non-diagonal in spin space, but X is a unit matrix there, hence their commutator is always zero. The operator \tilde{B} corresponds to an external electrostatic potential $\varphi(\mathbf{r})$. Only the trivial choice $\hat{U} = 1 = \hat{U}^{-1}$ satisfies the condition for the Hamiltonian (first Eq. of 2.54). Obviously $\tilde{B}^T = \tilde{B}$, hence $\epsilon = 1$. For the operator $\hat{A}_{\parallel} = -i [X, H_0 \hat{\sigma}_x]$ it follows:

$$-\hat{A}_{\parallel}^T = -i [X, H_0 \hat{\sigma}_x] \quad (5.12)$$

The last condition in (2.54) is therefore satisfied. A similar derivation for $\hat{A}_{\parallel z} = -[X, \hat{H}] \hat{\sigma}_z$ leads to the same conclusion, but for the out-of-plane response $\hat{A}_{\perp} = -i [X, \hat{H}] \hat{\sigma}_y$ the condition (2.54) cannot be satisfied, hence all terms in Eq. (2.51) need to be evaluated. Generally a linear combination of Pauli matrices after the commutator in \hat{A} should fulfill the same condition as the Hamiltonian, and therefore we restrict the calculation to in-plane components. Now the general spin current operator (5.9) is substituted into Eq. (2.43) with the assumption of zero temperature:

$$\mathbf{C}^{\sigma}(E_F) = -\frac{1}{\pi} \text{Tr} \left\{ \text{Im} \hat{G}^r(E_F) [X, H] \boldsymbol{\sigma} \text{Im} \hat{G}^r(E_F) [\phi, H] \right\}. \quad (5.13)$$

5.2.2 TB-LMTO expression

Eq. (5.13) is expressed in the LMTO formulation in a way analogous to that for charge conductance [65]. Note that a transformation to a particular LMTO representation corresponding to its TB form is desirable, and one should find a formulation of (5.13) independent of representation. We follow the way adopted in [62] for charge conductance. All potential parameters (Sec. 2.2.1) are diagonal in space, but now they are general matrices in spin space. Note that the tight-binding Hamiltonian (see Eq. (8) of [62]) therefore contains terms $\left(\hat{\Delta}_{\mathbf{R}l}^{\alpha}\right)^{1/2} \hat{S}_{\mathbf{R}l, \mathbf{R}'l'}(z) \left(\hat{\Delta}_{\mathbf{R}l}^{\alpha}\right)^{1/2}$ off-diagonal in real space, which are now non-trivial in spin space within exchange-split areas, and the commutator $[X, \hat{H}]$ may possibly void the last condition in (2.54). However, consistently with statements in Sec. 5.1 we choose to evaluate spin currents only in NM areas, the operator X is then replaced by a projector Π_{N-N} to (yet unspecified) continuous set of layers terminated at NM areas. The commutator $[\Pi_{N-N}, \hat{H}]$ is non-zero only inside NM areas, where \hat{H} reduces to the form of H_0 and the argumentation of the preceding subsection applies.

For the first-order accuracy, we note that $\hat{G}_{\mathbf{R}, \mathbf{R}'}(z) = \left(\hat{\Delta}^{\alpha}\right)_{\mathbf{R}}^{-1/2} \hat{g}_{\mathbf{R}, \mathbf{R}'}^{\alpha}(z) \left(\hat{\Delta}^{\alpha}\right)_{\mathbf{R}'}^{-1/2}$ remains valid regardless of the spin structure of the involved matrices. These matrices are multiplied by current operators localized at NM areas, hence the only involved spatial parts of matrices $\left(\hat{\Delta}^{\alpha}\right)^{-1/2}$ are also unitary in spin space, so that they commute with $\boldsymbol{\sigma}$.

They can then be canceled with $(\hat{\Delta}^\alpha)^{1/2}$ in the transformed current operator (Eq. (10) of Ref. [62]). Spin conductance formula for non-collinear situations in TB-LMTO is therefore analogous to Eq. (2.59), note that commutators of an operator diagonal in space with H can be replaced by commutators with S :

$$\mathbf{C}_{N-N}^\sigma(E_F) = -\frac{2}{\pi} \text{Tr} \{ \text{Im} \hat{g}^{r,\alpha}(E_F) [\Pi_{N-N}, S^\alpha] \boldsymbol{\sigma} \text{Im} \hat{g}^{r,\alpha}(E_F) [\phi, S^\alpha] \}. \quad (5.14)$$

For the second-order accuracy, the derivation presented in Section III B of [62] holds also for potential parameters given as matrices in spin space. Current operators are again nonzero only in NM regions and $\boldsymbol{\sigma}$ commutes there with the term $(\hat{\Delta})^{-1/2} \{1 + S^\alpha (\alpha - \gamma)\}$ present in the second-order current operator (Eq. (28) of Ref. [62]). Hence it can be shifted so that it is adjacent to $[\Pi_p, S^\alpha]$ and the resulting formula (5.14) is correct up to the second order in energy expansion $\epsilon = E - E_\nu$. The LMTO representation index and energy argument will be omitted from now on.

In order to find the torkances \mathbf{C}_2^τ acting on the monitored magnetic slab (FM2) in a spin valve structure we need to express the spin conductances \mathbf{C}^σ in NM areas on both sides of FM2. One side can correspond to an end of the structure, we choose the right lead (labeled \mathcal{R}), the opposite side is always inside the NM layer between two FM layers and one its layers is chosen and labeled p (Fig. 5.1). The choice of the projector Π_{N-N} to be restricted to layers between p and \mathcal{R} leads directly to torkance evaluation. Term $[\Pi_{N-N}, S^\alpha]$ is nonzero only at the edges of this area, calculation of Eq. (5.14) at these two points separately corresponds to an evaluation of spin conductances at layers p and N (adjacent to \mathcal{R}): \mathbf{C}_p^σ and $\mathbf{C}_{\mathcal{R}}^\sigma$. The torkance acting on the second FM layer is then given by

$$\mathbf{C}_2^\tau = \mathbf{C}_{\mathcal{R}}^\sigma - \mathbf{C}_p^\sigma, \quad (5.15)$$

in agreement with the presented statements about the spin current continuity (Sec. 5.1).

Equation (5.14) can be evaluated using Eq. (2.60) as in Sec. 2.4.1. Equation (2.64) can be utilized only for the commutator $[\phi, S]$, this yields:

$$\mathbf{C}_2^\tau = -\frac{1}{2\pi} \text{Tr} \{ \mathcal{B} \hat{g}^r [\Pi_{N-N}, S] \boldsymbol{\sigma} \hat{g}^r \mathcal{B} (\varphi g^a - g^a \varphi) \}. \quad (5.16)$$

Using the assumption of field source in the left lead ($\mathcal{B}\varphi = \varphi\mathcal{B} = \mathcal{B}_{\mathcal{L}}$) and performing substitution (2.60) backwards leads to the following formula:

$$\mathbf{C}_2^\tau = \frac{i}{2\pi} \text{Tr} \{ [\Pi_{N-N}, S] \boldsymbol{\sigma} g^r \mathcal{B}_{\mathcal{L}} g^a - [\Pi_{N-N}, S] \boldsymbol{\sigma} g^a \mathcal{B}_{\mathcal{L}} g^r \}. \quad (5.17)$$

Spin conductance at the right lead ($\mathbf{C}_{\mathcal{R}}^\sigma$) corresponds to the flux between layers N and $N+1$:

$$\begin{aligned} \mathbf{C}_{\mathcal{R}}^\sigma &= \frac{i}{2\pi} \text{Tr} \{ S_{N,N+1} \boldsymbol{\sigma} \hat{g}_{N+1,1}^r \mathcal{B}_{\mathcal{L}} \hat{g}_{1,N}^a - S_{N+1,N} \boldsymbol{\sigma} \hat{g}_{N,1}^r \mathcal{B}_{\mathcal{L}} \hat{g}_{1,N+1}^a - \\ &\quad S_{N,N+1} \boldsymbol{\sigma} \hat{g}_{N+1,1}^a \mathcal{B}_{\mathcal{L}} \hat{g}_{1,N}^r + S_{N+1,N} \boldsymbol{\sigma} \hat{g}_{N,1}^a \mathcal{B}_{\mathcal{L}} \hat{g}_{1,N+1}^r \}. \end{aligned} \quad (5.18)$$

Employing identities (A16) of [65] leads to a compact formula in the Caroli-like form [64]. The final result is that for the charge conductance (2.68) multiplied by the vector of Pauli

matrices:

$$\mathbf{C}_{\mathcal{R}}^{\sigma}(z_{\mu}, z_{\nu}) = \frac{1}{2\pi} \text{Tr} \{ \hat{g}_{N,1}(z_{\mu}) \mathcal{B}_{\mathcal{L}} \hat{g}_{1,N}(z_{\nu}) \mathcal{B}_{\mathcal{R}} \boldsymbol{\sigma} \} . \quad (5.19)$$

Note that $\mathbf{C}_{\mathcal{R}}^{\sigma}(E + i0, E - i0) \neq \mathbf{C}_{\mathcal{R}}^{\sigma}(E - i0, E + i0)$ since $\hat{\sigma}_y \neq \hat{\sigma}_y^T$. Charge conductance formula for non-collinear situations is obtained from Eq. (5.19) by substitution of $\boldsymbol{\sigma}$ by a unity matrix in spin space. Note that due to the current conservation it is independent of position, but the most convenient choice is to evaluate it at layer N adjacent to the right lead as in Eq. (5.19).

Spin conductance at the opposite side corresponds to the flux between layers p and $p+1$, its expression is analogous to Eq. (5.18), where N is replaced by p . This quantity cannot be reduced to more simple form like Eq. (5.19). The final formula for spin conductance at layer p :

$$\mathbf{C}_p^{\sigma}(z_{\mu}, z_{\nu}) = \frac{i}{2\pi} \text{Tr} \{ \mathcal{B}_{\mathcal{L}} (\hat{g}_{1,p}(z_{\mu}) S_{p,p+1} \boldsymbol{\sigma} \hat{g}_{p+1,1}(z_{\nu}) - \hat{g}_{1,p+1}(z_{\mu}) S_{p+1,p} \boldsymbol{\sigma} \hat{g}_{p,1}(z_{\nu})) \} . \quad (5.20)$$

5.2.3 Ab initio torkance in non-collinear spin valves

For a non-collinear NM | FM1 | NM | FM2 | NM system there is another approach leading very quickly to a torkance formula, limited also to its in-plane part. Note that the torque acting on each FM layer is perpendicular to its magnetization direction as discussed in Sec. 5.1. Therefore the in-plane component of the torque acting on layer FM2 $\boldsymbol{\tau}_{2\parallel}$ is fully determined by the projection of $\boldsymbol{\tau}_2$ to the magnetization direction \mathbf{n}_1 : $|\boldsymbol{\tau}_{2\parallel}| = \boldsymbol{\tau}_2 \cdot \mathbf{n}_1 / \sin \vartheta$, where ϑ is an angle between \mathbf{n}_1 and \mathbf{n}_2 . Also note that this projection equals the projection of the total torque $\boldsymbol{\tau}$ acting on the spin valve, because for FM1 it also holds $\boldsymbol{\tau}_1 \perp \mathbf{n}_1$:

$$\boldsymbol{\tau}_{2\parallel} \cdot \mathbf{n}_1 = \boldsymbol{\tau} \cdot \mathbf{n}_1 . \quad (5.21)$$

The fact that the total torkance can be used instead of a partial one significantly simplifies the calculation. We perform the derivation in NEGF formalism here, similar to the one performed in Sec. 4.2. Operator $\boldsymbol{\tau}$ can be chosen as the examined response operator, the same as in the spin-mixing conductance derivation, and the only physically reasonable quantity, its projection $\boldsymbol{\tau} \cdot \mathbf{n}_1$, is then extracted immediately. In contrast to the assumptions of Sec. 4.2, the perturbation of the Hamiltonian is now due to external electrostatic potential and thus not spin-polarized, the non-collinear spin structure is incorporated into system Green's functions. The first order change of self-energy is then

$$\delta \Sigma_{\mathcal{L}}^{\lessgtr} = f'(E) \mathcal{B}_{\mathcal{L}} \delta \phi_{\mathcal{L}} . \quad (5.22)$$

Substitution of Eqs. (5.23, 4.9, 5.22) into Eq. (4.8) and use of the fact that $[\boldsymbol{\sigma}, \mathcal{B}_{\mathcal{L}}] = 0$ allows to obtain $C_{2\parallel}^{\tau}$, the linear response coefficient for $\boldsymbol{\tau}_{2\parallel}$ given by the final formula:

$$\begin{aligned} C_{2\parallel}^{\tau} \sin \vartheta &= \frac{1}{2\pi} \text{Tr} \{ (\mathbf{n}_1 \cdot \boldsymbol{\sigma}) [i(G^r - G^a) \mathcal{B}_{\mathcal{L}} - G^r \mathcal{B}_{\mathcal{L}} G^a \mathcal{B}] \} \\ &= \frac{1}{2\pi} \text{Tr} \{ (\mathbf{n}_1 \cdot \boldsymbol{\sigma}) [G^r \mathcal{B}_{\mathcal{R}} G^a \mathcal{B}_{\mathcal{L}} - G^r \mathcal{B}_{\mathcal{L}} G^a \mathcal{B}_{\mathcal{R}}] \} \end{aligned} \quad (5.23)$$

In contrast to the derivation of \mathbf{C}_2^τ , Eq. (5.15) the whole formula can be expressed in the Caroli-like form as charge conductance does. For the situation with external potential acting on the opposite side (\mathcal{R}) of the system the torque is found to be:

$$C_{\mathcal{R}2\parallel}^\tau \sin \vartheta = \frac{1}{2\pi} \text{Tr} \{ (\mathbf{n}_1 \cdot \boldsymbol{\sigma}) [G^r \mathcal{B}_\mathcal{L} G^a \mathcal{B}_\mathcal{R} - G^r \mathcal{B}_\mathcal{R} G^a \mathcal{B}_\mathcal{L}] \}, \quad (5.24)$$

which is the exact opposite of Eq. (5.23). This way a crucial feature of current induced magnetization reversal is directly obtained: current direction reversal causes also torque direction reversal [91], which has been already observed in experiments [103] and is in fact used to recognize current induced magnetization switching from other phenomena. We have found that total torque in system is exactly antisymmetric with respect to current direction in agreement with [91], its in-plane component exerted on one of FM layers is then also antisymmetric due to relation (5.21).

Transformation of formula (5.23) to the TB-LMTO formulation is straightforward:

$$C_{2\parallel}^\tau \sin \vartheta = \frac{1}{2\pi} \text{Tr} \{ (\mathbf{n}_1 \cdot \boldsymbol{\sigma}) [\hat{g}_{1,N}^r \mathcal{B}_\mathcal{R} \hat{g}_{N,1}^a \mathcal{B}_\mathcal{L} - \hat{g}_{1,N}^r \mathcal{B}_\mathcal{L} \hat{g}_{N,1}^a \mathcal{B}_\mathcal{R}] \}. \quad (5.25)$$

5.3 Comparison to spin-mixing conductance

We have presented another calculation of spin torques in Chapter 4. Now an obvious question arises, what is the relation of its results to the results of the theory presented here. The first one provides *spin torques* as a response to the spin accumulation, while the second one relates it directly to the electrostatic potential difference (similarly to the well-known charge conductance) of a more complicated structure where the spin accumulation is generated internally. We first verify whether the spin currents present due to the spin accumulation lead to the same spin torque as the approach described in Chap. 4 based on the spin-mixing conductance.

We again examine the NM | FM | NM junction, the spin currents on the two sides of the FM layer can then be defined as

$$\begin{aligned} \mathbf{J}_\mathcal{L} &= -i[\Pi_\mathcal{L}, H_0] \boldsymbol{\sigma} = -i[\Pi_\mathcal{L} \boldsymbol{\sigma}, H], \\ \mathbf{J}_\mathcal{R} &= -i[\Pi_\mathcal{R}, H_0] \boldsymbol{\sigma} = -i[\Pi_\mathcal{R} \boldsymbol{\sigma}, H], \end{aligned} \quad (5.26)$$

where the kinetic energy (intersite hopping) is contained in the spin-independent part H_0 of the Hamiltonian H , Eq. (4.1), and where the $\Pi_\mathcal{L}$ and $\Pi_\mathcal{R}$ denote projection operators on the two NM leads including a few adjacent (non-magnetic) layers of the intermediate region such that $\Pi_\mathcal{L} \gamma = \Pi_\mathcal{R} \gamma = 0$. The spin accumulation ($\delta E_\mathcal{L}$) again acts as an infinitesimal perturbation to the lesser self-energy $\Sigma^<$ (Eq. 4.10), the linear response coefficients for the spin currents are defined as

$$\mathbf{K}_\mathcal{L}^\mathcal{L} = \frac{\delta \bar{\mathbf{J}}_\mathcal{L}}{\delta E_\mathcal{L}}, \quad \mathbf{K}_\mathcal{L}^\mathcal{R} = \frac{\delta \bar{\mathbf{J}}_\mathcal{R}}{\delta E_\mathcal{L}}. \quad (5.27)$$

Their direct evaluation reveals that because of the similar arrangement of Pauli matrices they can be obtained by the same approach as in the section 4.2 for the response coefficient

$\mathbf{C}_{\mathcal{L}}$, Eq. (4.12). The explicit expressions are given by

$$\begin{aligned}\mathbf{K}_{\mathcal{L}}^{\mathcal{L}} &= \frac{1}{2\pi} \text{Tr} [i(\boldsymbol{\sigma}G^r - G^a\boldsymbol{\sigma})(\boldsymbol{\sigma} \cdot \mathbf{a})\mathcal{B}_{\mathcal{L}} - \boldsymbol{\sigma}\mathcal{B}_{\mathcal{L}}G^r(\boldsymbol{\sigma} \cdot \mathbf{a})\mathcal{B}_{\mathcal{L}}G^a], \\ \mathbf{K}_{\mathcal{L}}^{\mathcal{R}} &= -\frac{1}{2\pi} \text{Tr} [\boldsymbol{\sigma}\mathcal{B}_{\mathcal{R}}G^r(\boldsymbol{\sigma} \cdot \mathbf{a})\mathcal{B}_{\mathcal{L}}G^a],\end{aligned}\quad (5.28)$$

where several simple properties of the projectors, such as $[\Pi_{\mathcal{L}}, \Sigma^{r,a}(E)] = 0$ and $\Pi_{\mathcal{L}}\mathcal{B} = \mathcal{B}_{\mathcal{L}}$ (and similarly for $\Pi_{\mathcal{R}}$), were used. Note that $\mathbf{K}_{\mathcal{L}}^{\mathcal{L}} + \mathbf{K}_{\mathcal{L}}^{\mathcal{R}} = \mathbf{C}_{\mathcal{L}}$ which reflects the above mentioned relation between the torque and the spin currents.

The resulting formulas can be summarized as

$$\begin{aligned}\mathbf{K}_{\mathcal{L}}^{\mathcal{L}} &= 2 \text{Re} C_{\mathcal{L}}^{\mathcal{L},\text{mix}} \mathbf{n} \times (\mathbf{a} \times \mathbf{n}) + 2 \text{Im} C_{\mathcal{L}}^{\mathcal{L},\text{mix}} \mathbf{a} \times \mathbf{n} + (C_{\uparrow} + C_{\downarrow})(\mathbf{n} \cdot \mathbf{a})\mathbf{n}, \\ \mathbf{K}_{\mathcal{L}}^{\mathcal{R}} &= 2 \text{Re} C_{\mathcal{L}}^{\mathcal{R},\text{mix}} \mathbf{n} \times (\mathbf{a} \times \mathbf{n}) + 2 \text{Im} C_{\mathcal{L}}^{\mathcal{R},\text{mix}} \mathbf{a} \times \mathbf{n} - (C_{\uparrow} + C_{\downarrow})(\mathbf{n} \cdot \mathbf{a})\mathbf{n},\end{aligned}\quad (5.29)$$

where we introduced complex coefficients in analogy to the spin-mixing conductance, Eq. (4.20), namely

$$\begin{aligned}C_{\mathcal{L}}^{\mathcal{L},\text{mix}} &= \frac{1}{2\pi} \text{tr} [i(G_{\uparrow}^r - G_{\downarrow}^a) \mathcal{B}_{\mathcal{L}} - \mathcal{B}_{\mathcal{L}}G_{\uparrow}^r \mathcal{B}_{\mathcal{L}}G_{\downarrow}^a], \\ C_{\mathcal{L}}^{\mathcal{R},\text{mix}} &= -\frac{1}{2\pi} \text{tr} (\mathcal{B}_{\mathcal{R}}G_{\uparrow}^r \mathcal{B}_{\mathcal{L}}G_{\downarrow}^a).\end{aligned}\quad (5.30)$$

Two comments to these results are now in order. First, the dependence of the spin currents on the orientation of the spin accumulation (\mathbf{s}) and the magnetization (\mathbf{n}), Eq. (5.29), is more complicated than that of the spin torque, Eq. (4.19). Second, an obvious relation $C_{\mathcal{L}}^{\text{mix}} = C_{\mathcal{L}}^{\mathcal{L},\text{mix}} + C_{\mathcal{L}}^{\mathcal{R},\text{mix}}$ can be proved from Eqs. (4.20, 5.30). However, this decomposition does not justify a direct interpretation of the quantities $C_{\mathcal{L}}^{\mathcal{L},\text{mix}}$ and $C_{\mathcal{L}}^{\mathcal{R},\text{mix}}$ as respective contributions to the total spin-mixing conductance due to the left and right spin currents, since the latter contain also terms proportional to the total charge conductance $C_{\uparrow} + C_{\downarrow}$ and parallel to the magnetization direction \mathbf{n} , see Eq. (5.29). Hence, the quantities $C_{\mathcal{L}}^{\mathcal{L},\text{mix}}$ and $C_{\mathcal{L}}^{\mathcal{R},\text{mix}}$ refer only to the transverse components of the left and right spin currents with respect to the exchange field of the FM layer.

In the scattering theory analogy, we can show that Eq. (4.37) can be decomposed to its left and right contributions due to the transverse spin currents, Eq. (5.30) in the same way as $C_{\mathcal{L}}^{\text{mix}}$ is decomposed:

$$C_{\mathcal{L}}^{\mathcal{L},\text{mix}} = \frac{1}{2\pi} (1 - r_{\uparrow}r_{\downarrow}^*), \quad C_{\mathcal{L}}^{\mathcal{R},\text{mix}} = -\frac{1}{2\pi} t_{\uparrow}t_{\downarrow}^* \quad (5.31)$$

We have shown that evaluations of the spin torque from the change of “spin conductances due to spin accumulation” $\mathbf{K}_{\mathcal{L}}$ and from the spin-mixing conductance are in fact equivalent methods, in agreement with the continuity equation for spin currents (5.5). Note that our non-collinear methods provide only the in-plane component of the torque, while from the mixing conductance method in-plane (real part) and out-of-plane (imaginary part) components are obtained. In principle, if the spin accumulation generated in given structure was known, the spin-mixing conductance should give the spin-torque as well as Eq. (5.23). Hence the results of Eq. (5.23) contain in addition to spin-mixing conductance information

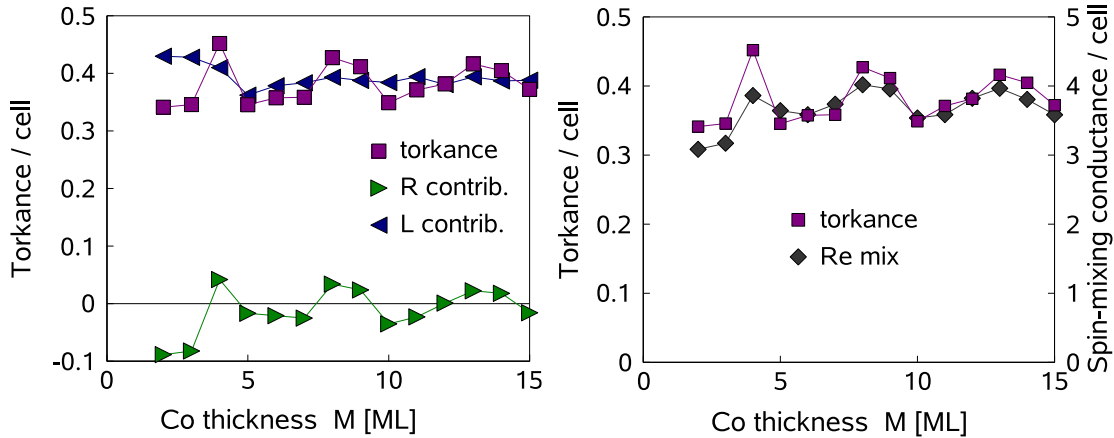


Figure 5.2: Torkances on the second FM layer in fcc Cu | 5ML Co | 3ML Cu | M ML Co | Cu (001) junction with perpendicular oriented magnetizations of Co slabs as function of Co thickness M . Left panel: comparison to its decomposition to contributions due to spin conductances on left and right side of FM2. Right panel: comparison to the real part of spin-mixing conductance of a Co layer of thickness M surrounded by Cu leads.

about the spin accumulation. Information about the spin accumulation can alternatively be obtained from the magneto-electronic circuit theory [15, 86], which is accurate in the limit of purely diffusive transport. When some trends of C^{mix} and C^σ for dependencies where spin accumulation is expected not to be changing significantly are compared, they should be strongly correlated. The right panel of Fig. 5.2 compares these two spin torque coefficients for Cu | Co | Cu | Co | Cu (001) junctions with perpendicular oriented FM slabs and Cu|Co|Cu (001) slabs respectively as functions of Co thickness M , and the correlation is clearly visible. It is interesting to examine the behavior of spin conductances on both sides of the free Co layer (Fig. 5.2, left panel), which together constitute the torkance (Eq. 5.15). The oscillations of the spin torque are mainly due to the variations of the spin conductance on the right side (transmitted spin current), while the oscillations due to reflected spin current are weaker.

Table 5.1 provides a comparison of torkances in the junctions Cu | 5ML Co | 3ML Cu | 11ML \mathbf{X} | Cu (001) and mixing conductances in the junctions Cu | 4ML \mathbf{X} | Cu (001), for two different materials subjected to torque: $\mathbf{X} = \text{Co, Ni}$. Note that both phenomena are influenced by the material change in a roughly similar way, which again supports the statements of the previous paragraph.

These statements should not hold in situations where the spin accumulation changes rapidly with given variable, so that effect observed for spin-mixing conductance or for torkance cannot be seen for the other one. Note the magnetic tunneling junction described in Sec. 4.6 and the surprising behavior of spin-mixing conductance for this system - it almost does not decay when tunneling barrier is enlarged. However, for a spin valve containing such element instead of one of FM layers the spin accumulation should probably decay

Table 5.1: Torkances in junctions Cu | 5ML Co | 3ML Cu | 11ML **X** | Cu (001) and corresponding mixing conductances in junctions Cu | 11ML **X** | Cu (001), for two different materials subjected to torque: **X** = Co, Ni. Ratio between Co and Ni results for both these quantities.

System	$C_{2\parallel}^\tau$	$\text{Re} (C_{\mathcal{L}}^{mix} + C_{\mathcal{R}}^{mix})$	Ratio Co/Ni
Cu 5ML Co 3ML Cu 11ML Co Cu	0.37		1.28
Cu 5ML Co 3ML Cu 11ML Ni Cu	0.29		
Cu 11ML Co Cu		3.59	1.38
Cu 11ML Ni Cu		2.61	

exponentially similar to the charge conductance and so the torkance should. This agrees with our results and it is also supported by the observation that while the formula (4.42) for spin-mixing conductance contains Green's function elements avoiding the tunnel barrier, only those going through it are present in (5.23). Nevertheless, this fact does not mean that the design of such junction lacks any application potential, but it must be updated so that enough spin accumulation is generated by an additional current going in other direction, as was proposed in [87].

5.4 Summary of calculations results

Non-collinear transport calculation was implemented only for systems with no substitutional disorder. All calculations were performed for NM | FM1 | NM | FM2 | NM model spin valves. First we briefly review few important general properties of obtained results. All these properties are expected to be fulfilled if there is no fundamental error in the implementation or formulation of torkance calculation:

- Our calculations have shown perfect agreement between torkances $C_{2\parallel}^\tau$ obtained from (5.23) and a projection of \mathbf{C}_2^τ from (5.15) to the magnetization direction \mathbf{n}_1 , which also corroborates the equivalence of the NEGF and Kubo based derivation here.
- The antisymmetry with respect to current direction found as a consequence of the theory developed for $C_{2\parallel}^\tau$ was also verified by means of \mathbf{C}_2^τ obtained from (5.15). All torkance results will from now on be therefore labeled as $C_{2\parallel}^\tau$ without specifying the method.
- We verified that charge conductance is invariant with respect to an arbitrary rotation of the whole system in spin space.
- For parallel and antiparallel orientations of FM layers torkance vanish.
- Spin conductances are independent of the measurement position within one NM layer.
- The component of torkance \mathbf{C}_2^τ parallel to the magnetization of the FM2 layer vanish, and for torkance \mathbf{C}_1^τ the same is valid concerning the direction parallel to FM1 layer.

Table 5.2: Torkances $C_{2\parallel}^\tau$ and total charge conductances C in junctions Cu | 4ML **X** | 4ML Cu | 4ML Ni | Cu (001) for **X**=Co,Ni and Cu | 4ML **Fe** | 4ML Cu | 4ML **Fe** | Cu (001) with perpendicular magnetizations of FM layers, spin polarization of conductance via Cu | **X** | Cu and Cr | Fe | Cr junctions, and the ratio of $C_{2\parallel}^\tau$ to it.

System	$C_{2\parallel}^\tau$	C	FM1 <i>Pol</i>	$C_{2\parallel}^\tau/C/Pol$
Cu 4ML Co 4ML Cu 4ML Ni Cu (001)	0.38	0.97	31%	1.26
Cu 4ML Ni 4ML Cu 4ML Ni Cu (001)	0.092	1.23	7.2%	1.07
Cr 4ML Fe 4ML Cr 4ML Fe Cr (001)	-0.36	0.81	-46%	0.97

- Spin currents at the NM layer preceding the FM1 layer are polarized mostly in the direction of FM1, while those at NM layer after the FM2 layer are polarized in the direction of FM2, which is consistent with the statements on decaying perpendicular spin current component in Sec. 5.1.

Ab initio formulation of torkance allows to examine the role of FM1, FM2 and NM spacer materials, their thicknesses and the angle ϑ between the two FM layers. The dependence on the switching layer FM2 should be in rough agreement with the information on it from the spin-mixing conductance as is discussed in the preceding section. The polarizing layer FM1 determines the torkance exerted on FM2 mainly by the amount how much does it polarize the current passing through it, this is supported by findings presented in Tab. 5.2. Note that even though torkance differs between systems with Co and Ni as FM1 slab significantly (cca. four times), its ratio to spin polarization of a standalone NM | FM1 | NM junction is very similar. There are slight changes of the ratio caused mainly by the difference between spin polarization in the NM | FM1 | NM junction alone and accompanied by another perpendicularly oriented magnetic slab (FM2). The two FM slabs cannot of course be accurately seen as independent with their effect on spin current summed, that is an idea within the series resistor model (see Sec. 2.3).

This finding about the dependence on FM1 slab polarization also proposes the way to reverse torque direction: Use systems where conductance is polarized opposite to magnetization of FM1, this idea was already realized experimentally [104]. Negative spin polarization (also referred to as negative spin asymmetry) may arise due to scattering properties of particular interfaces with NM metal or due to bulk scattering properties of FM layer influenced suitably by a strong disorder. The latter case is not accessible currently for our non-collinear calculation, but one such system is examined in Sec. 6.4 with respect to its magnetoresistance, which is also impacted. The former case corresponds for example to Fe | Cr (001) interface. This interface prefers minority electrons (with respect to Fe magnetization) and the overall (referred to as net) spin polarization of Cr | Fe | Cr conductance is negative even though standalone Fe layer of course contains more conducting channels for majority electrons, an experimental verification of this fact can be seen in [105]. Inversion of torque direction for this system is clearly obtained from our calculations (Tab. 5.2). Note that spin torque exerted on FM2 layer can be reversed by having negative spin anisotropy corresponding to layer FM1, but not layer FM2.

5.4.1 Angular dependence

Dependences of the total resistance and spin-transfer torque on the FM1 and FM2 relative angle ϑ are one of the most interesting problems to be solved for non-collinear systems. Analytical formulas for these dependencies have been proposed based on experimental findings and justified theoretically [15, 106] for spin valves with identical FM layers within an assumption that electrons' phase coherence is lost between interfaces (semiclassical approximation):

$$\frac{\tilde{R}(\vartheta) - R(0)}{R(\pi) - R(0)} = \frac{1 - \cos(\vartheta)}{\chi(1 + \cos(\vartheta)) + 2} \quad (5.32)$$

$$\tilde{C}_{2\parallel}^{\tau}(\vartheta) = \frac{CP}{8\pi}\omega \frac{\sin(\vartheta)}{1 + \omega - (1 - \omega)\cos(\vartheta)}, \quad (5.33)$$

where

$$\chi = \frac{1}{1 - P^2}\omega - 1, \quad \omega = \frac{|C^{mix}|^2}{C \cdot \text{Re } C^{mix}}, \quad (5.34)$$

and spin polarization P , mixing and charge conductances C^{mix} , C are properties of one of NM/FM/NM junctions.

Torkances and resistances of a Cu | Co | Cu | Co | Cu junction are depicted in Fig. 5.2. We calculate coefficients χ , ω and compare results from (5.32,5.33) to our results in the same Figure, $\tilde{C}_{2\parallel}^{\tau}(\vartheta)$ is multiplied by a constant to best accommodate extent of $C_{2\parallel}^{\tau}$. Note that the agreement between approximate formulas (5.32,5.33) and our more accurate *ab initio* calculations is quite good, especially the angular position of the spin torque extreme. However, the small almost saddle of angular dependence left from the torque maximum is not caught by the simple formula (5.33).

With increasing spin polarization the value of χ grows and with increasing C^{mix}/C both ω and χ grows. This supports the asymmetry of Eq. (5.33) so that its peak angle ϑ_m is shifted towards $\vartheta = \pi$. This prediction is in overall agreement with our results (Tab. 5.3), but some additional subtle phenomena not accounted for in Eq. (5.33) may shift the peak position about $\pm 0.1\pi$. Therefore we rather compare the ratio between the absolute values of torque angular derivatives at angles $\vartheta = 0, \pi$, which should also describe the angular asymmetry:

$$\eta = \frac{\frac{\partial}{\partial \vartheta} \tilde{C}_{2\parallel}^{\tau}(\vartheta = 0)}{\frac{\partial}{\partial \vartheta} \tilde{C}_{2\parallel}^{\tau}(\vartheta = \pi)}. \quad (5.35)$$

Results of this comparison are provided in Tab. 5.3 for selected junctions. A complete angular dependence of a pure half-metal can be seen in Sec. 8.8.

The asymmetry of torkance angular distribution can be understood from examining the asymmetry of spin accumulation in NM spacer, which is commonly higher for situations closer to antiparallel orientation. However if the spin valve is constructed from such materials, that its NM | FM1 | NM part has negative and NM | FM2 | NM part positive net spin polarization (or vice versa), antiparallel alignment of the layers is more conducting, which corresponds to the negative GMR (Sec. 6.4.2). Spin accumulation is then higher for parallel alignment and the torque angular asymmetry is reversed, this is illustrated in Tab. 5.3 for Cr | Fe | Cr | Co₂MnSi | Cr system.

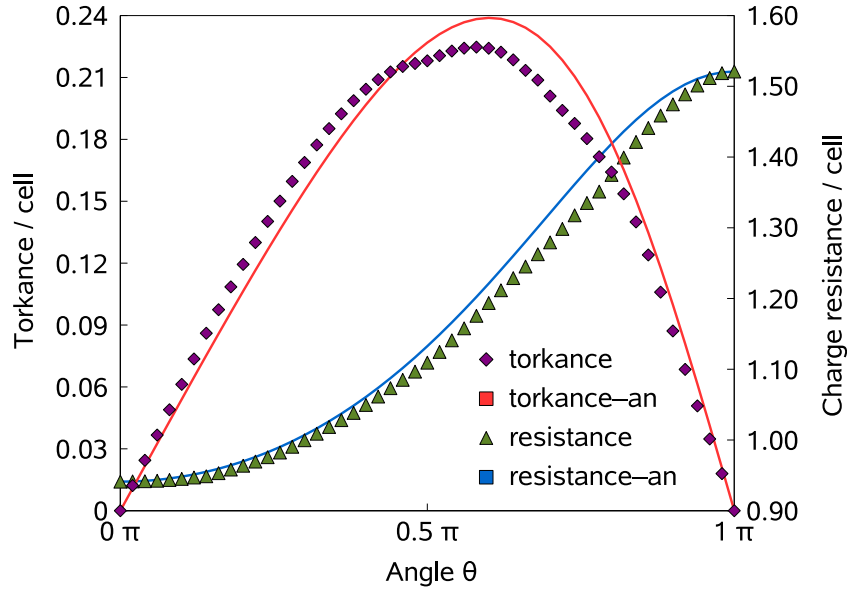


Figure 5.3: Torkances and resistances in fcc Cu | Co | Cu | Co | Cu (001) junction as functions of angle ϑ between the two Co slabs, both from ab initio calculations (markers) and analytical formulas (lines).

Table 5.3: Angle ϑ_m of spin torque angular dependence maximum and ratio η between the absolute values of torque angular derivatives for non-collinear NM | FM1 | NM | FM2 | NM (001) systems compared to ω and ratio $\tilde{\eta}$ between the $\tilde{C}_{2\parallel}^{\tau}(\vartheta)$ derivatives for corresponding NM | FM | NM (001) junctions. The latter are printed only in case that both FM junctions are the same.

System	η	ϑ_m	ω	$\tilde{\eta}$
Cu 4ML Ni 4ML Cu 4ML Ni Cu	0.83	0.50π	1.58	0.74
Cu 4ML Co 4ML Cu 4ML Co Cu	0.69	0.58π	1.73	0.6
Cr 4ML Fe 4ML Cr 4ML Fe Cr	0.73	0.56π	2.06	0.5
Cr 12ML Co ₂ MnSi 8ML Cr 12ML Co ₂ MnSi Cr	0.15	0.80π	17.06	0.09
Cr Fe Cr Co ₂ MnSi Cr	3.15	0.25π		

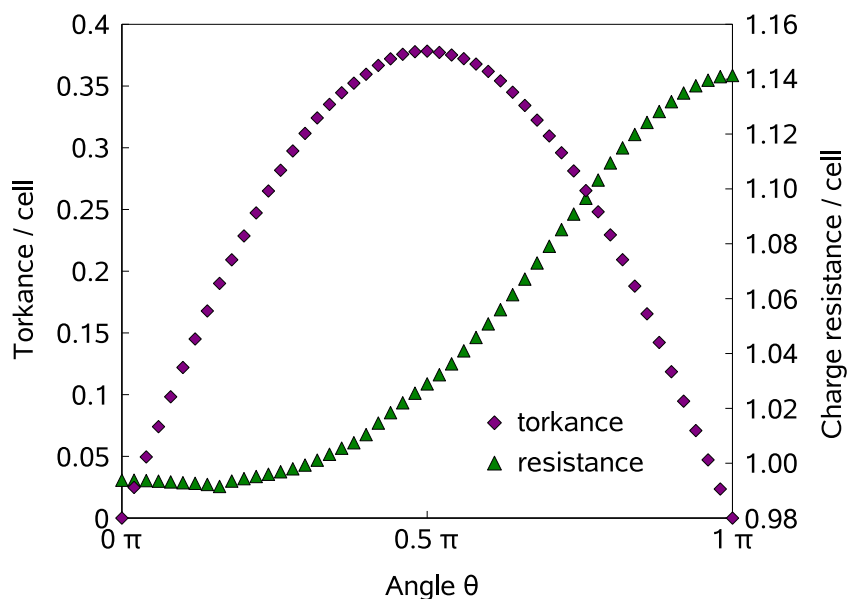


Figure 5.4: Torkances and resistances in fcc Cu | Co | Cu | Ni | Cu (001) junction as functions of angle ϑ between the Co and Ni slabs.

For asymmetric junctions with different CPP conductance spin polarizations or conductivities of FM1 and FM2 layers the angular dependence of resistance can have its minimum localized at angles different from 0 or π , as is discussed in [107] and observed in [108]. Note that spin accumulation is then generated in NM spacer also for the parallel configuration. The nonmonotonic angular dependence is probably caused by the increased possibility of this spin accumulation to transfer into magnetic layers for non-collinear situations, which for low angles surmounts the slower increase of resistance due to transition from parallel to antiparallel state. Angular dependence of conductance and torkance for such asymmetric system is depicted in Fig. 5.4. Note that no apparent deviation of spin-transfer torque from its standard shape is seen.

Chapter 6

Co/Cu based multilayers with substitutional disorder

GMR effect in Co/Cu based multilayers has been observed [109] recently after the initial GMR experiments on Fe/Cr multilayers done by Baibich et al. in 1988[2]. Production of Co/Cu metallic multilayers is well developed and they exhibit a reasonable GMR ratio even at room temperature, while having lower coercivity fields than Fe/Cr. Moreover Cu represents a truly nonmagnetic spacer in contrast to the complicated magnetic structure of Cr. From the theoretical point of view they are based on quite simple transition metals with no significant relativistic contribution, whose electronic structure and other calculation predictions are in good agreement with experiments. Therefore they represent an ideal material to test the validity of presented theories before going to more complicated systems, that may show an even more interesting physical behavior.

6.1 Electronic structure

The self-consistency of one-electron potentials was achieved in intermediate regions comprising also a few (3-5) monolayers of the attached metallic leads. One principal layer (Sec. 2.2.3) was formed by one atomic layer for fcc(111) stacking while two neighboring atomic layers per principal layer were necessary in fcc(001) and bcc(001) cases. The integrations over the 2D BZ were performed on a uniform mesh of about 1000 \mathbf{k}_{\parallel} points to determine the electronic structure.

The key to understand the origin of high magnetoresistance in metallic multilayers is the *band structure* for energies near the Fermi energy. It is well known that there is a very good matching between the *band structures* of Cu and Co \uparrow , while Cu and Co \downarrow exhibit a band mismatch. The calculated *band structures* of these two materials depicted in Fig. 6.1 demonstrate this behavior, which is the source of the high spin polarization of electron scattering at their interfaces leading to GMR phenomena calculated in subsequent sections. Systems with the 2D translational symmetry must in reality be described by the Bloch spectral function which contains peaks of finite width instead of δ -functions, hence the simple band structure picture is inaccurate, but an assumption of bulk-like atoms in the multilayer is sufficient for a qualitative understanding of the multilayer's spin-dependent

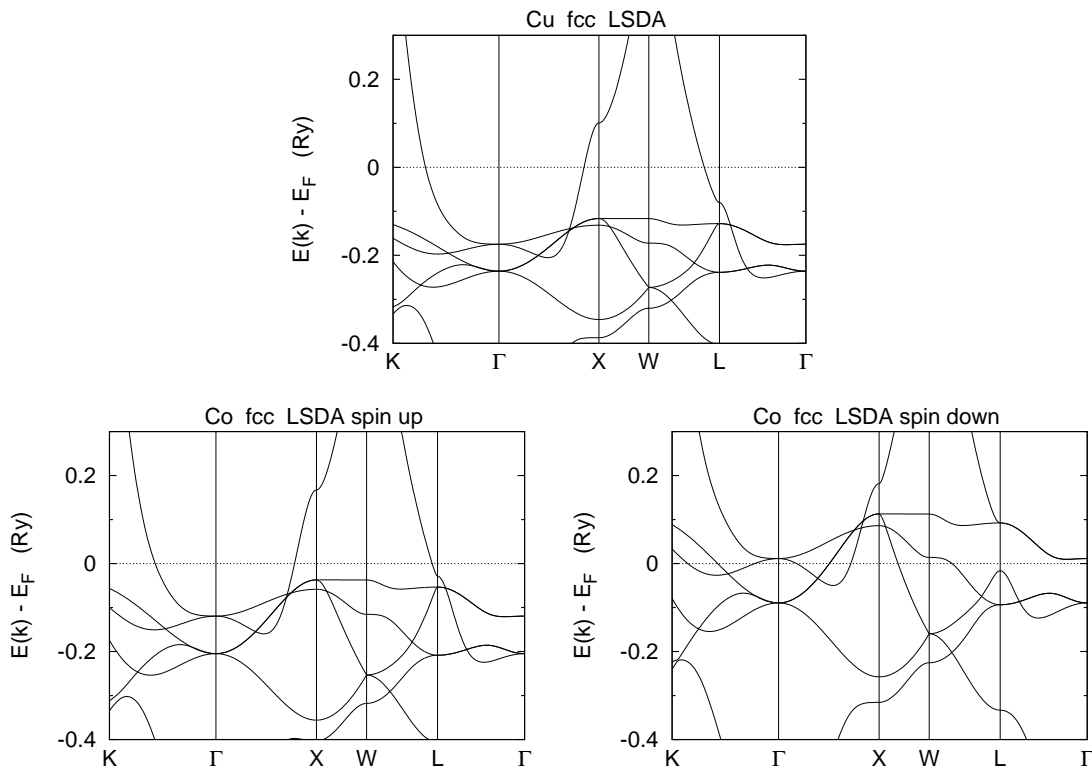


Figure 6.1: Band structures of bulk Cu and Co (spin-resolved).

transport behavior.

6.2 Co | Cu | Co multilayers with interface roughness

At any interface there is always a high probability of interdiffusion of atoms from one side to the other one, thus creating a thin alloyed layer at the interface. The concentration and spatial extend of this layer depends on materials, temperature, manufacturing technique and many other factors, determination of it is not a subject of this work. Here we concentrate on its impact on transport properties, which has shown up impossible to be described by some simplified models and it is not completely understood to date, although this impact is rather high. Experimental characterization of interface roughness is quite difficult and it is rather predicted indirectly. Attempts to describe profile of interfacial impurity concentration have been done based on a comparison of magnetic moments between measurements and theory [110]. There are works which address the GMR effect in Co|Cu|Co multilayers with interface interdiffusion [70, 111]. These calculations are based on the supercell method, which allows us to compare this method to pure CPA calculation. Here we studied fcc(001) 5 ML Co | 4 ML Cu | 5 ML Co trilayers sandwiched by two semi-infinite Cu leads with all four interfaces imperfect; the atoms were placed at sites of an ideal Co fcc lattice (with a lattice parameter smaller by $\sim 2\%$ than that of pure Cu). The interface roughness was simulated

Table 6.1: Trilayer 5ML Co | 4ML Cu | 5 ML Co fcc(001) sandwiched between two Cu leads: spin-resolved CPP conductances and MR ratio for trilayers with ideal and rough interfaces obtained using various methods to treat disorder. SC results taken from [70], CPA results were presented in [14]. AP conductances for both spin channels coincide due to geometric symmetry of the trilayer.

Case	C_{PM}^\uparrow	C_{PM}^\downarrow	$C_{AP}^{\uparrow\downarrow}$	γ
Ideal	0.743	0.238	0.228	1.15
CPA - coherent	0.673	0.016	0.054	5.38
CPA - full	0.722	0.260	0.356	0.38
SC	0.733	0.256	0.354	0.40

by disordered alloys in two atomic layers at each Co/Cu interface; the neighboring layers have composition $\text{Co}_{1-x}\text{Cu}_x$ on the Co side and $\text{Co}_x\text{Cu}_{1-x}$ on the Cu side, where x is a concentration variable, $0 \leq x \leq 0.5$. As noted in [65], the particular thicknesses of the Co and Cu layers are less important for understanding the influence of disorder on the CPP magnetotransport in this model.

6.2.1 Transport properties

Tab. 6.1 shows, what results are provided from various calculation methods for the difference between the transport through ideal and rough interfaces. The presented CPA calculations employed BZ-averages evaluated using $N_{\parallel} \approx 400$ \mathbf{k}_{\parallel} points in the IBZ (equivalent to about 3000 \mathbf{k}_{\parallel} points in the full 2D BZ). Within the CPA it is necessary to calculate vertex corrections for transport properties, because a great portion of the transmission is diffusive, which is a very interesting effect and it cannot be handled by the coherent part of the CPA. The results involving only the coherent part would obviously be completely misleading. Both SC and CPA results also show the high sensitivity of the MR ratio to the interface roughness, which is a crucial information for potential applications.

This effect can be examined in more detail at a dependence of spin-dependent transport on interface interdiffusion concentration x (Fig. 6.2). This dependence is much more easily obtained within the CPA than the SC method because very small changes of concentration can be reflected only if very big supercells are used. For the AP conductance, the interdiffusion obviously opens large amount of new conduction channels, and this effect dominates over almost unchanged $\text{PM}\uparrow$ and slightly varying $\text{PM}\downarrow$ conductance. This massive increase of AP conductance causes the decrease of the MR ratio γ from approx. 115% for ideal interfaces to its minimum value 37% with the interdiffused atoms concentration around $x = 0.2$. Another interesting thing is the fact, that introduction of even a very small interdiffusion concentration $x < 0.1$ has a great impact on the magnetoresistance, which is rapidly decaying with x in this area, while then for x in the range 0.1 – 0.4 the change in magnetoresistance is almost negligible (37% - 43%). We observed this behavior also for other multilayers. This strong sensitivity of MR ratio to small amount of interface disorder contradicts a recent prediction of minor GMR changes due to the rough interfaces

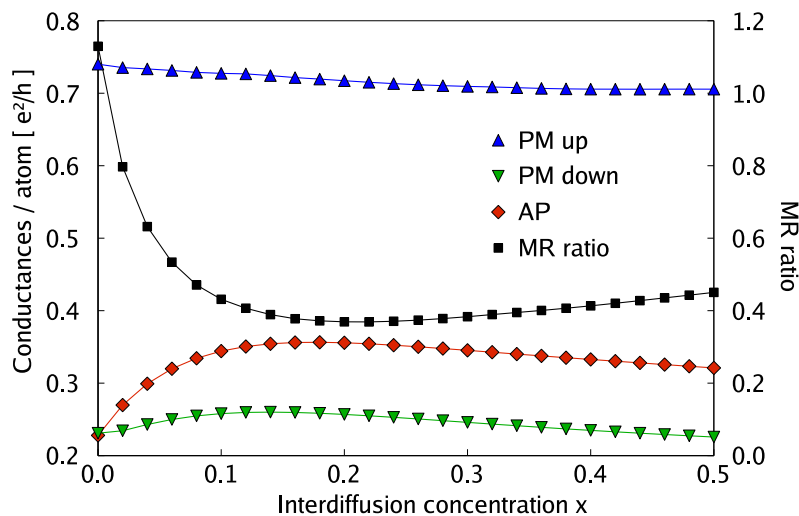


Figure 6.2: Spin-resolved CPP conductances in PM and AP arrangements and the MR-ratio for fcc(001) 5 ML Co|4 ML Cu|5 ML Co trilayers sandwiched by two Cu leads as functions of the concentration x of interdiffused atoms at the rough interfaces [14].

[112]. Note however that the SC calculations of Ref. [112] were performed only for a single Co/Cu(001) interface while the present model contains four intermixed interfaces; the MR-ratio decreases with increasing number of rough Co/Cu interfaces, as shown in another SC study [65]. Reflection and transmission probabilities and specularity parameters of a single rough Co/Cu(001) interface have recently been investigated using a LKKR-CPA approach [113]. In agreement with the present results, the calculated probabilities of Ref. [113] exhibit pronounced changes due to a small ($x \sim 0.1$) amount of disorder; however the underlying \mathbf{k}_{\parallel} -resolved quantities are based on a highly simplified form of the VC and their reliability for a thorough quantitative analysis is thus limited.

6.2.2 Comparison to supercell calculations

We compare our results with supercell calculations from work [70], see Tab. 6.1. Obviously the agreement between the SC and CPA calculations is almost perfect. This demonstrates that the CPA, an effective-medium theory, is reliable even for 2D alloys, in contrast to common wisdom on a general failure of mean-field like approaches in low-dimensional systems. The present case, however, is not a genuine 2D system: the imaginary parts of self-energies of the (nonrandom) metallic leads play a significant role for the success of the CPA. Also the CPA results provide an independent validity check of previous SC calculation results, which could have been affected by supercell size or by an incorrect choice of a limited set of evaluated configurations.

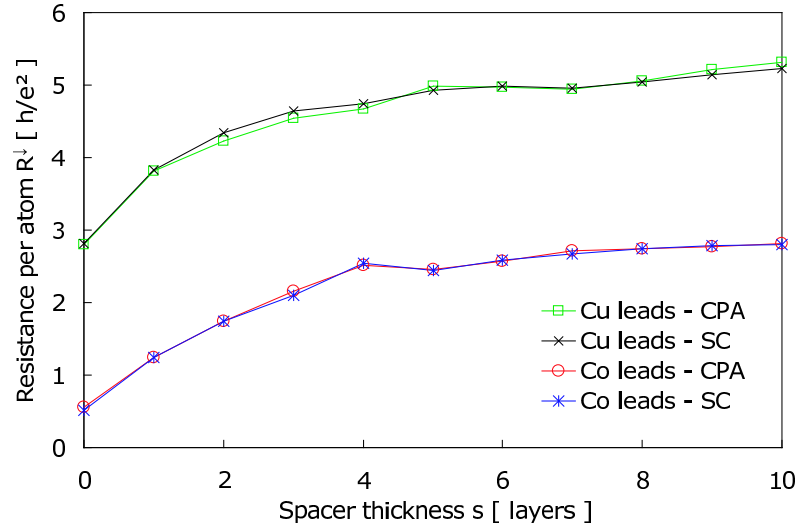


Figure 6.3: Resistances per one interface atom of the fcc(001) 5 ML Co| s ML Cu_{0.84}Ni_{0.16}|5 ML Co trilayers sandwiched by two pure fcc(001) Cu and Co leads for minority electrons and the FM orientation of the Co slabs. The present CPA values [14] are compared to the SC results of Ref. [70].

6.3 Co | Cu_{0.84}Ni_{0.16} | Co trilayers with randomness in the spacer

Systems with magnetic impurities in a nonmagnetic spacer represent another challenge for CPA transport calculation, now the disorder is spread across the whole slab. The effect of random Ni impurities in the Cu spacer on the CPP transport in fcc(001) Co/Cu/Co trilayers has been studied in detail by the SC technique [70]. For this reason we focus merely on a comparison of the present CPA results to the existing SC values for two cases, namely for fcc(001) 5 ML Co| s ML Cu_{0.84}Ni_{0.16}|5 ML Co trilayers sandwiched by two pure fcc(001) Cu and Co leads. Note that the latter case refers to the CuNi slab embedded between two semi-infinite Co leads. We have taken the ideal fcc Co lattice in both cases (see Section 6.2) and considered the minority spin ($\sigma = \downarrow$) channel of the FM arrangement with the CuNi spacer thickness s varying in the range $1 \leq s \leq 10$.

The results are plotted as resistances $R_{\text{FM}}^{\downarrow}(s) = 1/C_{\text{FM}}^{\downarrow}(s)$ in Fig. 6.3. The depicted resistances prove a very good quantitative agreement between the two approaches (CPA, SC) for both leads (Cu, Co); in particular, the different slopes of $R_{\text{FM}}^{\downarrow}(s)$ for very thin spacers as compared to thicker spacers are clearly reproduced. This phenomenon can be explained by quantum-well states formed in Cu-based spacers sandwiched by two Co slabs [70, 114]. The resistivity of the alloy in a thin spacer is high, because the quantum well states are localized and do not contribute to conduction. With increasing spacer thickness the quantum well states delocalize due to electron scattering into other \mathbf{k}_{\parallel} states and begin to contribute to electron transport. The degree of agreement shown in Fig. 6.3 indicates

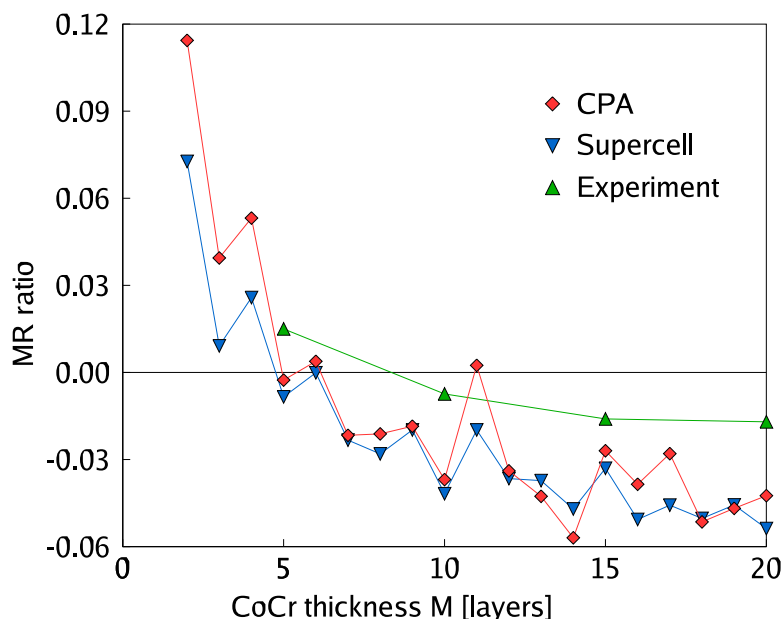


Figure 6.4: MR-ratio for fcc(111) trilayers M ML $\text{Co}_{0.8}\text{Cr}_{0.2}|20$ ML Cu|2 ML Co sandwiched by two Cu leads calculated by the present CPA approach [14] and the SC technique of Ref. [115] as functions of the CoCr slab thickness M . The experimental values of Ref. [105] refer to $\text{Co}_{0.8}\text{Cr}_{0.2}|\text{Cu}|\text{Co}|\text{Cu}$ multilayers.

that the localized nature of the quantum-well states does not represent a principal obstacle for applicability of the CPA.

6.4 CoCr | Cu | Co trilayers exhibiting negative GMR

Recently, several various F1|Cu|Co|Cu fcc(111) multilayers containing a random binary ferromagnetic alloy F1 have been manufactured that exhibit a transition from a positive to negative GMR effect with increasing thickness M of the ferromagnetic alloy [105]. The negative GMR corresponds to a situation when the AP state is more conducting than the PM one. The value of M where the transition occurs is called a compensation thickness M_t . The experimental observation has been explained theoretically for $\text{Co}_{0.8}\text{Cr}_{0.2}|\text{Cu}|\text{Co}$ trilayers using the SC method [115].

6.4.1 Transport properties

Here the CPA transport calculation is compared to the SC approach [115], both for fcc(111) trilayers M ML $\text{Co}_{0.8}\text{Cr}_{0.2}|20$ ML Cu|2 ML Co, where the $\text{Co}_{0.8}\text{Cr}_{0.2}$ layer thickness covers an interval $2 \leq M \leq 20$, sandwiched by two semi-infinite Cu leads (all atoms placed on the ideal fcc Co lattice). This replaces the experimental setup of 20x repeated F1|Cu|Co|Cu

sandwiched by Nb leads, which is impossible to compute using standard *ab initio* methods without intensive approximations because of high numerical demands. The resulting MR-ratio of both techniques together with the experimental results of Ref. [105] are shown in Fig. 6.4 as functions of the CoCr thickness M . The theoretical dependences exhibit very similar features, namely small oscillations on top of slowly decreasing trends; the latter follow roughly the experimentally observed dependence. The theoretical compensation thickness M_t is around 5 ML CoCr while the experimental compensation takes place at about 8 ML. This difference can most probably be ascribed to effects of multilayer repetitions in real samples [115].

The oscillations in the calculated $\text{Co}_{0.8}\text{Cr}_{0.2}$ thickness dependence of the MR-ratio (Fig. 6.4) are due to quantum oscillations in the minority-spin conductances, as documented in Fig. 6.5 for the AP configuration. Minority conductance is regarded here as the minority one with respect to $\text{Co}_{0.8}\text{Cr}_{0.2}$. The majority-spin conductances show up a completely different thickness dependence: a faster decrease with increasing M without any sign of oscillations, see Fig. 6.5 for the PM arrangement. The decision which of these types of behavior occurs depends on the spin channel regardless of the magnetic arrangement. The different transport regimes in the two channels are reflected also by the coherent and diffusive contributions of the conductances: while the coherent part of the majority-spin conductance represents a smaller contribution, exponentially decaying with M , the coherent part of the minority-spin conductance survives throughout the whole range of M studied and it reflects a weak scattering regime inside the CoCr slab. Note the big difference between the full and coherent conductance especially for the PM majority channel, which corresponds to vertex corrections.

6.4.2 The origin of the negative GMR

In order to understand the negative GMR, one should first notice the asymmetry of the junction structure, where the AP state corresponds to opposite magnetic direction of different magnetic layers, the Co layer and the CoCr one. In the dependence of the conductance through a standalone $\text{Co}_{0.8}\text{Cr}_{0.2}$ layer (Fig. 6.6) it can be seen that the Co majority channel is the less conducting one even for the lowest thickness without any transition. This means that the transition cannot be explained in terms of the series resistor model [48]. Within this model a different sign of the interface and bulk spin anisotropy of $\text{Co}_{0.8}\text{Cr}_{0.2}$ layer was believed to cause the transition [105]. The calculated spin polarization of $\text{Co}_{0.8}\text{Cr}_{0.2}$ negative for any thickness should within the series resistor model immediately lead to a negative GMR of $\text{Co}_{0.8}\text{Cr}_{0.2}$ | Cu| Co trilayer. Realistic calculations take into account different conductances for different \mathbf{k}_{\parallel} vectors and the coherence of electron transport across pure layers, and they cannot be replaced by simplified models in this case.

The origin of the negative bulk spin polarization was identified with a ferrimagnetic spin structure of the bulk random fcc $\text{Co}_{0.8}\text{Cr}_{0.2}$ alloy, i.e. the Co and Cr magnetic moments point in opposite directions. In the density of states (Fig. 6.7) a very good matching of minority Co and Cr-projected bands is clearly visible, while a virtual bound state is formed in the Cr-projected density of states of the CoCr alloy majority electrons [115]. This state reflects a strong scattering regime leading thus to a rapid decrease of the majority-spin conductances with increasing CoCr layer thickness M .

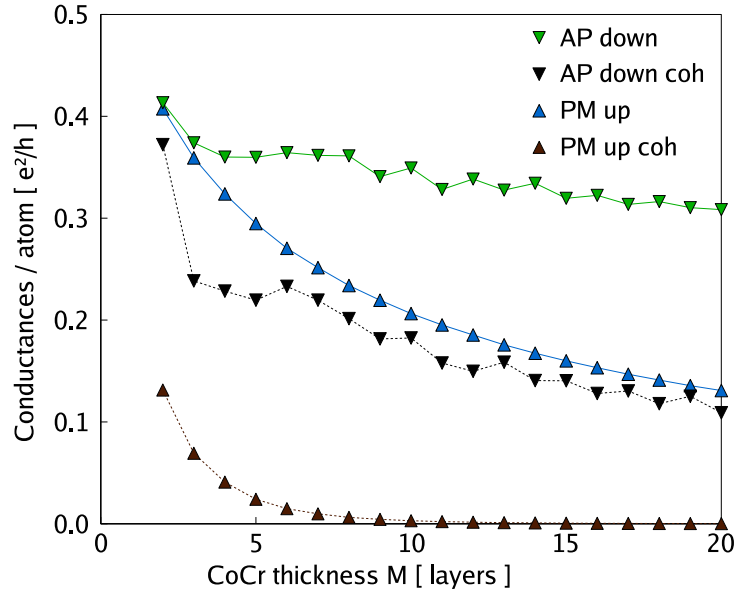


Figure 6.5: CPP conductances (solid lines) together with their coherent parts (dashed lines) of fcc(111) trilayers M ML $\text{Co}_{0.8}\text{Cr}_{0.2}|20$ ML $\text{Cu}|2$ ML Co sandwiched by two Cu leads calculated by the present CPA approach: for spin \uparrow in the PM arrangement and for spin \downarrow in the AP arrangement [14].

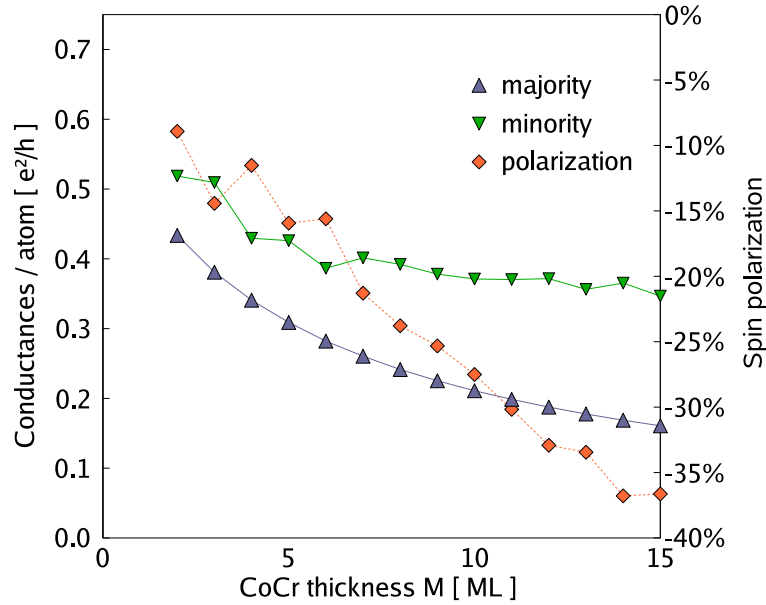


Figure 6.6: Spin-resolved CPP conductances and conductance spin polarization of fcc(111) system $\text{Cu} | M$ ML $\text{Co}_{0.8}\text{Cr}_{0.2} | \text{Cu}$ as functions of the CoCr slab thickness M .

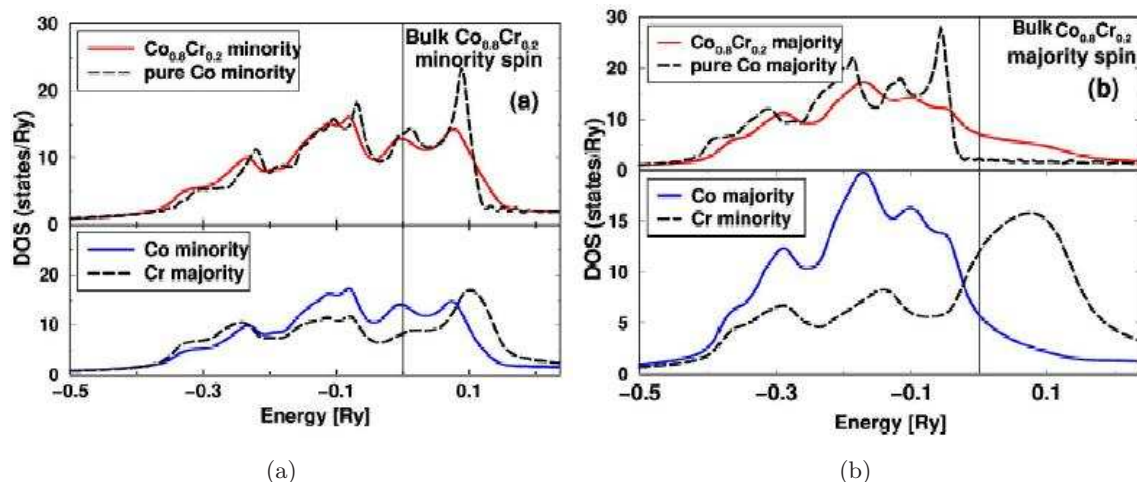


Figure 6.7: Density of states (DOS) for fcc $\text{Co}_{0.8}\text{Cr}_{0.2}$ bulk random alloy calculated in [115] employing the same ab initio scheme as used here. (a) Minority spin DOS for $\text{Co}_{0.8}\text{Cr}_{0.2}$ alloy (upper panel) and atom-resolved DOS (lower). (b) Majority spin DOS for $\text{Co}_{0.8}\text{Cr}_{0.2}$ alloy (upper panel) and atom-resolved DOS (lower). For the purpose of a comparison the DOS of a pure bulk fcc-Co is also shown. The vertical lines denote the Fermi energy.

6.4.3 The influence of interface interdiffusion

The oscillations of the MR-ratio, clearly present in theoretical results, are not seen in experiment [105]. For this reason, we investigated their sensitivity to interface roughness at the two CoCr/Cu interfaces by putting one atomic layer of composition $\text{Cu}_{1-x}\text{Co}_x$ on the Cu side of the interfaces and another one $\text{Co}_{0.8-x}\text{Cr}_{0.2}\text{Cu}_x$ on the CoCr side, where x is a concentration variable. Figure 6.8 contains the results for $x = 0.2$; very similar trends were found for other values of x in an interval $0.1 \leq x \leq 0.4$, in full analogy to the Co | Cu | Co case (Section 6.2.1). The obtained changes prove a strong influence of the interface roughness on the oscillations which brings the calculated MR-ratio towards a better agreement with the experiment and that leads us to conclusion, that the measured multilayers interfaces are annealed in a way similar to our proposal. This is another argument for the statement, that interface disorder should be taken into account in GMR calculations. An explanation of this smoothing effect rests on the fact that the Co impurities in the Cu layers represent strong scatterers for minority electrons suppressing thus the quantum conductance oscillations in this channel. Note however that the compensation length is only weakly affected by the interface roughness (Fig. 6.4 and 6.8).

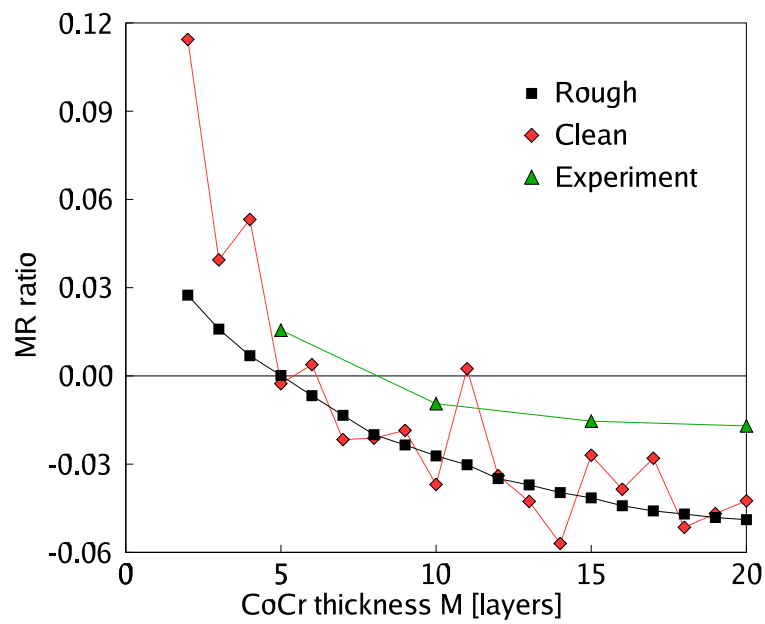


Figure 6.8: MR-ratio for fcc(111) trilayers M ML $\text{Co}_{0.8}\text{Cr}_{0.2}$ |20 ML Cu|2 ML Co sandwiched by two Cu leads calculated with clean and rough CoCr/Cu interfaces and compared to experimental values of Ref. [105].

Chapter 7

(Ga,Mn)As thin layers

The successful doping of GaAs with Mn has been realized for the first time in 1996 by H. Ohno [116], giving rise to (Ga,Mn)As, an important representative of the diluted magnetic semiconductors (DMS). The III-V DMS like, e.g., Mn-doped GaAs, GaN, and InAs with Mn atoms substituting the cations, represent nowadays the most frequently studied DMS systems [25]. The first III-V DMS (In,Mn)As was grown by molecular beam epitaxy in 1989 [117], subsequently the same group discovered hole-mediated ferromagnetism in this compound [118]. Holes are introduced into the system by the replacement of Ga or In by Mn and the hole-mediated ferromagnetism attracts ongoing interest [119]. The change in parent semiconductor caused by doping can be understood as a kind of the metal-insulator transition [68].

General feature of these systems is the random distribution of a small concentration of transition metal atoms as for example Mn on the cation sublattice. Due to the small concentrations these systems behave structurally as semiconductors and can be easily grown on their corresponding parent substrate, i.e. (Ga,Mn)As on GaAs. Moreover they can be doped and manipulated as semiconductors and they are half-metals[119–123], which both offers a large prospect for applications. However a problem of these DMS systems is that their Curie temperatures are well below room temperature because of their main property, the low concentration of magnetic atoms. This is the major obstacle for applications, hence a strong effort is targeted towards its resolution, and new representatives of DMS or already known ones prepared in other ways are currently exhibiting still higher, although yet insufficient Curie temperatures.

DMS represent system with a complicated interplay of various physical phenomena [25]. Some of its properties appear to be described or explained satisfactorily only by *ab initio* calculations. The detailed theory including, e.g., magnetic interactions and Curie temperature evaluation [124], the role of effects of *spin-orbit coupling*, remains far beyond the scope of this work. Here we concentrate mainly on its zero temperature transport properties and on an inclusion of properties that can influence it. Thin layers of (Ga,Mn)As or similar material may provide features useful for many spintronics applications. High spin polarization of electron transport is a crucial property for these applications.

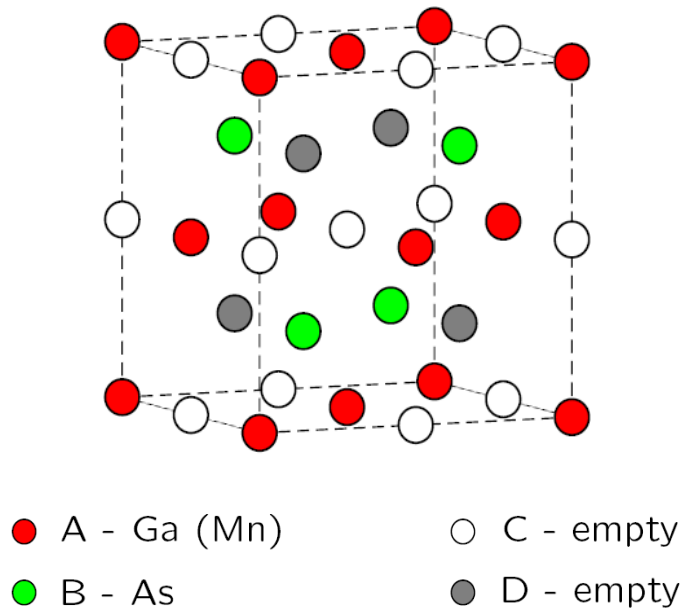


Figure 7.1: (Ga,Mn)As structure

7.1 Bulk (Ga,Mn)As

In order to explore thin layer properties, it is desirable to first understand its bulk counterpart complex behavior. Existing theoretical studies include first-principles calculations of the exchange interactions and the Curie temperatures [123–126]. The theoretical studies of transport properties of these systems, on the other hand, remain confined to a model level [127, 128]. It has been shown in a recent experiment [129] that controlled annealing of thin (Ga,Mn)As films accompanied by monitoring the resistivity during growth can lead to high Curie temperatures of the films. Moreover, a pronounced correlation between the Curie temperatures and the conductivities of the real samples has been reported [129].

The structure of (Ga,Mn)As is shown in Fig. 7.1. In the presented calculations, empty spheres in tetrahedral interstitial positions of the zinc-blende lattice were employed for reasons of a good space filling and equal Wigner-Seitz radii for all atoms and empty spheres were used. The valence basis comprised s -, p -, and d -type orbitals, where the Ga 3d orbitals were put into the core, which improves the calculation estimate of the band gap width (1.3 eV) and the valence-band width (6.8 eV). The Mn atoms were placed randomly on the cation sublattice. Electronic structure calculations reveal a band gap on the Fermi level in the minority DOS (Fig. 7.2), thus the system acts as an half-metal: an insulator for minority spin electrons and a metal for majority ones.

Bulk transport properties were in detail examined by TB-LMTO and CPA methods in [130]. Residual resistivities as functions of Mn-content x are depicted in Fig. 7.3. Their calculated values for a typical Mn-content $x = 5\%$ lie in the range $1 - 5 \times 10^{-5} \Omega\text{m}$ (see below), in good agreement with experiment [129, 131]. Note that the vertex part of the

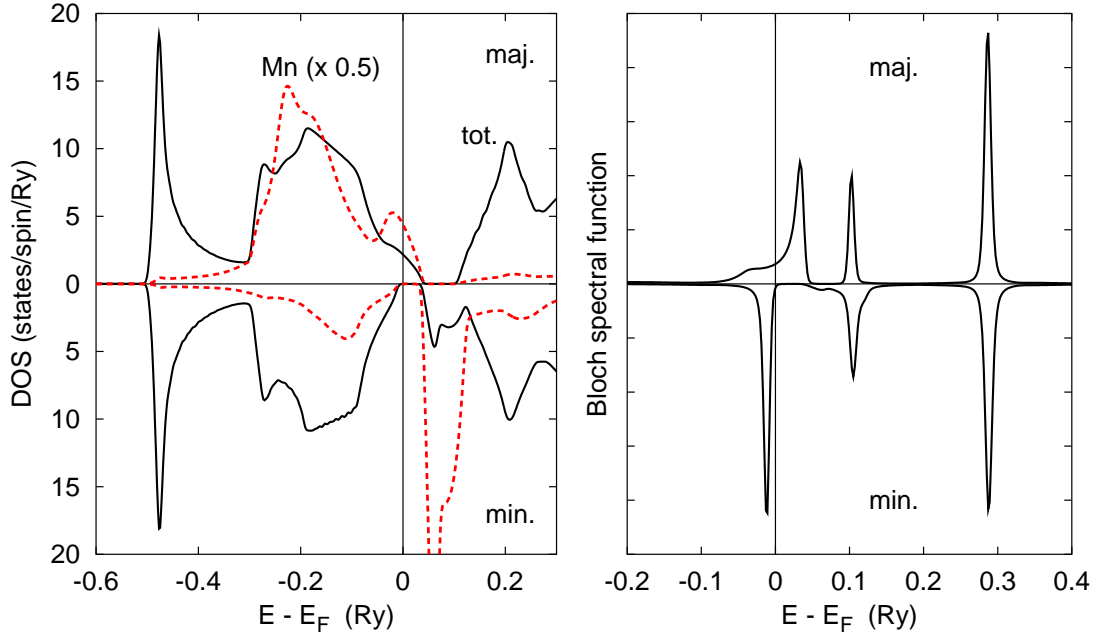


Figure 7.2: (Ga,Mn)As: density of states with highlighted local DOS on Mn atom, and the Bloch spectral function at the Γ point.

conductivity is very small in this case. We observe the decrease of the resistivity with concentration of Mn-impurities, which is just an opposite dependence to that known for metallic alloys. The reason for such behavior is a competition of two trends in the DMS's:

- (i) the increase of ρ with increasing concentration of defects which is due to impurity scattering, and
- (ii) the increase of the conductivity, i.e., the decrease of ρ , with increasing number of carriers which is in turn proportional to the concentration of Mn atoms.

The second effect is obviously dominant in the examined range of Mn concentration. Such a strong dependence on the number of carriers is missing in typical metallic alloys with a large number of carriers at the Fermi energy only weakly depending on the alloy composition. In agreement with the prediction from the density of states, the minority spin component of conductance is zero.

7.1.1 Lattice defects

Real samples of (Ga, Mn)As tend to contain lattice defects, namely As antisites on the Ga sublattice (As_{Ga} , concentration y) and Mn interstitials (Mn_i , concentration z), both act as double donors [122]. These defects reduce the Curie temperature [123] and influence a number of ground-state properties including the lattice parameter [132]. This fact can also be used to estimate the actual amount of lattice defects from X-ray lattice parameter measurements. DFT calculations [132] have shown that the lattice constant dependence on impurity concentrations can be approximated as linear (Fig. 7.4), dependences on each

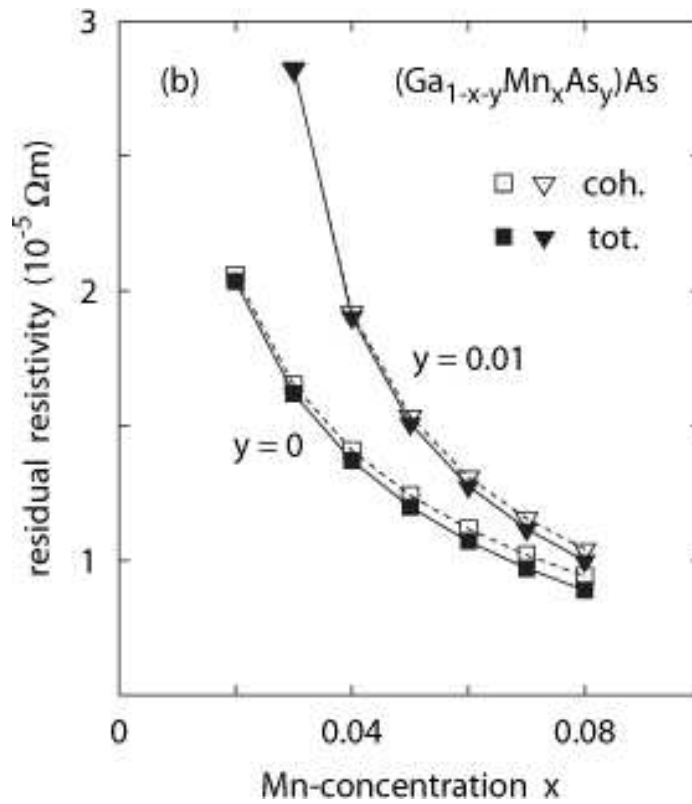


Figure 7.3: Residual resistivity of the $(\text{Ga}_{1-x-y}\text{Mn}_x\text{As}_y)\text{As}$ alloy as a function of the Mn-content [130]: without As-antisites ($y = 0$, squares) and with 1% As-antisites ($y = 0.01$, triangles). The open and full symbols refer to the coherent and the total conductivities, respectively.

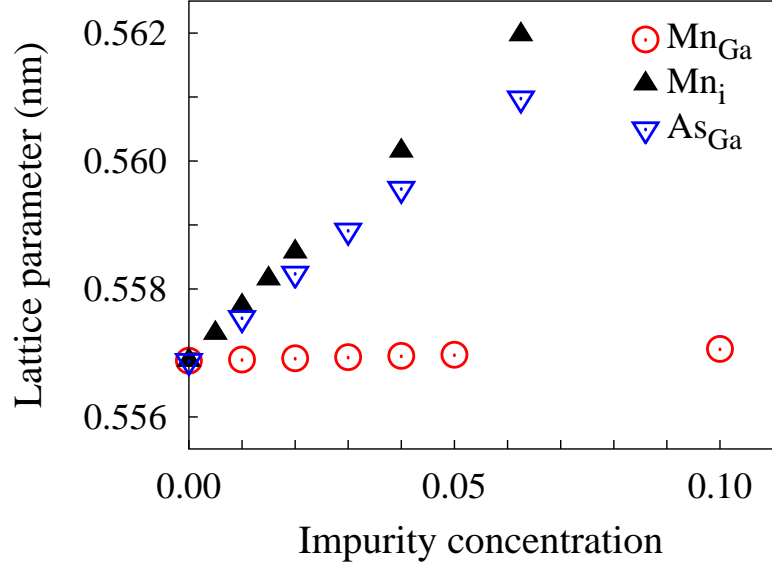


Figure 7.4: Calculated lattice constant as a function of the concentration of the impurities [132]: (a) Mn atoms in the substitutional positions (circles), (b) Mn atoms in the interstitial positions (full triangles), (c) As antisite defects (empty triangles).

separate impurity concentration can be combined into a single formula

$$a(x, y, z) = a_0 + 0.02x + 0.69y + 1.05z \text{ (\AA)}. \quad (7.1)$$

Note that the coefficient at the desirable substitutional Mn concentration (x) is more than order of magnitude smaller than that at the defect concentrations (y, z). Experimental lattice constant measurements [131] show that lattice constant grows significantly with increasing Mn content and comparisons of experimental data to the formula (7.1) leads to the conclusion that lattice defects must be present in available samples. Another possible structural defect is segregation into related compounds. As antisites have a stabilizing effect, which prevents segregation and also incorporation of Mn into interstitial positions. These effects are not studied here, we refer the reader to Ref. [133].

Important question is the magnetic orientation of interstitial Mn with respect to substitutional one. First let us note that Mnⁱ prefers to be in interstitial position corresponding to sphere C in Fig. 7.1 [133]. Density of states of $(\text{Ga}_{0.95+z}\text{Mn}_{0.05-z})\text{AsMn}_z^i$ alloy with both FM and AFM oriented Mnⁱ is shown in Fig. 7.5. Note the peak of local DOS on Mn atom at the Fermi energy in FM case, which suggests that this state is energetically less favorable. Energetic comparisons of these two states corroborate this conclusion [130, 133]. From this it also follows that system prefers to remain in halfmetallic state even for quite high amount of defects, because $(\text{Ga}_{0.95+z}\text{Mn}_{0.05-z})\text{AsMn}_z^i$ in AFM arrangement still contains a gap in the minority band at the Fermi energy. As impurities in $(\text{Ga},\text{Mn})\text{As}$ cause mainly a shift of E_F towards the top of the majority spin valence band [123] and half-metallic character is also retained in this case.

Residual resistivities as functions of the As-antisite concentration y and the Mn-interstitial

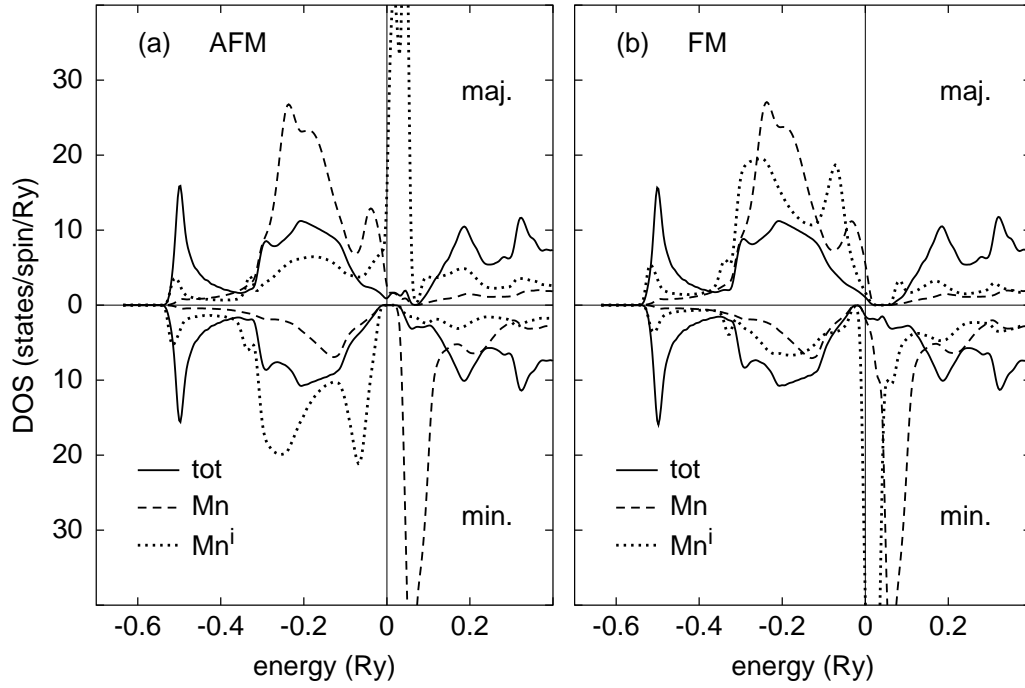


Figure 7.5: Spin-resolved total densities of states (full lines) and local Mn-densities of states on substitutional (Mn, dashed lines) and interstitial (Mn^i , dotted lines) atoms for the $(\text{Ga}_{0.95+z}\text{Mn}_{0.05-z})\text{AsMn}^i$ alloy at the compensated composition ($z = 0.0166\dots$) with antiferromagnetic (a) and ferromagnetic (b) alignment of the substitutional and interstitial Mn-moments [130]. The energy zero coincides with the Fermi level.

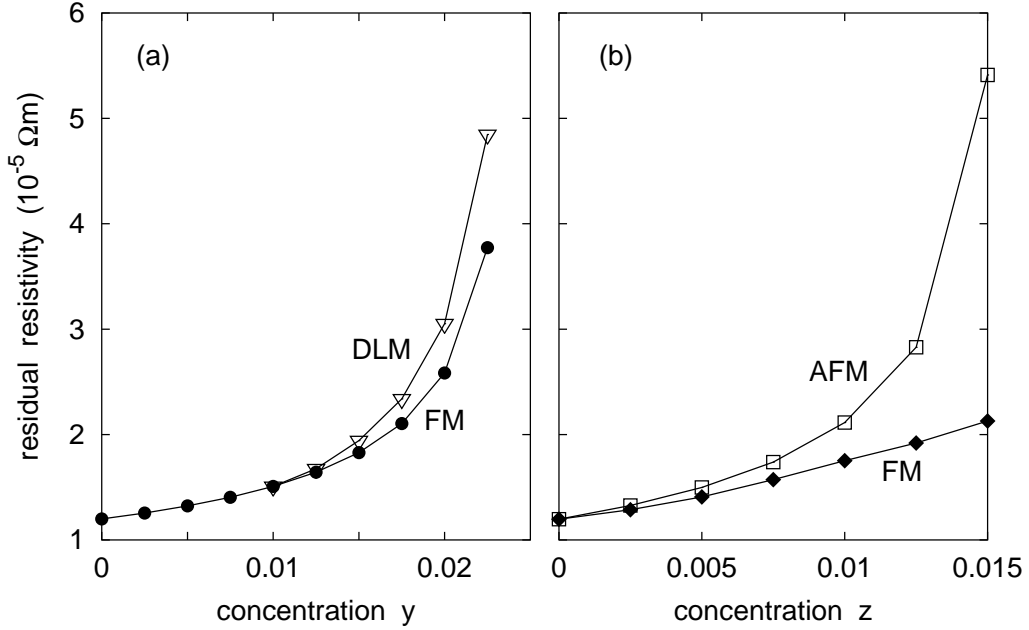


Figure 7.6: Residual resistivity of (Ga,Mn)As alloys with native structural defects [130]: (a) as a function of the As-antisite concentration y in the $(\text{Ga}_{0.95-y}\text{Mn}_{0.05}\text{As}_y)\text{As}$ alloy for the ferromagnetic state (FM, full circles) and for a disordered-local-moment state (DLM, open triangles); (b) as a function of the Mn-interstitial concentration z in the $(\text{Ga}_{0.95+z}\text{Mn}_{0.05-z})\text{AsMn}_z^i$ alloy for the antiferromagnetic (AFM, open squares) and ferromagnetic (FM, full diamonds) alignment of magnetic moments on the substitutional and interstitial Mn atoms.

concentration z are depicted in Fig. 7.6 for (Ga,Mn)As alloy with 5% Mn. The resistivity monotonically increases with defect concentrations y and z . While this looks like a conventional metallic behavior due to impurity scattering, simultaneously with disorder increase the number of carriers is reduced (both As_{Ga} and Mn^i acts as donors) and this is the dominant effect [130]. For high enough concentration of double donors ($y \rightarrow 0.025$), all holes are removed. This is the compensation limit and resistivity diverges.

The resistivity increases with the Mn-interstitial content z for both FM and AFM states; however, the two dependences differ from each other. In particular, the resistivity in the AFM case quickly increases if we approach the fully compensated state ($z \rightarrow 0.0166\dots$), this is similar to the dependence on As antisites. On the contrary, the resistivity for the rather improbable FM state increases with z nearly linearly in the whole concentration range studied. One can understand such difference from the corresponding densities of states (Fig. 7.5) for z close to the compensation limit. The large resistivity in AFM state is due to the Fermi level lying in the energy region of strongly disordered Mn-interstitial states formed in the majority band gap. On the contrary, E_F for the FM case lies in the minority conduction band (Fig. 7.5), and both majority and minority carriers contribute to the conductivity, so that the resistivity is smaller as compared to the AFM case.

7.1.2 Uncompensated DLM state

Recent theoretical studies indicate that magnetic structures with partial disorder of local magnetic moments (pDLM) can lower the total energy of system with lattice defects as compared to the ferromagnetic state [134]. This structure can be described as an alloy comprising two oppositely oriented Mn atoms: $(\text{Ga}_{1-x-y}\text{Mn}_{(1+r)x/2}^+\text{Mn}_{(1-r)x/2}^-\text{As}_y)\text{As}$, where r is an auxiliary order parameter ($0 \leq r \leq 1$) which specifies the fraction of Mn atoms with local moments oriented oppositely to the remaining Mn-moments. The concentrations of Mn^+ and Mn^- atoms are x_+ and x_- respectively. The order parameter is defined as $r = (x_+ - x_-)/x$, therefore $x_{\pm} = (1 \pm r)x/2$. Magnetic moments are not completely disordered unless $r = 0$, the system retains a nonzero average magnetic moment lower than that of its FM phase, this case is also called uncompensated DLM state.

In ref. [134] it is shown that for a situation without As antisites the oppositely oriented Mn^- moments would form a very narrow impurity band located exactly at the Fermi level, which is energetically very unfavorable situation and forces Mn moments to the FM state. However the enough amount of extra electrons donated by As antisites cause the impurity subband of Mn^- to lay completely below the Fermi level thus being energetically inexpensive. The shift of E_F therefore contributes to energetic stabilization of the DLM state as well as to the full spin polarization of the DLM conductivities. *Ab initio* calculations can evaluate the energy associated with each amount of magnetic disorder (parameter r), depicted in Fig. 7.7. Thus they reveal the threshold value of As antisites concentration y leading to partial DLM (Fig. 7.8 for various Mn-content x) and determine the order parameter associated with each y .

The presence of additional disorder of course increases the amount of scattering, its influence on the residual resistivity can be seen in Fig. 7.6. Calculations of conductance shows that the transport remains completely spin polarized up to quite high values of antisite disorder, in agreement with the finding that Mn^- states (potentially destroying the full spin polarization) are located mainly below the Fermi level. Their contribution to spin polarization is negligible up to $y \leq 0.02$ (and $x = 0.05$), for higher values the corresponding strong magnetic disorder ($r > 0.3$) starts to influence the DOS heavily [135].

7.2 Ideal (Ga,Mn)As layers coupled to metallic leads

The interesting influence of (Ga,Mn)As on conductance spin polarization can be utilized in systems where it is comprised in a form of layers with nanoscale thickness. A tunneling junction comprising two such layers has already been prepared [136], yielding an impressive TMR of 290% at 0.39K. Here we examine properties of its basic elements, single thin (Ga,Mn)As slabs, which may provide important information for construction of arbitrary *spintronics* devices based on it.

The calculations reported here were performed for (001) layers of zinc-blende $\text{Ga}_{1-x}\text{Mn}_x\text{As}$ alloys with Mn content in a range $0.03 \leq x \leq 0.10$, sandwiched by two semi-infinite bcc(001) leads of nonmagnetic chromium. The lattice (Ga,Mn)As is equivalent to four inpenetrating fcc lattices as described in sec. 7.1. These two different lattices allow quite precise matching, where the lattice constant $a_{bcc} = \sqrt{2}a_{fcc}$. One atomic (001) layer of the resulting bcc lattice thus contained two spheres: either a Ga sphere and an empty sphere or an As sphere

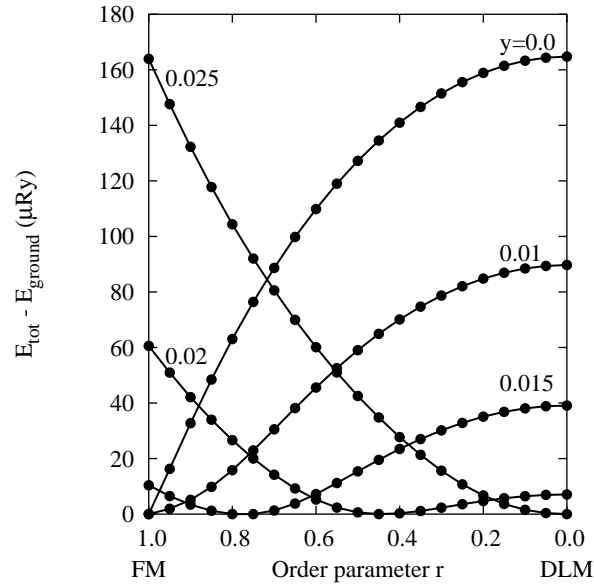


Figure 7.7: The energy difference $E_{tot} - E_{ground}$ for (Ga,Mn)As in pDLM state with various As antisite concentrations y and a fixed Mn-content $x = 0.05$ [124] as a function of the order parameter r .

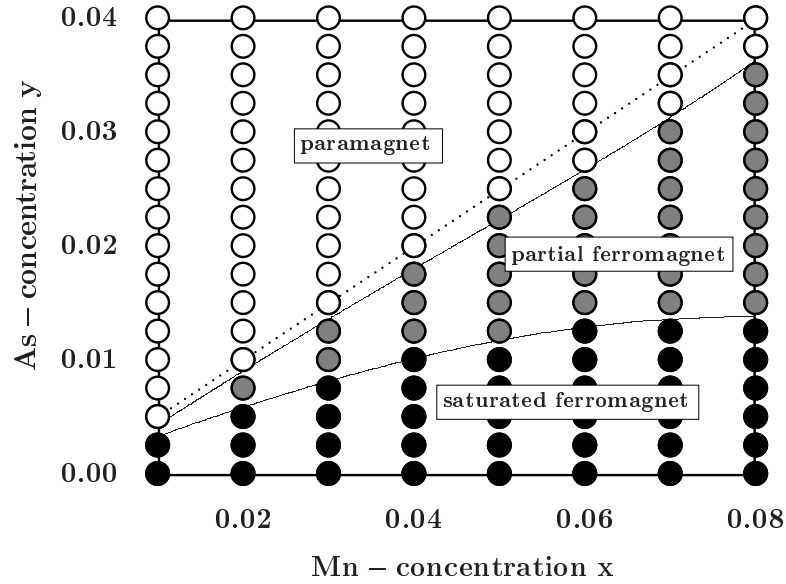


Figure 7.8: The three phases in the magnetic phase diagram of $(\text{Ga}_{1-x-y}\text{Mn}_{(1+r)x/2}^+\text{Mn}_{(1-r)x/2}^-\text{As}_y)\text{As}$. The dashed line separates n- and p- type samples.

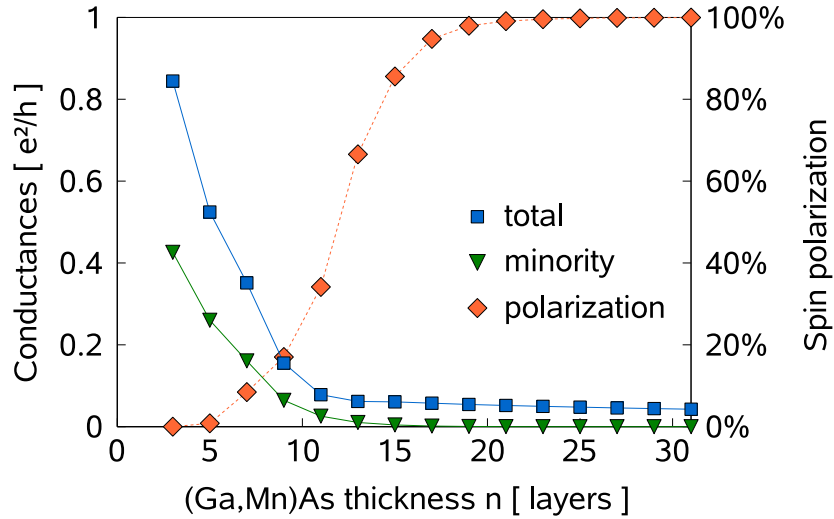


Figure 7.9: CPP conductances and the spin polarization of $(\text{Ga}_{0.95}\text{Mn}_{0.05})\text{As}$ (001) slabs sandwiched by two semi-infinite nonmagnetic bcc Cr(001) leads as functions of its thickness n [137].

and an empty sphere inside the $(\text{Ga},\text{Mn})\text{As}$ slab, or two Cr spheres inside the Cr leads; all spheres have equal radii. This kind of layer will here be referred to as a monolayer (ML) or simply layer, but always only units of principal layers are added to or removed from the system, these contain both Ga and As spheres in the $(\text{Ga},\text{Mn})\text{As}$ part and are twice as thick as ML. No relaxations of an ideal bcc lattice were allowed; its lattice parameter was set according to the equilibrium fcc lattice of pure GaAs ($a = 0.565$ nm) which required a small compression ($\sim 2\%$) inside the Cr leads as compared to an equilibrium bcc Cr lattice. The $(\text{Ga},\text{Mn})\text{As}$ slabs comprised an odd number n of atomic layers, where $3 \leq n \leq 31$ and their description was similar to the bulk case; the slabs were As-terminated with no disorder at the As/Cr interfaces. 4-6 ML of Cr were used on each side to allow the model to achieve self-consistency. Transport calculations were performed on a uniform mesh of 3600 \mathbf{k}_{\parallel} points in the 2D BZ.

The calculated total and spin-resolved CPP conductances for slabs with 5% Mn are depicted in Fig. 7.9. Their thickness dependence exhibits two different slopes: a rapid decrease for thin layers ($n < 11$) followed by a much slower decrease for thick layers ($n > 11$). The transition between these two regimes can be explained by the formation of the bulk-like electronic structure in the middle of thicker $(\text{Ga},\text{Mn})\text{As}$ slabs; it can also be observed in the behavior of local electronic quantities as illustrated in Fig. 7.10 for the local spin Mn moments in the central plane of the slabs with 5% Mn. The central Mn moments in thin slabs are strongly influenced by the leads while a slow monotonous trend towards the bulk value is found only for thicker slabs. The decreasing influence of the Cr leads on the CPP conductances (Fig. 7.9) is also reflected by a strong spin polarization due to the exponentially decaying minority conductance C^{\downarrow} for $n > 11$, while the majority one C^{\uparrow} is

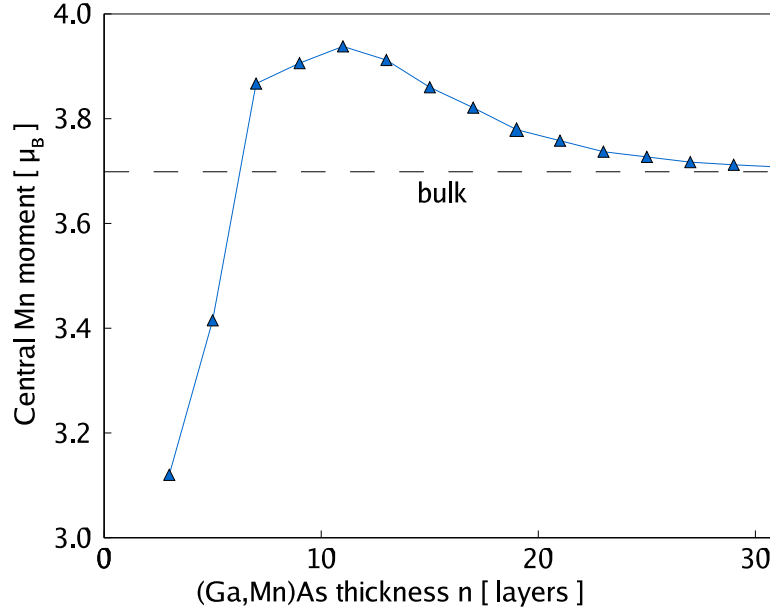


Figure 7.10: The local magnetic moment of Mn atoms in the middle of (Ga,Mn)As (001) slabs with 5% Mn sandwiched by two semi-infinite nonmagnetic bcc Cr(001) leads as a function of the slab thickness [14]. The horizontal line marks the Mn moment in the bulk $\text{Ga}_{0.95}\text{Mn}_{0.05}\text{As}$ alloy.

approaching an ohmic regime. Both these features are expected because of the half-metallic nature of bulk (Ga,Mn)As alloys [119, 121–123]. It is interesting to see how thick DMS layer is required to reach a relatively high polarization of the current. Note that higher values of the spin polarization within our model have to be taken with care due to the neglected effects of *spin orbit coupling*.

In the limit of high slab thickness the derivative of the total CPP resistance with respect to the disordered slab thickness is in good agreement with the resistivity obtained from bulk calculations [130] and with experimental data [129], their comparison is provided in Tab. 7.1. The experimental values for $x = 0.05$ and $x = 0.06$ provide an independent check of reliability of the *ab initio* CPA scheme whereas the markedly higher resistivity measured for $x = 0.08$ reflects a high amount of compensating As antisite defects in the sample [129].

The coherent and vertex contributions to the majority conductance are shown in Fig. 7.11 for $(\text{Ga}_{0.92}\text{Mn}_{0.08})\text{As}$ (001) slabs. The former decreases rapidly with (Ga,Mn)As thickness and it vanishes practically for $n > 10$ whereas the latter does not change appreciably over the range of n studied. These trends witness that the intrinsic disorder of (Ga,Mn)As slabs is strong enough to destroy the coherence after a very short distance traveled by electrons. This conclusion is in qualitative agreement with effects of strong disorder (*non-quasiparticle behavior*) manifested in the Bloch spectral function of majority electrons at the Fermi level of the bulk alloy [138]. Note that the decomposition to coherent and vertex contributions is completely different from its bulk counterpart, but their sums agree well as was shown

Table 7.1: Residual resistivities (in $10^{-5} \Omega\text{m}$) of $\text{Ga}_{1-x}\text{Mn}_x\text{As}$ as obtained from the CPP conductances (ρ_{CPP}) of thick (Ga,Mn)As(001) slabs sandwiched by two nonmagnetic bcc(001) Cr leads [137] and from bulk calculations (ρ_{bulk}) of Ref. [130]. The experimental values (ρ_{exp}) are taken from Ref. [129].

Mn content x	ρ_{CPP}	ρ_{bulk}	ρ_{exp}
0.05	1.23 ± 0.04	1.20	1.49
0.06	1.06 ± 0.02	1.07	1.32
0.08	0.88 ± 0.01	0.89	2.87

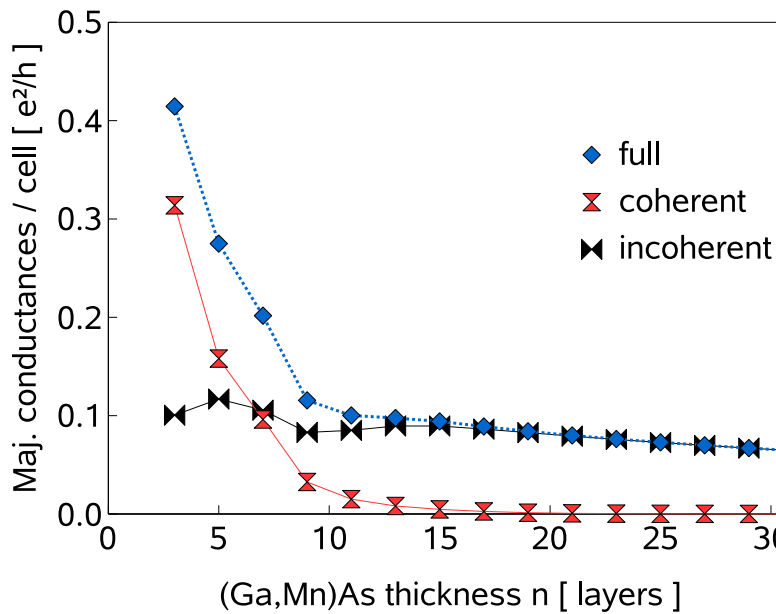


Figure 7.11: Majority-spin CPP conductance and its coherent and vertex part for $(\text{Ga}_{0.92}\text{Mn}_{0.08})\text{As}$ (001) slabs sandwiched by two semi-infinite nonmagnetic bcc Cr(001) leads as functions of its thickness n [14].

in the preceding paragraph. In the bulk case vertex corrections can almost be neglected, while in the layered one they play a dominant role.

Thin (Ga,Mn)As layers represent also a very interesting system from the point of view of spin torque related phenomena. An extensive discussion of spin-mixing conductance of this system and a graph of the spin-mixing conductance as a function of slab thickness (Fig. 4.5) can be seen in Sec. 4.6.

Increasing Mn concentration raises the majority (and total) conductance (Fig. 7.12), which proves an importance of the number of carriers (holes in the valence band) in addition to the strength of impurity scattering and is consistent with calculations of bulk (Ga,Mn)As.

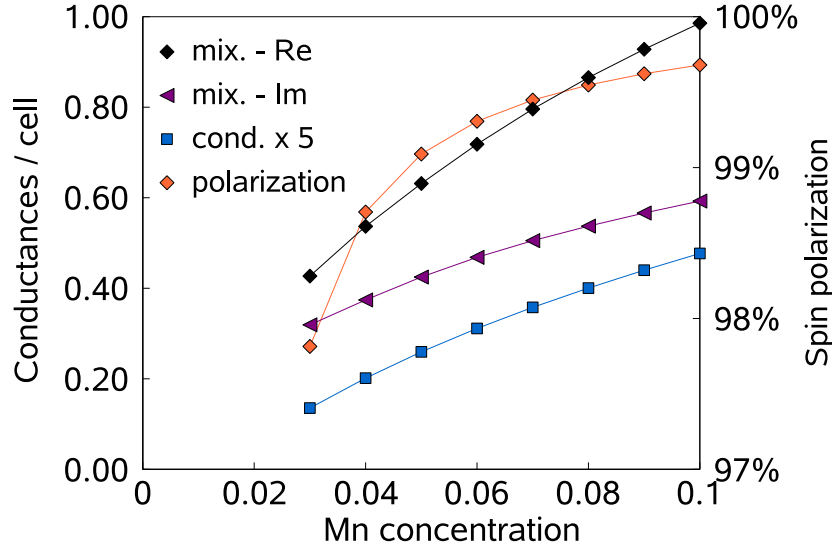


Figure 7.12: Total CPP conductance, its spin polarization and the real and imaginary parts of the mixing conductance for thin $(\text{Ga}_{1-x}\text{Mn}_x)\text{As}$ (001) slab of thickness $t = 21$ atomic layers as functions of Mn concentration x . Results for charge conductance were published in [137].

Also the minority states penetrating to $(\text{Ga}, \text{Mn})\text{As}$ from metallic leads become more quickly suppressed, which results in an increase of the conductance spin polarization P . The behavior of mixing conductances is analyzed in Sec. 4.6.

7.3 (Ga,Mn)As layers with lattice defects

The total resistance as a function of defect concentration exhibits trends similar to the one observed for bulk (Fig. 7.13). Bulk $(\text{Ga}, \text{Mn})\text{As}$ with As antisites of concentration below full compensation remains half-metallic. For the layered geometry, layers deep inside $(\text{Ga}, \text{Mn})\text{As}$ have the same property. However, the metal induced gap states (MIGS) and their spatial extent change, and this influences the spin polarization of the conductance. The majority conductance is decreasing with increasing amount of defects as expected, but the minority one rises, which leads to a decrease of the spin polarization (Fig. 7.13). This contrasts the constant full spin polarization of the bulk conductivities.

Fig. 7.14 shows the spin polarization of the layer-resolved density of states (DOS) at the Fermi energy (E_F) for thin $(\text{Ga}, \text{Mn})\text{As}$ slabs. With increasing amount of As antisites MIGS penetrate deeper into slabs, which explains the rise of minority conductance [137]. When the slab thickness is enlarged, the tunneling part deep inside it will dominate the transport, and the minority conductance will again be exponentially decaying with the slab thickness (Fig. 7.15). This finding also supports the described explanation based on changes of DOS at the interfaces.

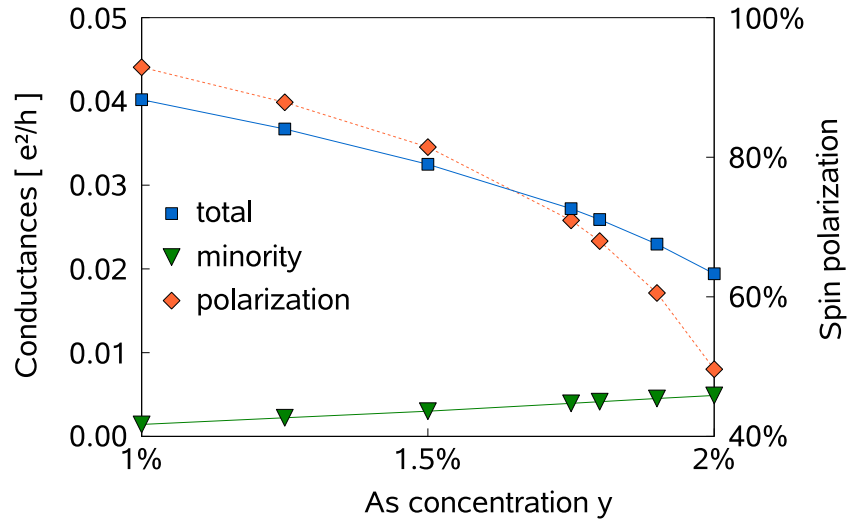


Figure 7.13: CPP conductances and the spin polarization for thin $(\text{Ga}_{0.95-y}\text{Mn}_{0.05}\text{As}_y)\text{As}$ (001) slab of thickness $n = 21$ atomic layers as functions of As antisite concentration y [137].

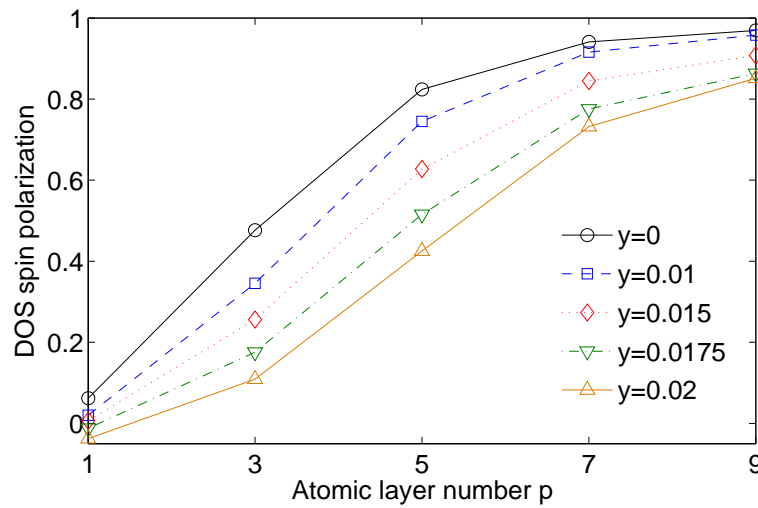


Figure 7.14: Spin polarization of layer-resolved DOS at E_F for monolayers m inside $(\text{Ga}_{0.95-y}\text{Mn}_{0.05}\text{As}_y)\text{As}$ (001) slabs of thickness $n = 21$ monolayers, where $m = 1$ is adjacent to one of Cr leads [137]. Each m and $m + 1$ correspond to one elementary cell and its DOS is summed.

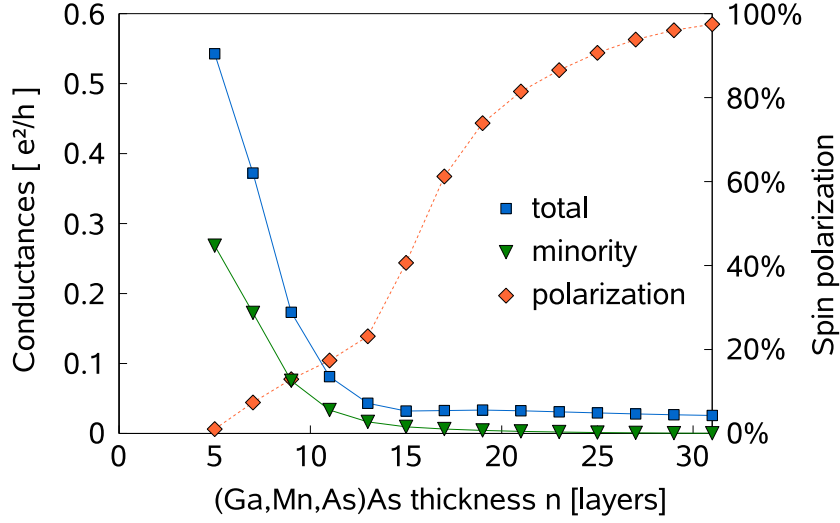


Figure 7.15: CPP conductances and the spin polarization for thin $(\text{Ga}_{0.935}\text{Mn}_{0.05}\text{As}_{0.015})\text{As}$ (001) slab as functions of its thickness [137].

The influence of the Mn interstitials on the CPP conductances for $(\text{Ga,Mn})\text{As}$ slabs with 5% Mn and the thickness of 21 ML is summarized in Fig. 7.16. Similarly to the case of the As antisites (Fig. 7.13) and to the bulk behavior (Fig. 7.6), the total conductances decrease with increasing Mn-interstitial content z ; the decrease becomes more pronounced for the AFM state [135]. The polarization of the CPP conductances decreases with z as well; the reduction of P is especially strong for the FM state and higher contents of Mn interstitials (Fig. 7.16).

7.3.1 Uncompensated DLM state

The presence of the uncompensated DLM state reduces significantly the conductivity of bulk $(\text{Ga,Mn})\text{As}$. It also impacts the spin polarization of transport, but only in the case of a very high magnetic disorder. Very similar trends (Fig. 7.17) can be observed for thin $(\text{Ga,Mn})\text{As}$ layers [135].

In calculations whose results are depicted in Fig. 7.17 order parameter r across the whole thin slab was assumed to be the same as for bulk $(\text{Ga,Mn})\text{As}$ with the same concentration of impurities. However a new partial DLM state characterized by r has to be found for thin layers and its value is generally layer-dependent, we denote it r_m . Order parameter is reasonably defined only for monolayers m containing Ga(Mn) spheres, therefore only those even numbered. The discovery of partial DLM state is performed as a search for a set of values r_m minimizing the total energy and it is significantly more complicated than for bulk systems.

We perform an iterative energy minimization with respect to r_m with a simplifying assumption on the energy dependence on r_m : we assume that there are no local minima of E in the $(n-1)/2$ -dimensional space of possible r_m values. First order parameter \hat{r}^{min}

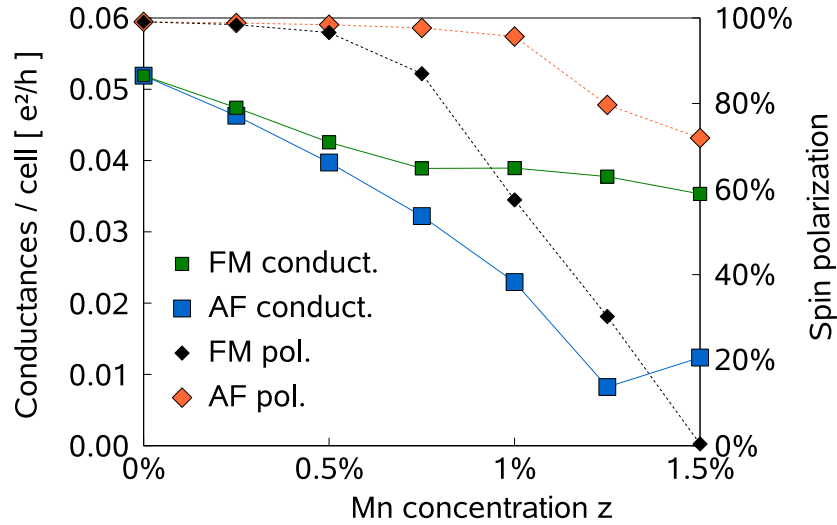


Figure 7.16: The total CPP conductances of the $(\text{Ga}_{0.95+z}\text{Mn}_{0.05-z})\text{AsMn}_z^i$ (001) slabs with a fixed thickness of 21 ML and the spin polarization of these conductances as functions of the Mn-interstitial concentration z in the ferromagnetic state (FM) and in the antiferromagnetic state (AFM) [135].

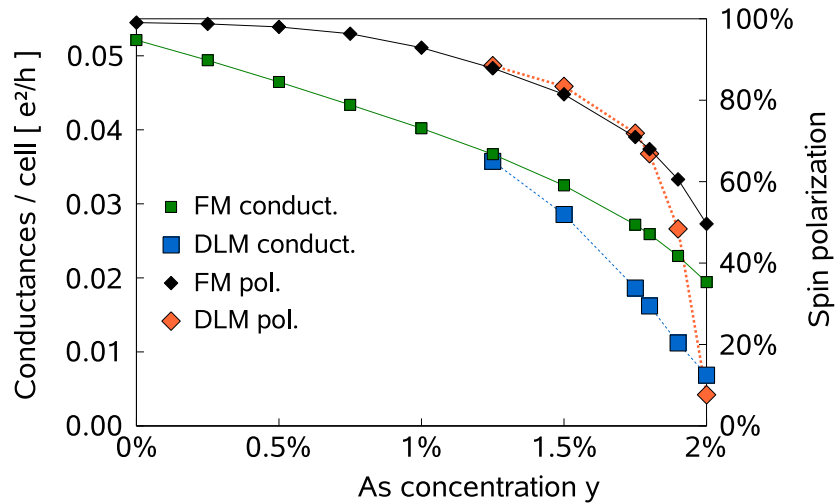


Figure 7.17: The total CPP conductances of the $(\text{Ga}_{0.95-y}\text{Mn}_{0.05}\text{As}_y)\text{As}$ (001) slabs with a fixed thickness of 21 ML sandwiched by two semi-infinite nonmagnetic bcc Cr(001) leads and the spin polarization of these conductances as functions of the As-antisite concentration y in the ferromagnetic state (FM) and in a disordered-local-moment state (DLM) [135].

homogeneous across the slab minimizing the total energy E is found, then r_m corresponding to monolayers $m = 2..n - 1$ are varied from this \hat{r}^{min} in sequence to find their values r_m^{min} minimizing E , previously obtained r_m^{min} are always put into system instead of \hat{r}^{min} so that the surrounding monolayers ($m' \neq m$) of examined m is simultaneously updated. The loop starts with those m adjacent to interfaces and continues inwards, when the reached r_m^{min} is close to \hat{r}^{min} it varies r_m for m in the direction from middle monolayers towards interfaces until all m are examined. The mirror symmetry of the slab with respect to the central layer is employed to reduce the number of steps. The whole iteration is then repeated and if there are no changes of r_m^{min} for all m due to updated surrounding, the iterative process is finished.

The obtained distribution of substitutional Mn^+ and Mn^- atoms is depicted in Fig. 7.18 for $(\text{Ga}_{0.94}\text{Mn}_{x_+}^+\text{Mn}_{x_-}^-\text{As}_{0.01})\text{As}$ (001) slabs of thickness $t = 21$ with $x = x_+ + x_- = 0.05$. For this combination of concentrations x, y the bulk (Ga,Mn)As remains completely ferromagnetic, but for thin layers we see a clear formation of a strong magnetic disorder penetrating deep into the slab ($r_m = 0.3$ for $m = 4..8$ and vice versa on the opposite side of the slab), and the interface Mn atoms are even oriented opposite to the slab magnetization.

For the FM arrangement of Mn atoms the corresponding CPP conductance spin polarization of the $(\text{Ga}_{0.94}\text{Mn}_{x_+}^+\text{Mn}_{x_-}^-\text{As}_{0.01})\text{As}$ (001) slabs is 93%. In its more realistic magnetic state described by the calculated order parameter (Fig. 7.18) the polarization is reduced to 79%, and the total conductance is 0.63 times smaller. We estimate that for higher defect concentrations, which correspond to a presence of slight pDLM even in bulk, the magnetic disorder in thin slabs will be much higher and the spin polarization would be completely destroyed sooner than it is shown in Fig. 7.17. However, note that the presented results for thin layers are also strongly sensitive to the material of leads and to the thickness of DMS slabs.

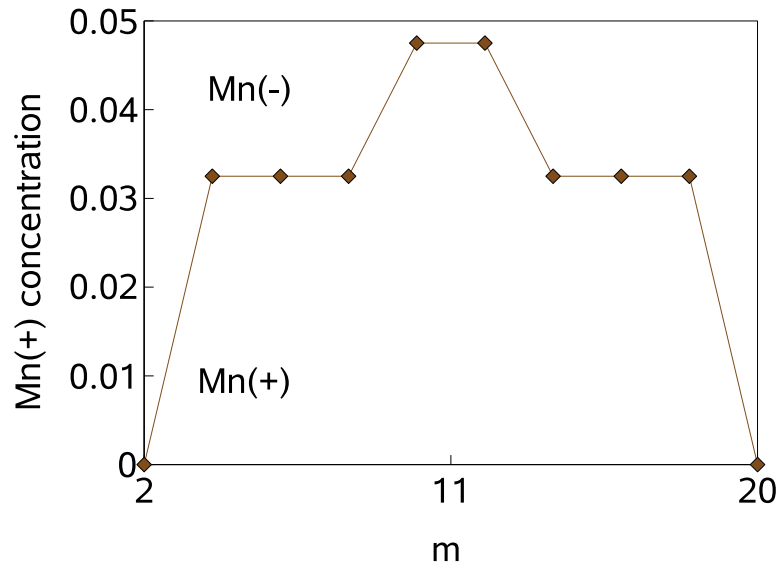


Figure 7.18: Distribution of total Mn concentration between Mn^+ and Mn^- atoms for monolayers m inside $(\text{Ga}_{0.94}\text{Mn}_{x_+}^+\text{Mn}_{x_-}^-\text{As}_{0.01})\text{As}$ (001) slabs of thickness $n = 21$ atomic layers with $x = x_+ + x_- = 0.05$. Mn atoms are located at even numbered layers m and $m = 2, 20$ are locations adjacent to one of Cr leads. Terminating As atoms are at $m = 1, 21$. Each m and $m + 1$ correspond to one principal layer.

Chapter 8

Co₂MnSi thin layers

The intermetallic compound Co₂MnSi is chosen here as a representative of the wide class of full Heusler alloys. This name originates from Friedrich Heusler's discovery of ferromagnetic alloy Cu₂MnAl, whose all elements are non-magnetic. Later the name was adopted for all intermetallic compounds with similar structure and the first discovered half-metal belongs to this class [24]. It can be viewed as 4 inpenetrating fcc lattices (Fig. 8.1) with lattice parameter ($a = 0.565$ nm) very close to that of GaAs, which allows very good matching to it.

Halfmetallicity is common among Heusler alloys, and Co₂MnSi also should have this property according to *ab initio* calculations [139]. However, attempts to prove this experimentally were not successful until recently, when the halfmetallic energy gap in Co₂MnSi was observed by tunneling conductance spectroscopy [140, 141]. There are few most probable reasons for difficulties with confirming halfmetallicity of this structure [142]:

- The used methods are often surface sensitive, but the half-metallic character is destroyed at surfaces.
- Antisite disorder is likely to occur, especially swapping between Mn atoms and similar sized Co atoms, which are also close to each other

One of the most important advantages of Co₂MnSi over other halfmetals is its high Curie temperature 985K, magnon effects can be neglected even at room temperature [143]. Another crucial feature is the expected width of the minority bandgap, which should preserve the half-metallicity even at room temperature (depending on the position of the Fermi energy inside the gap). Therefore this material is definitely worth further examination.

8.1 Bulk properties

The calculated band structure and density of states of ideal Co₂MnSi are depicted in Fig. 8.2 and the left panel of Fig. 8.3, respectively. Transport calculations show zero conductance in the minority spin channel as expected because of its predicted half-metallic character. Calculated magnetic moment is $5 \mu_B$ per f. u. (formula unit), in agreement with the fact that conduction band is cut by Fermi level for one spin channel only, hence there

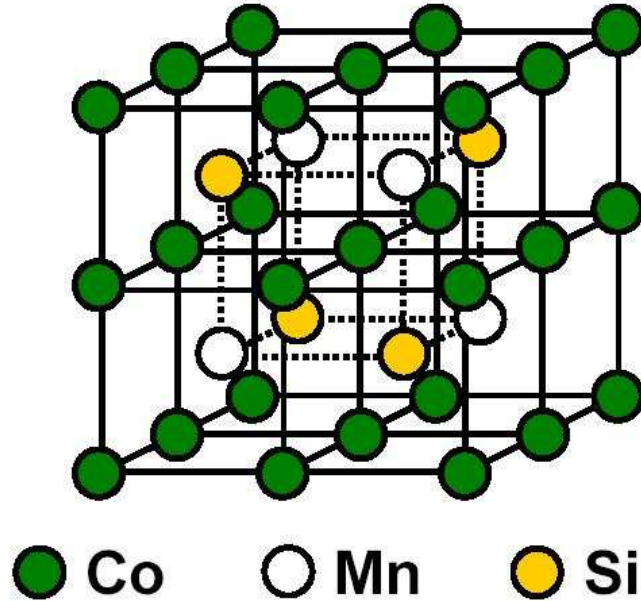


Figure 8.1: Co_2MnSi structure, four time the formula unit volume displayed [142].

must be an integer number of electrons per f. u. present in both spin directions. SQUID based measurements of samples without special disorder reduction have yielded a value of $4.78 \mu_B$ [144], which is another proof of lower quality of these common samples and supports the idea of antisite disorder. We have investigated $(\text{Co}_{1-y/2}\text{Mn}_{y/2})_2(\text{Mn}_{1-y}\text{Co}_y)\text{Si}$ with swapping between Co and Mn in the range of up to $y=20\%$ Co as antisites on the Mn sublattice (Fig. 8.4). The range of magnetic moments of these alloys obtained from *ab initio* calculations comprise also the experimental value of magnetic moment, it can be matched to $y=8\%$. X-ray measurements [145] (on different samples) have shown a similar $y=7\%$, which corroborates that disorder of these really not negligible values can be expected in samples without a special treatment to improve quality. This amount of disorder corresponds to the conductance spin polarization of 98.5% (Fig. 8.4). The calculated density of states shows that the Co impurity band (on the Mn sublattice) is formed in the minority channel close to the Fermi energy (see Fig. 8.3, right panel). The halfmetallicity is in fact destroyed, but a conductance through such a virtual bound state remains strongly suppressed. Hence the conductance spin polarization is still high, but the non-negligible number of states near E_F in the minority channel may significantly impact the spin polarization measurements.

Recently a special annealing method was utilized in order to remove antisite disorder [140]. The minority spin energy gap was successfully observed [141] by tunneling conductance spectroscopy, the measured width of the gap (350 - 400 meV) and separation between the Fermi energy and the bottom edge of conduction band (10-20 meV) agree apparently well with *ab initio* electronic structure calculations of ideal Co_2MnSi (Fig. 8.3, band gap

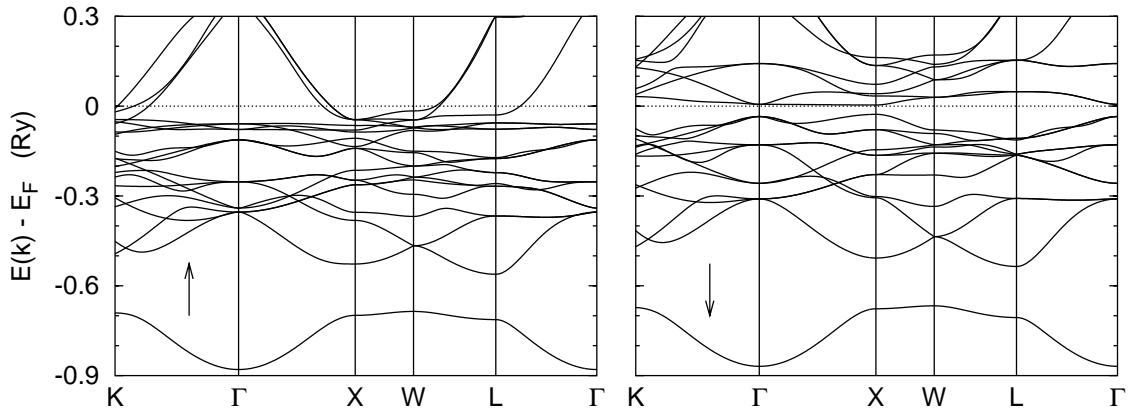


Figure 8.2: Band structure of the full-Heusler compound Co_2MnSi in the spin- \uparrow (left panel) and the spin- \downarrow channel (right panel).

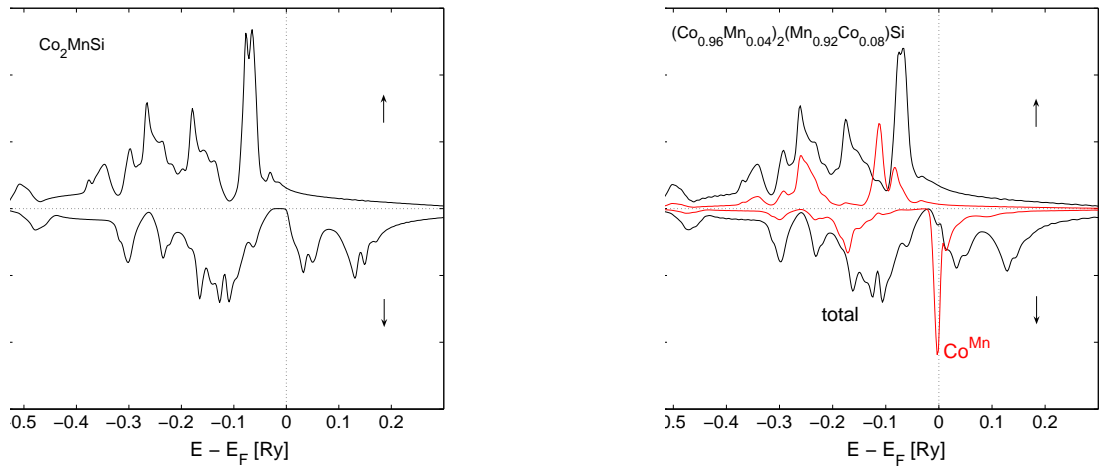


Figure 8.3: Density of states of ideal ($y = 0$, left panel) and disordered ($y = 0.08$, right panel) bulk $(\text{Co}_{1-y/2}\text{Mn}_{y/2})_2(\text{Mn}_{1-y}\text{Co}_y)\text{Si}$.

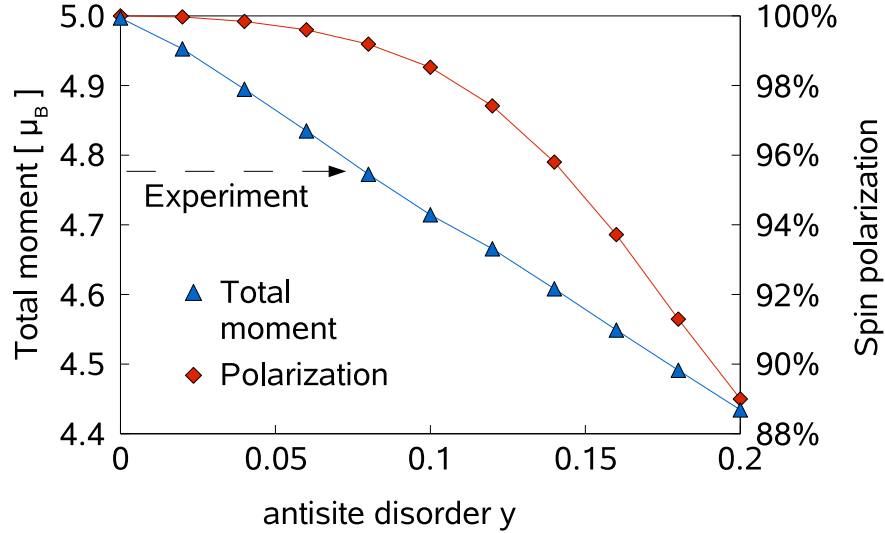


Figure 8.4: Total Mn moment and conductance spin polarization in disordered bulk $(\text{Co}_{1-y/2}\text{Mn}_{y/2})_2(\text{Mn}_{1-y}\text{Co}_y)\text{Si}$ as functions of antisite disorder y .

width 430 meV). To prepare half-metallic Co_2MnSi is thus within the reach of current technology.

8.2 Thin layers

Thin layers of Co_2MnSi were examined as sandwiched by bcc Cr(001) leads. Lattice matching of Cr and Co_2MnSi and the used techniques are similar to the case of Cr and (Ga,Mn)As, see Sec. 7.2. The Cr lattice was slightly compressed by cca. 2% to fit the equilibrium lattice of Co_2MnSi . One atomic (001) layer inside the Co_2MnSi slabs contained either two Co atoms or a Ga sphere and an As sphere, these two layers together form a principal layer. The slabs comprised an even number of atomic layers n , where $4 \leq n \leq 30$, they were thus terminated by a Co atomic layer on one side (\mathcal{L}) of the junction and by a layer containing Mn, Si on the other side (\mathcal{R}). Transport calculations were performed on a uniform mesh of 3600 \mathbf{k}_{\parallel} points in the 2D BZ. The CPP conductance and its spin polarization for ideal slabs is depicted in Fig. 8.5, the transport is purely ballistic, hence the conductance is oscillating around a constant value which reflects mainly the interface mismatch between Cr and Co_2MnSi and Cr Sharvin resistance. The minority conductance is suppressed even more quickly than in the (Ga,Mn)As based junctions (Sec. 7.2), which obviously leads to a quick saturation of conductance spin polarization.

Thin layers with antisite disorder should provide better agreement with real experiments. CPP conductances and the electronic structure for $y = 8\%$ corresponding to the expected disorder were calculated (Fig. 8.6). Note that while for bulk this disorder led to relatively very small reduction of the spin polarization (100% \rightarrow 98.5%), CPP conductance

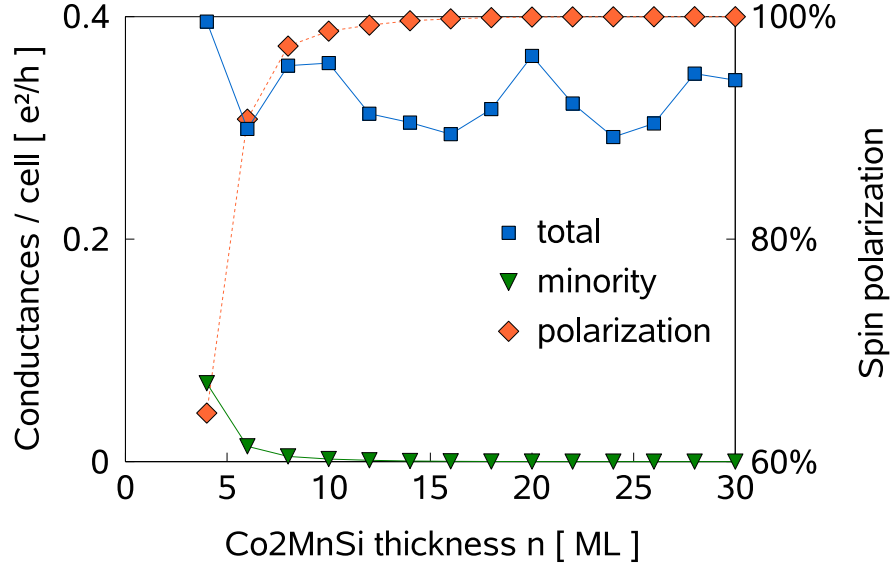


Figure 8.5: CPP conductances C , C^\downarrow and the spin polarization of Co_2MnSi (001) slabs sandwiched by two semi-infinite nonmagnetic bcc $\text{Cr}(001)$ leads as functions of its thickness n .

polarization of the thin layer remains at significantly lower value even for the thickness of 24 monolayers. This thickness was enough to yield 99.99% polarization for pure thin layers, but for $(\text{Co}_{0.96}\text{Mn}_{0.04})_2(\text{Mn}_{0.92}\text{Co}_{0.08})\text{Si}$ it is reduced to 90.2%. The minority conductance now has apparent ohmic behavior for larger thickness, which supports the previously presented idea based on the analysis of the DOS (Fig. 8.3, right panel) that for disordered Co_2MnSi this conductance is reduced mainly due to strong scattering and not tunneling.

Spin-mixing conductances of half-metallic materials may have some specific features, therefore we calculated the dependence of this quantity on slab thickness for both ideal and disordered Co_2MnSi (Fig. 8.7). The mixing conductance reaches its almost maximum value immediately for layers of thickness 5 ML because of its high exchange splitting, which is in good agreement with the statements in Sec. 4.6. Similar to $(\text{Ga},\text{Mn})\text{As}$ case any oscillations are hardly observable. The imaginary part of $C_{\mathcal{L}}^{mix}$ is also exceptionally high with respect to the real part, an explanation of this phenomena based on a free-electron model was provided in [16]. Properties of spin-mixing conductances of both $(\text{Ga},\text{Mn})\text{As}$ and Co_2MnSi are surprisingly similar, the main difference is the fact that $\text{Re } C_{\mathcal{L}}^{mix}$ is almost an order of magnitude lower than the lead Sharvin conductance for $(\text{Ga},\text{Mn})\text{As}$, while for Co_2MnSi it is reduced only slightly (Tab. 4.1). It is interesting to see that the spin-mixing conductance is only very slightly reduced due to disorder and oscillations are additionally smeared out in the presence of it.

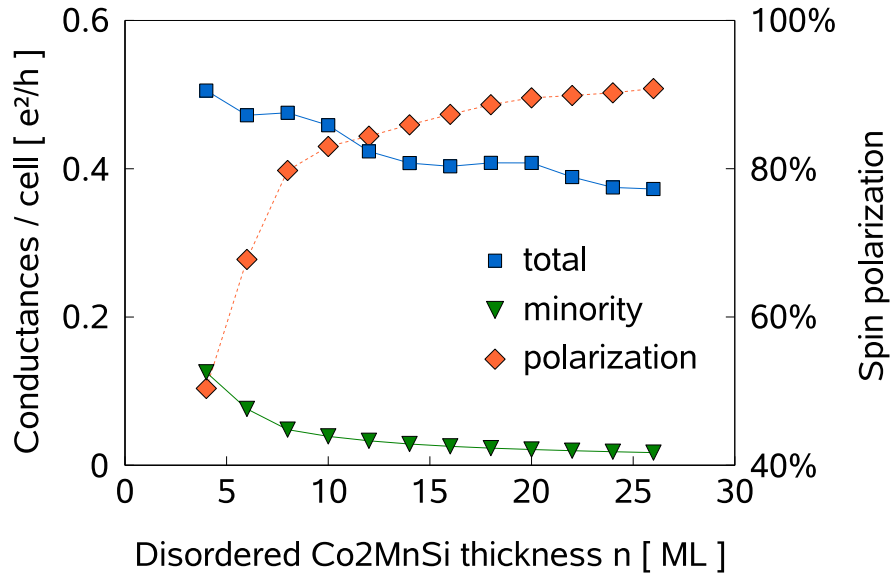


Figure 8.6: CPP conductances C , C^\downarrow and the spin polarization of $(\text{Co}_{0.96}, \text{Mn}_{0.04})_2 (\text{Mn}_{0.92}, \text{Co}_{0.08}) \text{Si}$ (001) slabs sandwiched by two semi-infinite non-magnetic bcc Cr(001) leads as functions of its thickness n .

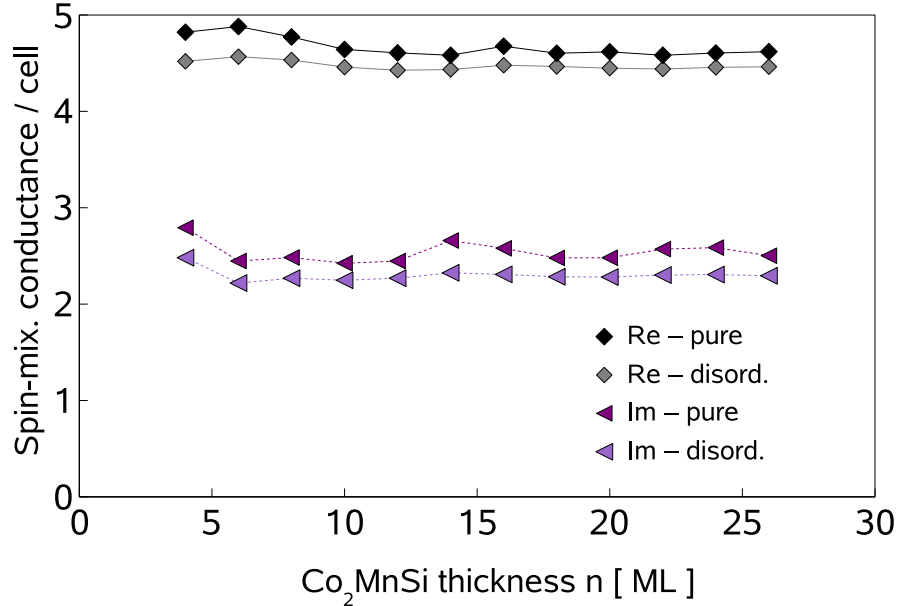


Figure 8.7: Spin-mixing conductances $C_{\mathcal{L}}^{mix}$ of both Co_2MnSi (001) and $(\text{Co}_{0.96}, \text{Mn}_{0.04})_2 (\text{Mn}_{0.92}, \text{Co}_{0.08}) \text{Si}$ (001) slabs sandwiched by two semi-infinite non-magnetic bcc Cr(001) leads as functions of its thickness n .

8.3 Spin valves

The uniquely high spin polarization of Co_2MnSi encourages its use in spin valves as ideal spin filters. Such a device should exhibit extraordinary high magnetoresistance ratio and also very high spin torques on FM layers (Chap. 4) should be present. Experimental realization of such a device should avoid the problem of surface sensitivity of some polarization measurements and give better information about the realized spin polarization and how well does it compare to the theoretical predictions. An experimental measurement of tunneling junction $\text{Co}_2\text{MnSi} | \text{AlO}_x | \text{Co}_{0.7}\text{Fe}_{0.3}$ gave TMR ratio 86% at 10K, from which a spin polarization 61% was deduced [142] based on Julliere's formula (Eq. 2.38). In work [146] a tunneling junction $\text{Co}_2\text{MnSi} | \text{MgO} | \text{Co}_{0.5}\text{Fe}_{0.5}$ was investigated and provided quite high TMR 70% at room temperature and 169% at 4.2 K. A very similar result was obtained for amorphous Al-O spacer [147]. Their similarity suggests that transport properties do not depend for this system strongly on spacer properties, in contrast to recent findings about Fe | MgO | Fe junctions [4]. Upon the improved annealing which removed antisite disorder, $\text{Co}_2\text{MnSi} | \text{AlO}_x | \text{Co}_2\text{MnSi}$ samples recently exhibited an extraordinary TMR ratio of 570% at 2K [140]. For similarly developed $\text{Co}_2\text{MnSi} | \text{AlO}_x | \text{Co}_{0.75}\text{Fe}_{0.25}$ the TMR 159% was obtained [141].

We have calculated ideal spin valves Cr | 12ML Co_2MnSi | 8ML Cr | 12ML Co_2MnSi | Cr (001). The MR ratio of pure layers is over $10^5\%$ as can be expected for halfmetallic junction, with antisite disorder $y = 8\%$ it is reduced to 320%. This indicates that antisite disorder can explain the difference between values obtained in different measurements, but only more experimental data could eliminate other explanations.

Another interesting topic is the possible non-collinear setup of magnetic layers and associated spin-torques (Chap. 5) in non-collinear Cr | 12 Co_2MnSi | 8 Cr | 12 Co_2MnSi | Cr (001) spin valves. We have investigated dependences of CPP resistances and spin torques on FM layers relative angles ϑ (Fig. 8.8). Both curves show features of a typical half-metal. In formulas (5.32, 5.33) coefficients χ and ω have high values and multiply the terms supporting asymmetry of the result and shift the torque maximum towards the AP oriented end of graph, which is seen in Fig. 8.8.

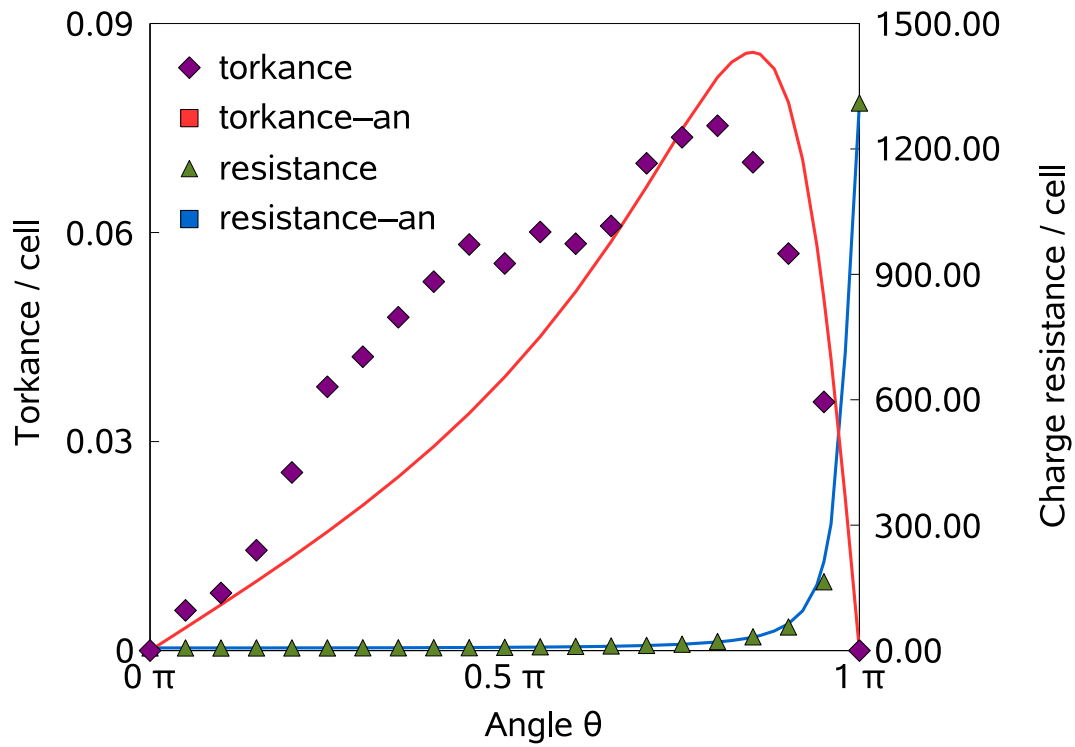


Figure 8.8: CPP resistances and the spin torque exerted on the second FM layer of the Cr | 12ML Co_2MnSi | 8ML Cr | 12ML Co_2MnSi | Cr bilayer as functions of FM layers relative angle ϑ from ab initio calculations (markers) compared to empirical formula results (lines)

Chapter 9

Conclusions

The theoretical part of this work was aimed mainly towards a development of very general *ab initio* methods. First we have enlarged the range of materials that can be handled by existing approaches: transport properties calculations for disordered systems based on the CPA were extended from bulk materials also to systems with one reduced dimension, multilayers. We have shown the importance of vertex corrections for this particular situation. This kind of problems can be evaluated on *ab initio* level also by means of the supercell method, but for some materials or situations our method appears to be more suitable, for example for the diluted magnetic semiconductors. Comparison of the supercell and the full CPA results proves that important aspects of the spin-polarized CPP transport are fully within the reach of an effective medium treatment (Sec. 6.2.2, 6.3).

Secondly we have derived *ab initio* methods for evaluation of novel observables connected with the phenomena of *current induced magnetization switching*, namely the spin-mixing conductance and spin torque. This area is yet only scarcely examined and we believe that our work has contributed significantly to understanding of this phenomenon, we have for example revealed its connection to system Green's functions (Eqs. 4.19, 4.20, 4.21). For the first time the spin-mixing conductance was combined with the CPA approximation for disordered systems. We have also demonstrated the equivalence between the Kubo and NEGF approach within linear response regime for one particular direction of spin-mixing conductance. The key features of our technique are the correct inclusion of evanescent states and the fact that it can be treated in a similar way as the charge conductance, thus it is compatible with the previously mentioned method for disordered systems. This general formulation of mixing conductances allows to find whether some often adopted assumptions are correct in all situations. Namely the assumption of a fast convergence of spin-mixing conductance with increasing thickness is found not to be valid for thin Ni layers (Fig. 4.3). Imaginary part of the mixing conductance was believed to be much smaller than the real part, this was disproven here for thin layers of (Ga,Mn)As (Fig. 4.5) or Co₂MnSi (Tab. 4.1, Fig. 8.7). A compact Caroli-like formula was formulated for spin torque caused by CPP current in non-collinear magnetic layered systems (Eq. 5.23). The relation between spin-mixing conductances and spin torques in non-collinear magnetic junctions has been found to be quite close (Sec. 5.3) and the theory has been shown to be capable of dealing with arbitrary angular arrangements of magnetic layers (Sec. 5.4.1). In the future this approach to non-collinear systems can be combined with the CPA too and the *spin-orbit*

coupling may also be included with no major obstacles.

The second part containing informations about concrete materials served two purposes. First it was used to test the presented methods. The systems were therefore selected so that they were as diverse as possible. Its results were compared to experimental data or other computational results if available, and the agreement was generally within the expected accuracy. Predictions for observable and material combination without relevant previous information were tested successfully for symmetries and conditions it should fulfill and at least the trends were found appropriate to what can be expected according to material properties. Therefore the developed methods appear to have passed the tests, and the chosen approximations were appropriate. The second main purpose was to find more information about the selected systems, explain not yet understood phenomena and predict its behavior under yet untested conditions, therefore we attempted to choose primarily physically interesting systems with unique or novel features or systems with a high application potential.

For thin (Ga,Mn)As layers many presented findings are novel since almost all existing *ab initio* studies deal only with its bulk counterpart. The obtained transport properties has therefore been checked for compatibility with calculated and measured bulk data, which turned out to be successful (Tab. 7.1). Very interesting is the discovered relation between the current spin polarization and native structural defects (Sec. 7.3). We have provided an explanation of this dependence based on the variation of metal induced gap states. We were also the first to calculate the spin-mixing conductance of this system and some results are rather surprising, especially the already mentioned magnitude of its imaginary part. Although we do not believe that the Curie temperature of (Ga,Mn)As can be raised high enough to allow practical utilization of this material, the same ideas can be more or less applied to other diluted magnetic semiconductors. In this class of materials there are some other promising novel types which may overcome the Curie temperature problem, in this context Li(Zn,Mn)As has been proposed recently [148].

Interest in Heusler alloys is high because of its unique features. An obstacle for obtaining theoretically predicted features in Co_2MnSi is its high tendency to antisite disorder, which leads quickly to a loss of halfmetallicity, we have calculated its impact on transport properties of thin Co_2MnSi layers (Sec. 8.2). Its direct elimination did not appear to be easily doable, but very recent experiments seems to have overcome this problem[140]. Our results may help to understand how the expected total spin polarization can be reached. We examined the angular dependence of spin torque (Fig. 8.8) exerted on one part of a spin valve constructed from such almost ideal spin-filter, this may be very important for attempts to create CIMS based applications of this or a similar material.

Appendix A

Derivation of Kubo formula for generalized CPP transport

The starting formula (2.47) can be rewritten using Eq. (2.5):

$$C_{A\tilde{B}} = \frac{i}{2\pi} \lim_{\alpha \rightarrow 0^+} \int d\xi f(\xi) \text{Tr} \left\{ [G(\xi + i0) - G(\xi - i0)] A G(\xi + i\alpha) \tilde{B} \right. \\ \left. + G(\xi - i\alpha) A [G(\xi + i0) - G(\xi - i0)] \tilde{B} \right\}. \quad (\text{A.1})$$

We decompose the last equation to three contributions distinguished by the sign of the imaginary parts of both complex energy arguments, labeled as:

- C^P ... for both imaginary parts positive
- C^N ... for both imaginary parts negative
- C^M ... for imaginary parts with mixed signs

The following commutator allows to revert the order of $G(z)$ and \tilde{B} :

$$\left[G(z), \tilde{B} \right] = G(z) \left(\tilde{B}(z - H) - (z - H) \tilde{B} \right) G(z) = -iG(z) \tilde{A}G(z).$$

From this a relation corresponding to our problem can be derived:

$$\text{Tr} \left\{ A G(z_\mu) \tilde{B} G(z_\nu) \right\} = \text{Tr} \left\{ A \tilde{B} G(z_\mu) G(z_\nu) \right\} - i \text{Tr} \left\{ A G(z_\mu) \tilde{A} G(z_\mu) G(z_\nu) \right\}, \quad (\text{A.2})$$

or alternatively

$$\text{Tr} \left\{ A G(z_\mu) \tilde{B} G(z_\nu) \right\} = \text{Tr} \left\{ A G(z_\mu) G(z_\nu) \tilde{B} \right\} + i \text{Tr} \left\{ A G(z_\mu) G(z_\nu) \tilde{A} G(z_\mu) \right\}. \quad (\text{A.3})$$

We employ (A.2) for the part of (A.1) corresponding to C^M :

$$C_1^M = \frac{i}{2\pi} \lim_{\alpha \rightarrow 0^+} \int d\xi f(\xi) \text{Tr} \left\{ A \tilde{B} G(\xi + i0) G(\xi - i\alpha) - A \tilde{B} G(\xi + i\alpha) G(\xi - i0) \right. \\ \left. - i A G(\xi + i0) \tilde{A} G(\xi + i0) G(\xi - i\alpha) + i A G(\xi + i\alpha) \tilde{A} G(\xi + i\alpha) G(\xi - i0) \right\},$$

where the involved products of two Green's functions can be rewritten by means of the Ward identity given here as:

$$G(z_\mu)G(z_\nu) = \frac{1}{z_\nu - z_\mu} [G(z_\mu) - G(z_\nu)]. \quad (\text{A.4})$$

Its use in formula for C_1^M leads to:

$$C_1^M = \frac{i}{2\pi} \lim_{\alpha \rightarrow 0^+} \int d\xi f(\xi) \text{Tr} \left\{ A\tilde{B} \frac{G(\xi + i0) - G(\xi - i\alpha)}{-i\alpha} - A\tilde{B} \frac{G(\xi + i\alpha) - G(\xi - i0)}{-i\alpha} \right. \\ \left. - iAG(\xi + i0)\tilde{A} \frac{G(\xi + i0) - G(\xi - i\alpha)}{-i\alpha} + iAG(\xi + i\alpha)\tilde{A} \frac{G(\xi + i\alpha) - G(\xi - i0)}{-i\alpha} \right\}.$$

It can be assumed that operators A, \tilde{A} are restricted only to the intermediate region as there is no need to have them defined out of it.

Since \tilde{B} in the last formula is also bounded there by multiplication by A , the limit $\alpha \rightarrow 0^+$ can be correctly performed:

$$\lim_{\alpha \rightarrow 0^+} \frac{G(\xi + i0) - G(\xi - i\alpha)}{-i\alpha} - \frac{G(\xi + i\alpha) - G(\xi - i0)}{-i\alpha} = \\ \lim_{\alpha \rightarrow 0^+} \frac{G(\xi + i\alpha) - G(\xi + i0)}{i\alpha} - \frac{G(\xi - i\alpha) - G(\xi - i0)}{-i\alpha} = G'(\xi + i0) - G'(\xi - i0).$$

This yields:

$$C_1^M = \frac{i}{2\pi} \int d\xi f(\xi) \text{Tr} \left\{ A\tilde{B} [G'(\xi + i0) - G'(\xi - i0)] \right\} \quad (\text{A.5}) \\ + \frac{i}{2\pi} \lim_{\alpha \rightarrow 0^+} \frac{1}{\alpha} \int d\xi f(\xi) \text{Tr} \left\{ AG(\xi + i0)\tilde{A}G(\xi + i0) - AG(\xi + i0)\tilde{A}G(\xi - i\alpha) \right\} \\ + \frac{i}{2\pi} \lim_{\alpha \rightarrow 0^+} \frac{1}{\alpha} \int d\xi f(\xi) \text{Tr} \left\{ AG(\xi + i\alpha)\tilde{A}G(\xi - i0) - AG(\xi + i\alpha)\tilde{A}G(\xi + i\alpha) \right\}.$$

Alternatively, (A.3) can be employed instead of (A.2) for the part of (A.1) corresponding to C^M :

$$C_2^M = \frac{i}{2\pi} \lim_{\alpha \rightarrow 0^+} \int d\xi f(\xi) \text{Tr} \left\{ AG(\xi + i0)G(\xi - i\alpha)\tilde{B} - AG(\xi + i\alpha)G(\xi - i0)\tilde{B} \right. \\ \left. + iAG(\xi + i0)G(\xi - i\alpha)\tilde{A}G(\xi - i\alpha) - iAG(\xi + i\alpha)G(\xi - i0)\tilde{A}G(\xi - i0) \right\}$$

We transform C_2^M analogously to the preceding derivation for C_1^M :

$$C_2^M = \frac{i}{2\pi} \int d\xi f(\xi) \text{Tr} \left\{ \tilde{B}A [G'(\xi + i0) - G'(\xi - i0)] \right\} \quad (\text{A.6}) \\ + \frac{i}{2\pi} \lim_{\alpha \rightarrow 0^+} \frac{1}{\alpha} \int d\xi f(\xi) \text{Tr} \left\{ AG(\xi + i\alpha)\tilde{A}G(\xi - i0) - AG(\xi - i0)\tilde{A}G(\xi - i0) \right\} \\ + \frac{i}{2\pi} \lim_{\alpha \rightarrow 0^+} \frac{1}{\alpha} \int d\xi f(\xi) \text{Tr} \left\{ AG(\xi - i\alpha)\tilde{A}G(\xi - i\alpha) - AG(\xi + i0)\tilde{A}G(\xi - i\alpha) \right\}.$$

Averaging the two expressions for C^M , Eqs. (A.5, A.6), we find

$$\begin{aligned}
C^M &= \frac{i}{4\pi} \int d\xi f(\xi) \operatorname{Tr} \left\{ (A\tilde{B} + \tilde{B}A) [G'(\xi + i0) - G'(\xi - i0)] \right\} \\
&+ \frac{1}{4\pi} \lim_{\alpha \rightarrow 0^+} \int d\xi f(\xi) \operatorname{Tr} \left\{ \frac{AG(\xi + i\alpha) \tilde{A}G(\xi + i\alpha) - AG(\xi + i0) \tilde{A}G(\xi + i0)}{i\alpha} \right\} \\
&+ \frac{1}{4\pi} \lim_{\alpha \rightarrow 0^+} \int d\xi f(\xi) \operatorname{Tr} \left\{ \frac{AG(\xi - i\alpha) \tilde{A}G(\xi - i\alpha) - AG(\xi - i0) \tilde{A}G(\xi - i0)}{-i\alpha} \right\} \\
&- \frac{1}{2\pi} \lim_{\alpha \rightarrow 0^+} \int d\xi f(\xi) \operatorname{Tr} \left\{ \frac{AG(\xi + i\alpha) \tilde{A}G(\xi - i0) - AG(\xi + i0) \tilde{A}G(\xi - i0)}{i\alpha} \right\} \\
&- \frac{1}{2\pi} \lim_{\alpha \rightarrow 0^+} \int d\xi f(\xi) \operatorname{Tr} \left\{ \frac{AG(\xi + i0) \tilde{A}G(\xi - i\alpha) - AG(\xi + i0) \tilde{A}G(\xi - i0)}{-i\alpha} \right\},
\end{aligned}$$

where limits can be replaced by derivatives:

$$\begin{aligned}
C^M &= \frac{i}{4\pi} \int d\xi f(\xi) \operatorname{Tr} \left\{ (A\tilde{B} + \tilde{B}A) [G'(\xi + i0) - G'(\xi - i0)] \right\} \\
&+ \frac{1}{4\pi} \int d\xi f(\xi) \frac{d}{d\xi} \operatorname{Tr} \left\{ AG(\xi + i0) \tilde{A}G(\xi + i0) + AG(\xi - i0) \tilde{A}G(\xi - i0) \right\} \\
&- \frac{1}{2\pi} \int d\xi f(\xi) \operatorname{Tr} \left\{ AG'(\xi + i0) \tilde{A}G(\xi - i0) + AG(\xi + i0) \tilde{A}G'(\xi - i0) \right\}.
\end{aligned}$$

Since $f(\xi) \rightarrow 0$ for $\xi \rightarrow \infty$ and $[G(\xi + i0) - G(\xi - i0)] \rightarrow 0$ for $\xi \rightarrow -\infty$, an integration by parts can be performed:

$$\begin{aligned}
C^M &= \frac{-i}{4\pi} \int d\xi f'(\xi) \operatorname{Tr} \left\{ (A\tilde{B} + \tilde{B}A) [G(\xi + i0) - G(\xi - i0)] \right\} \\
&+ \frac{1}{4\pi} \int d\xi f'(\xi) \frac{d}{d\xi} \operatorname{Tr} \left\{ A[G(\xi + i0) - G(\xi - i0)] \tilde{A}G(\xi - i0) \right. \\
&\quad \left. - AG(\xi + i0) \tilde{A}[G(\xi + i0) - G(\xi - i0)] \right\}.
\end{aligned}$$

The second term is now in the form of the desired coefficient $C_{A\tilde{B}}^{(1)}$ (Eq. 2.49), which gives rise to charge conductance.

A similar approach is used for C^P, C^N . We find the averaged formula for C^P :

$$\begin{aligned}
C^P &= \frac{i}{4\pi} \int d\xi f(\xi) \operatorname{Tr} \left\{ (A\tilde{B} + \tilde{B}A) G^2(\xi + i0) \right\} \\
&+ \frac{1}{4\pi} \int d\xi f(\xi) \operatorname{Tr} \left\{ AG(\xi + i0) \tilde{A}G^2(\xi + i0) - AG^2(\xi + i0) \tilde{A}G(\xi + i0) \right\}
\end{aligned}$$

The formula for C^N differs only by signs:

$$\begin{aligned}
C^N &= \frac{-i}{4\pi} \int d\xi f(\xi) \operatorname{Tr} \left\{ (A\tilde{B} + \tilde{B}A) G^2(\xi - i0) \right\} \\
&- \frac{1}{4\pi} \int d\xi f(\xi) \operatorname{Tr} \left\{ AG(\xi - i0) \tilde{A}G^2(\xi - i0) - AG^2(\xi - i0) \tilde{A}G(\xi - i0) \right\}
\end{aligned}$$

We sum these two contributions, for their first terms we employ the relation $G^2(z) = -G'(\xi)$ and an integration by parts, which yields:

$$\begin{aligned}
C^P + C^N &= \frac{i}{4\pi} \int d\xi f'(\xi) \text{Tr} \left\{ (A\tilde{B} + \tilde{B}A) [G(\xi + i0) - G(\xi - i0)] \right\} \\
&\quad + \frac{1}{4\pi} \int d\xi f(\xi) \text{Tr} \left\{ AG(\xi + i0) \tilde{A}G^2(\xi + i0) - AG^2(\xi + i0) \tilde{A}G(\xi + i0) \right. \\
&\quad \left. - AG(\xi - i0) \tilde{A}G^2(\xi - i0) - AG^2(\xi - i0) \tilde{A}G(\xi - i0) \right\}
\end{aligned} \tag{A.7}$$

The total response coefficient is given as

$$C_{A\tilde{B}} = C^M + C^P + C^N. \tag{A.8}$$

The first terms of C^M and $C^P + C^N$ cancel each other in (A.8). Note that the remaining part of C^M is equivalent to $C_{A\tilde{B}}^{(1)}$, formula (2.49), while the remaining part of $C^P + C^N$, the second term in Eq. (A.7), is equivalent to $C_{A\tilde{B}}^{(R)}$, formula (2.50), and the validity of Eq. (2.48) has been proven. This proof does not require an existence of an operator B which fulfills $A = -i[B, H]$.

Appendix B

Invariance property of the spin-mixing conductance

Let us consider the thermodynamic average of a one-particle quantity Q (e.g., a component of the spin torque or of the spin current) in a stationary non-equilibrium state,

$$\bar{Q} = \frac{1}{2\pi} \int_{-\infty}^{\infty} \text{Tr} \{ Q G^r(E) \Sigma^<(E) G^a(E) \} dE, \quad (\text{B.1})$$

where Q is an operator non-zero only inside the intermediate region, denoted here by \mathcal{I} , the trace refers to the Hilbert space of \mathcal{I} and the selfenergy $\Sigma^<(E)$ is given by Eqs. (4.7, 4.10). In contrast to the usual case of scalar Fermi-Dirac functions $f_{\mathcal{L},\mathcal{R}}(E)$, the presence of spin accumulation in the leads requires to include spin-dependent distributions. This means that $f_{\mathcal{L},\mathcal{R}}(E)$ in Eq. (4.10) must be understood as operators acting only on spin indices; for a given lead (\mathcal{L}, \mathcal{R}) and a given energy E , this operator is uniquely specified by a hermitean 2×2 matrix. We assume that $f_{\mathcal{L}}(E)$ commutes with the Hamiltonian H inside the left lead, so that $[f_{\mathcal{L}}(E), \Sigma_{\mathcal{L}}^{r;a}(E)] = 0$, and similarly for the right lead; however, the operators $f_{\mathcal{L},\mathcal{R}}(E)$ do not in general commute with H inside the intermediate region \mathcal{I} and with the operator Q . Let us prove that the resulting \bar{Q} , Eq. (B.1), does not depend on positions of interfaces \mathcal{L}/\mathcal{I} and \mathcal{I}/\mathcal{R} (provided that Q remains localized in \mathcal{I}). It is implicitly assumed that matrix elements of H are short-ranged, i.e., H is a tight-binding Hamiltonian.

The total value \bar{Q} can easily be decomposed in two contributions according to Eqs. (4.7, 4.10), $\bar{Q} = \bar{Q}_{\mathcal{L}} + \bar{Q}_{\mathcal{R}}$, where

$$\bar{Q}_{\mathcal{L},\mathcal{R}} = \frac{1}{2\pi} \int_{-\infty}^{\infty} \text{Tr} \{ Q G^r(E) f_{\mathcal{L},\mathcal{R}}(E) \mathcal{B}_{\mathcal{L},\mathcal{R}}(E) G^a(E) \} dE. \quad (\text{B.2})$$

Since the propagators $G^{r;a}(E)$ refer to the whole infinite system, while the operator Q is localized in the interior of \mathcal{I} and the operators $\mathcal{B}_{\mathcal{L},\mathcal{R}}$ are localized in narrow regions at the respective interfaces, it is obvious that the contribution $\bar{Q}_{\mathcal{R}}$ does not depend on the position of the \mathcal{L}/\mathcal{I} interface and vice versa.

Let us investigate the dependence, e.g., of $\bar{Q}_{\mathcal{L}}$ on the position of the \mathcal{L}/\mathcal{I} interface. Let us move the interface towards the left, which results in a modified lead $\tilde{\mathcal{L}} \subset \mathcal{L}$ and a region Λ of a finite thickness such that $\Lambda = \mathcal{L} \setminus \tilde{\mathcal{L}}$, $\mathcal{L} = \tilde{\mathcal{L}} \cup \Lambda$. The original intermediate region \mathcal{I}

is thus modified to an extended region $\tilde{\mathcal{I}} = \Lambda \cup \mathcal{I}$. An explicit expression of $\bar{Q}_{\mathcal{L}}$, Eq. (B.2), in terms of the left selfenergies is given by

$$\bar{Q}_{\mathcal{L}} = \frac{i}{2\pi} \int_{-\infty}^{\infty} \text{Tr} \{ Q G^r(E) f_{\mathcal{L}}(E) [\Sigma_{\mathcal{L}}^r(E) - \Sigma_{\mathcal{L}}^a(E)] G^a(E) \} dE, \quad (\text{B.3})$$

where the trace refers to the original intermediate region \mathcal{I} .

Let us consider the original lead \mathcal{L} decoupled from the rest of the system; its Green's function projected on the region \mathcal{L} are analogues of the TB-LMTO surface Green's functions (Sec. 2.2.3) and will also be denoted $\mathcal{G}_{\mathcal{L}}^{r,a}(E)$. It holds $[f_{\mathcal{L}}(E), \mathcal{G}_{\mathcal{L}}^{r,a}(E)] = 0$. The selfenergy of the original left lead can be expressed as

$$\Sigma_{\mathcal{L}}^{r,a}(E) = t \mathcal{G}_{\mathcal{L}}^{r,a}(E) t^\dagger, \quad (\text{B.4})$$

where t denotes that part of the Hamiltonian H that describes hoppings from Λ to \mathcal{I} while t^\dagger describes hoppings from \mathcal{I} to Λ , in the TB-LMTO picture of layered system with leads (Sec. 2.2.3) they correspond to S^β matrix elements $S_{0,1}^\beta$ and $S_{1,0}^\beta$, respectively; these (spin-independent) hoppings satisfy $[f_{\mathcal{L}}(E), t] = 0$. We assume for simplicity that Λ is thick enough so that no matrix elements of H couple $\tilde{\mathcal{L}}$ to \mathcal{I} . Substitution of Eq. (B.4) in Eq. (B.3) yields

$$\bar{Q}_{\mathcal{L}} = \frac{i}{2\pi} \int_{-\infty}^{\infty} \text{Tr} \left\{ Q G^r(E) t f_{\mathcal{L}}(E) [\mathcal{G}_{\mathcal{L}}^r(E) - \mathcal{G}_{\mathcal{L}}^a(E)] t^\dagger G^a(E) \right\} dE. \quad (\text{B.5})$$

Let us further denote by $\tilde{\Sigma}_{\mathcal{L}}^{r,a}(E)$ the selfenergy of the modified lead $\tilde{\mathcal{L}}$. Since $\mathcal{G}_{\mathcal{L}}^{r,a}(E)$ refers to the Green's function of $\mathcal{L} = \tilde{\mathcal{L}} \cup \Lambda$, i.e., of a finite region Λ attached to the semi-infinite lead $\tilde{\mathcal{L}}$, the following relation holds in the Λ region:

$$\mathcal{G}_{\mathcal{L}}^r(E) - \mathcal{G}_{\mathcal{L}}^a(E) = \mathcal{G}_{\mathcal{L}}^r(E) \left[\tilde{\Sigma}_{\mathcal{L}}^r(E) - \tilde{\Sigma}_{\mathcal{L}}^a(E) \right] \mathcal{G}_{\mathcal{L}}^a(E), \quad (\text{B.6})$$

which represents an analogy to Eqs. (2.62, 4.18). The use of Eq. (B.6) in Eq. (B.5) leads to

$$\bar{Q}_{\mathcal{L}} = \frac{i}{2\pi} \int_{-\infty}^{\infty} \text{Tr} \left\{ Q G^r(E) t \mathcal{G}_{\mathcal{L}}^r(E) f_{\mathcal{L}}(E) \left[\tilde{\Sigma}_{\mathcal{L}}^r(E) - \tilde{\Sigma}_{\mathcal{L}}^a(E) \right] \mathcal{G}_{\mathcal{L}}^a(E) t^\dagger G^a(E) \right\} dE. \quad (\text{B.7})$$

Finally, let us take into account the Dyson equation for a coupling of the isolated left lead $\mathcal{L} = \tilde{\mathcal{L}} \cup \Lambda$ to the rest of the whole system, $\mathcal{I} \cup \mathcal{R}$, by using the hoppings t and t^\dagger as a perturbation. Since the operator Q is localized inside the region \mathcal{I} while the selfenergy $\tilde{\Sigma}_{\mathcal{L}}^{r,a}(E)$ is localized in Λ , one can replace the products $G^r(E) t \mathcal{G}_{\mathcal{L}}^r(E)$ and $\mathcal{G}_{\mathcal{L}}^a(E) t^\dagger G^a(E)$ in Eq. (B.7) by the perturbed Green's functions $\tilde{G}^r(E)$ and $\tilde{G}^a(E)$, respectively. Here the $\tilde{G}^{r,a}(E)$ denote propagators of the coupled infinite system, projected on the extended intermediate region $\tilde{\mathcal{I}}$, in contrast to their projections $G^{r,a}(E)$ on the original region \mathcal{I} . This replacement yields a modified formula for $\bar{Q}_{\mathcal{L}}$,

$$\bar{Q}_{\mathcal{L}} = \frac{i}{2\pi} \int_{-\infty}^{\infty} \text{Tr} \left\{ Q \tilde{G}^r(E) f_{\mathcal{L}}(E) \left[\tilde{\Sigma}_{\mathcal{L}}^r(E) - \tilde{\Sigma}_{\mathcal{L}}^a(E) \right] \tilde{G}^a(E) \right\} dE, \quad (\text{B.8})$$

where the trace is taken over the extended region $\tilde{\mathcal{I}}$. A comparison of Eq. (B.8) and Eq. (B.3) proves insensitivity of the contribution $\bar{Q}_{\mathcal{L}}$ to the position of the \mathcal{L}/\mathcal{I} interface.

This completes a proof of the invariance of the thermodynamic average \bar{Q} , Eq. (B.1), with respect to the $\mathcal{L}/\mathcal{I}/\mathcal{R}$ partitioning.

The same invariance holds for the spin-mixing conductance $C_{\mathcal{L}}^{\text{mix}}$, Eq. (4.20), as well as for other quantities, Eqs. (5.30, 2.69), that can be obtained by infinitesimal variations of averages of the form (B.1).

Bibliography

- [1] P. Grünberg, R. Schreiber, Y. Pang, M. B. Brodsky, H. Sowers, *Phys. Rev. Lett.* 57 (1986) 2442.
- [2] M. N. Baibich, et al., *Phys. Rev. Lett.* 61 (1988) 2472.
- [3] S. Maekawa, S. Takahashi, H. Imamura, in: S. Maekawa, T. Shinjo (Eds.), *Spin Dependent Transport in Magnetic Nanostructures*, CRC Press, London, 2002, Ch. 4, p. 143.
- [4] S. Yuasa, T. Katayama, T. Nagahama, et al., *Appl. Phys. Lett.* 87 (2005) 222508.
- [5] A. D. Giddings, M. N. Khalid, T. Jungwirth, J. Wunderlich, et al., *Phys. Rev. Lett.* 94 (2005) 127202.
- [6] C. Gould, et al., *Phys. Rev. Lett.* 93 (2004) 117203.
- [7] G. A. Prinz, *Science* 282 (1998) 1660.
- [8] D. J. Monsma, J. C. Lodder, T. J. A. Popma, B. Dienny, *Phys. Rev. Lett.* 74 (1995) 5260.
- [9] J. C. Slonczewski, *J. Magn. Magn. Mater.* 159 (1996) L1.
- [10] J. Z. Sun, *IBM J. Res. Dev.* 50 (2006) 81.
- [11] D. E. Bürgler, in: S. Blügel, T. Brückel, C. M. Schneider (Eds.), *Magnetism goes Nano*, Forschungszentrum Jülich GmbH, Jülich, 2005, Ch. E6.
- [12] S. I. Kiselev, J. C. Sankey, I. N. Krivorotov, et al., *Nature* 425 (2003) 380.
- [13] S. Urazhdin, N. O. Bridge, W. P. Pratt, J. Bass, *Phys. Rev. Lett.* 91 (2003) 146803.
- [14] K. Carva, I. Turek, J. Kudrnovský, O. Bengone, *Disordered magnetic multilayers: Electron transport within the coherent potential approximation*, *Phys. Rev. B* 73 (2006) 144421.
- [15] A. Brataas, G. E. W. Bauer, P. J. Kelly, *Physics Reports* 427 (2006) 157.
- [16] I. Turek, K. Carva, *Spin-mixing conductances of metallic and half-metallic magnetic layers*, accepted for publication in *J. Phys.: Condens. Matter*.

- [17] R. Kubo, *J. Phys. Soc. Jpn.* 12 (1957) 570.
- [18] H. Bruus, K. Flensberg, *Many-body quantum theory in condensed matter physics*, Oxford University Press, New York, 2004.
- [19] S. Datta, *Electronic Transport in Mesoscopic Systems*, Cambridge University Press, 1995.
- [20] H. Mera, P. Bokes, R. W. Godby, *Phys. Rev. B* 63 (2001) 245407.
- [21] E. Louis, J. A. Vergés, J. J. Palacios, A. J. Pérez-Jiménez, E. SanFabián, *Phys. Rev. B* 72 (2005) 085311.
- [22] K. Carva, I. Turek, Tunneling junctions under finite bias voltages: Ab initio calculations of electron densities and currents, *Physica Status Solidi C* 1 (2004) 3369.
- [23] H. Mera, P. Bokes, R. W. Godby, *Phys. Rev. B* 72 (2005) 085311.
- [24] R. A. de Groot, F. M. Mueller, P. G. van Engen, K. H. J. Buschow, *Phys. Rev. Lett.* 50 (1983) 2024.
- [25] H. Ohno, *J. Magn. Magn. Mater.* 200 (1999) 110.
- [26] P. V. Dorpe, Z. Liu, et al., *Appl. Phys. Lett.* 84 (2004) 3495.
- [27] P. Hohenberg, W. Kohn, *Phys. Rev.* 136 (1964) B864.
- [28] W. Kohn, L. J. Sham, *Phys. Rev.* 140 (1965) A1133.
- [29] U. von Barth, L. Hedin, *J. Phys. C: Solid State Phys.* 5 (1972) 1629.
- [30] S. H. Vosko, L. Wilk, M. Nusair, *Can. J. Phys.* 58 (1980) 1200.
- [31] A. Gonis, *Theoretical Materials Science*, Materials Research Society, Warrendale, PA, 2000.
- [32] A. Georges, G. Kotliar, W. Krauth, M. J. Rozenberg, *Rev. Mod. Phys.* 68 (1996) 13.
- [33] V. Eyert, *J. Comput. Phys.* 124 (1996) 271.
- [34] I. Turek, V. Drchal, J. Kudrnovský, M. Šob, P. Weinberger, *Electronic Structure of Disordered Alloys, Surfaces and Interfaces*, Kluwer, Boston, 1997.
- [35] G. Rickayzen, *Green's Functions and Condensed Matter*, Academic Press, London, 1980.
- [36] L. Hedin, *Phys. Rev.* 139 (1965) 796.
- [37] K. Carva, *Time-dependent density functional theory*, Master's thesis, Charles University, Prague (2003).
- [38] A. Zangwill, P. Soven, *Phys. Rev. Lett.* 45 (1980) 204.

- [39] E. Runge, E. K. U. Gross, *Phys. Rev. Lett.* 52 (1984) 997.
- [40] O. K. Andersen, O. Jepsen, M. Šob, in: M. Yussouff (Ed.), *Lecture Notes in Physics: Electronic Band Structure and its Applications*, Springer, Berlin, 1987, p. 1.
- [41] P. Weinberger, *Electron Scattering Theory for Ordered and Disordered Matter*, Clarendon Press, Oxford, 1990.
- [42] A. Gonis, *Green Functions for Ordered and Disordered Systems*, North-Holland, Amsterdam, 1992.
- [43] P. O. Löwdin, *J. Chem. Phys.* 19 (1951) 1396.
- [44] B. Wenzien, J. Kudrnovský, V. Drchal, M. Šob, *J. Phys.: Condens. Matter* 1 (1989) 9893.
- [45] B. Velický, J. Kudrnovský, *Surf. Sci.* 64 (1977) 411.
- [46] M. P. López Sancho, J. M. López Sancho, J. Rubio, *J. Phys. F: Met. Phys.* 15 (1985) 851.
- [47] N. F. Mott, *Adv. Phys.* 13 (1964) 325.
- [48] S. F. Lee, J. W. P. Pratt, R. Loloee, P. A. Schroeder, J. Bass, *Phys. Rev. B* 46 (1992) 548.
- [49] P. M. Levy, I. Mertig, in: S. Maekawa, T. Shinjo (Eds.), *Spin Dependent Transport in Magnetic Nanostructures*, CRC Press, London, 2002, Ch. 2, p. 47.
- [50] J. Bass, W. P. Pratt, Jr., *J. Magn. Magn. Mater.* 200 (1999) 274.
- [51] X. Jiang, S. Parkin, in: S. Maekawa (Ed.), *Concepts in spin Electronics*, Oxford University Press, New York, 2006, Ch. 6, p. 239.
- [52] T. Miyazaki, N. Tezuka, *J. Magn. Magn. Mater.* 139 (1995) L2314.
- [53] J. S. Moodera, et al., *Phys. Rev. Lett.* 74 (1995) 3273.
- [54] M. Julliere, *Phys. Lett. A* 54 (1975) 225.
- [55] P. M. Tedrow, R. Meservey, *Phys. Rev. Lett.* 26 (1971) 192.
- [56] T. Valet, A. Fert, *Phys. Rev. B* 48 (1993) 7099.
- [57] R. Landauer, *IBM J. Res. Dev.* 1 (1957) 223.
- [58] M. Büttiker, *IBM J. Res. Dev.* 32 (1988) 317.
- [59] Y. Imry, R. Landauer, *Rev. Mod. Phys.* 71 (1999) S306.
- [60] P. Mavropoulos, N. Papanikolaou, P. H. Dederichs, *Phys. Rev. B* 69 (2004) 125104.
- [61] A. Crépieux, P. Bruno, *Phys. Rev. B* 64 (2001) 014416.

- [62] I. Turek, J. Kudrnovský, V. Drchal, L. Szunyogh, P. Weinberger, *Phys. Rev. B* 65 (2002) 125101.
- [63] B. Velický, J. Mašek, B. Kramer, *Phys. Lett. A* 140 (1989) 447.
- [64] C. Caroli, R. Combescot, P. Nozières, D. Saint-James, *J. Phys. C: Solid State Phys.* 4 (1971) 916.
- [65] J. Kudrnovský, V. Drchal, C. Blaas, P. Weinberger, I. Turek, P. Bruno, *Phys. Rev. B* 62 (2000) 15084.
- [66] E. M. Godfrin, *J. Phys.: Condens. Matter* 3 (1991) 7843.
- [67] D. S. Fisher, P. A. Lee, *Phys. Rev. B* 23 (1981) 6851.
- [68] V. F. Gantmakher, *Electrons and Disorder in Solids*, Clarendon Press, Oxford, 2005.
- [69] N. Møartensson, *J. Phys. F: Metal Phys.* 8 (1978) 27.
- [70] V. Drchal, J. Kudrnovský, P. Bruno, P. H. Dederichs, I. Turek, P. Weinberger, *Phys. Rev. B* 65 (2002) 214414.
- [71] P. Soven, *Phys. Rev.* 156 (1967) 809.
- [72] B. Velický, S. Kirkpatrick, H. Ehrenreich, *Phys. Rev.* 175 (1968) 747.
- [73] J. Kudrnovský, V. Drchal, J. Mašek, *Phys. Rev. B* 35 (1987) 2487.
- [74] B. Velický, *Phys. Rev.* 184 (1969) 614.
- [75] W. H. Butler, *Phys. Rev. B* 31 (1985) 3260.
- [76] J. C. Swihart, W. H. Butler, G. M. Stocks, D. M. Nicholson, R. C. Ward, *Phys. Rev. Lett.* 57 (1986) 1181.
- [77] H. Ebert, A. Vernes, J. Banhart, *Phys. Rev. B* 54 (1996) 8479.
- [78] J. Banhart, G. Czycholl, *Europhys. Lett.* 58 (2002) 264.
- [79] H. Itoh, J. Inoue, A. Umerski, J. Mathon, *Phys. Rev. B* 68 (2003) 174421.
- [80] E. Y. Tsymbal, D. G. Pettifor, *Phys. Rev. B* 54 (1996) 15314.
- [81] A. Fert, et al., *J. Magn. Magn. Mater.* 272–276 (2004) 1706.
- [82] J. Barnas, A. Fert, M. Gmitra, I. Weymann, V. K. Dugaev, *Phys. Rev. B* 72 (2005) 024426.
- [83] J. Barnas, A. Fert, M. Gmitra, I. Weymann, V. K. Dugaev, *Mater. Sci. Eng. B* 126 (2006) 271.
- [84] M. D. Stiles, A. Zangwill, *Phys. Rev. B* 66 (2002) 014407.

- [85] A. Brataas, Y. V. Nazarov, G. E. W. Bauer, Phys. Rev. Lett. 84 (2000) 2481.
- [86] A. Brataas, Y. V. Nazarov, G. E. W. Bauer, Euro. Phys. J. B 22 (2001) 99.
- [87] K. Xia, P. J. Kelly, G. E. W. Bauer, A. Brataas, I. Turek, Phys. Rev. B 65 (2002) 220401(R).
- [88] K. Xia, M. Zwierzycki, M. Talanana, P. J. Kelly, G. E. W. Bauer, Phys. Rev. B 73 (2006) 064420.
- [89] M. Zwierzycki, Y. Tserkovnyak, P. J. Kelly, A. Brataas, G. E. W. Bauer, Phys. Rev. B 71 (2005) 064420.
- [90] K. Carva, I. Turek, Ab initio theory of spin-transfer torques, accepted for publication in J. Magn. Magn. Mater.
- [91] X. Waintal, E. B. Myers, P. W. Brouwer, D. C. Ralph, Phys. Rev. B 62 (2000) 12317.
- [92] A. A. Kovalev, G. E. W. Bauer, A. Brataas, Phys. Rev. B 73 (2006) 054407.
- [93] D. Chiba, Y. Sato, T. Kita, F. Matsukura, H. Ohno, Phys. Rev. Lett. 93 (2004) 216602.
- [94] W. Wetzels, G. E. W. Bauer, M. Grifoni, Phys. Rev. B 72 (2005) 020407(R).
- [95] S. E. Barnes, S. Maekawa, in: S. Maekawa (Ed.), Concepts in spin Electronics, Oxford University Press, New York, 2006, Ch. 7, p. 293.
- [96] O. Wessely, B. Skubic, L. Nordström, Phys. Rev. Lett. 96 (2006) 256601.
- [97] E. D. Edwards, F. Federici, J. Mathon, A. Umerski, Phys. Rev. B 71 (2005) 054407.
- [98] Q. f. Sun, X. C. Xie, Phys. Rev. B 72 (2005) 245305.
- [99] J. Shi, P. Zhang, D. Xiao, Q. Niu, Phys. Rev. Lett. 96 (2006) 076604.
- [100] A. Vernes, B. Györffy, P. Weinberger, preprint: cond-mat/0609376.
- [101] Y. Wang, K. Xia, Z.-B. Su, Z. Ma, Phys. Rev. Lett. 96 (2006) 066601.
- [102] A. I. Liechtenstein, M. I. Katsnelson, V. A. Gubanov, J. Phys. F: Met. Phys. 14 (1984) L125.
- [103] J. A. Katine, F. J. Albert, R. A. Buhrman, E. B. Myers, D. C. Ralph, Phys. Rev. Lett. 84 (2000) 3149.
- [104] M. AjHajDarwish, H. Kurt, S. Urazhdin, A. Fert, et al., Phys. Rev. Lett. 93 (2004) 157203.
- [105] C. Vouille, et al., Phys. Rev. B 60 (1999) 6710.
- [106] J. C. Slonczewski, J. Magn. Magn. Mater. 247 (2002) 324.

- [107] J. Manschot, A. Brataas, G. E. W. Bauer, *Phys. Rev. B* 69 (2004) 092407.
- [108] S. Urazhdin, R. Loloee, J. W. P. Pratt, *Phys. Rev. B* 71 (2005) 100401(R).
- [109] S. S. P. Parkin, R. Bhadra, K. P. Roche, *Phys. Rev. Lett.* 66 (1991) 2152.
- [110] G. Andersson, A. M. Blixt, V. Stanciu, B. Skubic, E. Holmstrom, P. Nordblad, *J. Magn. Magn. Mater.* 267 (2003) 234.
- [111] K. Xia, P. J. Kelly, G. E. W. Bauer, I. Turek, J. Kudrnovský, V. Drchal, *Phys. Rev. B* 63 (2001) 064407.
- [112] J. Velev, W. H. Butler, *Phys. Rev. B* 69 (2004) 024404.
- [113] D. A. Stewart, W. H. Butler, X.-G. Zhang, V. F. Los, *Phys. Rev. B* 68 (2003) 014433.
- [114] E. Y. Tsymlal, D. G. Pettifor, *Phys. Rev. B* 61 (2000) 506.
- [115] O. Bengone, O. Eriksson, S. Mirbt, I. Turek, J. Kudrnovský, V. Drchal, *Phys. Rev. B* 69 (2004) 092406.
- [116] H. Ohno, A. Shen, F. Matsukura, et al., *Appl. Phys. Lett.* 69 (1996) 363.
- [117] H. Munekata, H. Ohno, S. von Molnár, et al., *Phys. Rev. Lett.* 68 (1992) 2664.
- [118] H. Ohno, H. Munekata, T. Penney, et al., *Phys. Rev. Lett.* 68 (1992) 2664.
- [119] F. Matsukura, H. Ohno, T. Dietl, in: K. H. J. Buschow (Ed.), *Handbook of Magnetic Materials*, Vol. 14, North-Holland, Amsterdam, 2002, Ch. 1, p. 1.
- [120] H. Akai, *Phys. Rev. Lett.* 81 (1998) 3002.
- [121] S. Sanvito, P. Ordejón, N. A. Hill, *Phys. Rev. B* 63 (2001) 165206.
- [122] F. Máca, J. Mašek, *Phys. Rev. B* 65 (2002) 235209.
- [123] J. Kudrnovský, I. Turek, V. Drchal, F. Máca, P. Weinberger, P. Bruno, *Phys. Rev. B* 69 (2004) 115208.
- [124] J. Kudrnovský, I. Turek, V. Drchal, F. Máca, J. Mašek, P. Weinberger, P. Bruno, *J. Superconductivity* 16 (2003) 119.
- [125] L. M. Sandratskii, P. Bruno, *Phys. Rev. B* 66 (2002) 134435.
- [126] K. Sato, P. H. Dederichs, H. Katayama-Yoshida, *Europhys. Lett.* 61 (2003) 403.
- [127] T. Jungwirth, Q. Niu, A. H. MacDonald, *Phys. Rev. Lett.* 88 (2002) 207208.
- [128] T. Jungwirth, M. Abolfath, J. Sinova, J. Kučera, A. H. MacDonald, *Appl. Phys. Lett.* 81 (2002) 4029.
- [129] K. W. Edmonds, et al., *Appl. Phys. Lett.* 81 (2002) 4991.

- [130] I. Turek, J. Kudrnovský, V. Drchal, P. Weinberger, *J. Phys.: Condens. Matter* 16 (2004) S5607.
- [131] H. Ohno, *J. Magn. Magn. Mater.* 200 (1999) 110.
- [132] J. Mašek, J. Kudrnovský, F. Máca, *Phys. Rev. B* 67 (2003) 153203.
- [133] V. Drchal, J. Kudrnovský, I. Turek, F. Máca, P. Weinberger, *Phil. Mag.* 84 (2004) 1889.
- [134] P. A. Korzhavyi, I. A. Abrikosov, E. A. Smirnova, L. Bergqvist, P. Mohn, R. Mathieu, P. Svendlindh, J. Sadowski, E. I. Isaev, Y. K. Vekhilov, O. Eriksson, *Phys. Rev. Lett.* 88 (2002) 187202.
- [135] I. Turek, K. Carva, J. Kudrnovský, Transport properties of (Ga,Mn)As diluted magnetic semiconductors in the bulk and in layered systems, *Adv. Sci. Tech.* 52 (2006) 1.
- [136] D. Chiba, F. Matsukura, H. Ohno, *Physica E* 21 (2004) 966.
- [137] K. Carva, I. Turek, Ab initio calculations of transport properties of epitaxial (Ga,Mn)As systems, accepted for publication in *J. Magn. Magn. Mater.*
- [138] J. Kudrnovský, V. Drchal, F. Máca, I. Turek, G. Bouzerar, P. Bruno, in: P. E. A. Turchi, A. Gonis, K. Rajan, A. Meike (Eds.), *Complex Inorganic Solids – Structural, Stability, and Magnetic Properties of Alloys*, Springer, New York, 2005, p. 277.
- [139] S. Ishida, T. Masaki, S. Fujii, S. Asano, *Physica B* 245 (1998) 1.
- [140] Y. Sakuraba, M. Hattori, M. Oogane, Y. Ando, H. Kato, et al., *Appl. Phys. Lett.* 88 (2006) 192508.
- [141] Y. Sakuraba, T. Miyakoshi, M. Oogane, Y. Ando, et al., *Appl. Phys. Lett.* 89 (2006) 052508.
- [142] S. Kämmerer, The Heusler alloy Co_2MnSi in thin films, Ph.D. thesis, Universität Bielefeld (2004).
- [143] P. Brown, K. Neumann, P. Webster, K. Ziebeck, *J. Phys.: Condens. Matter* 12 (2000) 1827.
- [144] L. Ritchie, G. Xiao, Y. Ji, T. Y. Chen, C. L. Chien, et al., *Phys. Rev. B* 68 (2003) 104430.
- [145] B. Ravel, M. P. Raphael, V. G. Harris, Q. Huang, *Phys. Rev. B* 65 (2001) 184431.
- [146] T. Marukame, H. Kijima, T. Ishikawa, K. i. Matsuda, T. Uemura, M. Yamamoto, submitted to *J. Magn. Magn. Mater.*
- [147] Y. Sakuraba, et al., *Jpn. J. Appl. Phys.* 44 (2005) L1100.
- [148] J. Mašek, J. Kudrnovský, F. Máca, B. L. Gallagher, et al., preprint: cond-mat/0609184, submitted to *Phys. Rev. Lett.*